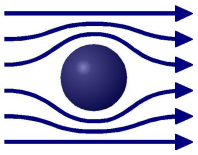

TECHNISCHE
UNIVERSITÄT
MÜNCHEN

WALTHER - MEISSNER -
INSTITUT FÜR TIEF -
TEMPERATURFORSCHUNG

BAYERISCHE
AKADEMIE DER
WISSENSCHAFTEN

Superconducting Microwave Circuits for Quantum Experiments

Diploma Thesis

Thomas Niemczyk

Advisor: Prof. Dr. Rudolf Gross

Munich, 11 May 2006

TECHNISCHE UNIVERSITÄT MÜNCHEN

Motivation

In 1965 Gordon E. Moore, a co-founder of Intel Corporation, stated that the number of transistors on a chip doubles about every two years. His prediction, popularly known as Moore's Law, has largely held the test of time to date. Current PC processors are fabricated at the 90 nm level and 65 nm chips are just being rolled out by Intel. A decade ago, chips were built at a 500 nm level. Companies are working on using nanotechnology to solve the complex engineering problems involved in producing chips at the 45 nm, 30 nm, and even smaller levels – a process that will postpone the industry meeting the limits of Moore's Law.

However, there is no doubt that sooner or later the limit for the miniaturisation of transistors in integrated circuits (ICs) based on classical semiconductor technology will be reached. When individual elements in ICs reach the size of a few nm, the physical laws that govern the behavior and properties of the circuits are inherently quantum mechanical in nature, not classical. Physicists and computer scientists became aware of this problem a long time ago and in the 1970's and early 1980's they raised the question of whether a new kind of computer could be devised based on the principles of quantum physics.

In 1982, Richard Feynman was among the first to attempt to provide an answer to this question by producing an abstract theoretical model. In reference [1] he showed how a quantum system could be used to do computations. Furthermore, he explained how such a machine would be able to act as a simulator for quantum physics. In other words, a physicist would have the ability to carry out experiments in quantum physics (e.g. many particle problems) inside a quantum mechanical computer.

In 1985, David Deutsch realized that Feynman's assertion could eventually lead to a general purpose quantum computer and published a crucial theoretical paper on quantum Turing machines. In reference [2] he showed that, in principle, *any* physical process could be modeled perfectly by a quantum computer. Thus, a quantum computer would have capabilities far beyond those of any traditional classical computer.

However, quantum information processing has gained great interest as recently as in 1994. Peter Shor showed in reference [3] how an ensemble of mathematical operations – designed specifically for a quantum computer – could be organized to enable such a machine to factor huge numbers ex-

tremely rapidly, much faster than it is possible on conventional computers. Modern *encryption* algorithms are based on the fact that it is almost impossible to factorize numbers that are a product of two large enough primes in a *reasonable* amount of time – even on nowadays most powerful computers. Therefore, factorization of very large composite numbers into their primes is the key feature for *decryption*. A computer who can do this easily is of great interest for government agencies and anyone interested in electronic and financial privacy.

The field of quantum information processing has made numerous promising advancements since its conception. Up to now there are several different realizations of so-called *qubits*, the building blocks for future quantum computers. However, a few potentially large obstacles still remain that prevent us from building a quantum computer that can rival today's modern digital computer. Among these difficulties, error correction, decoherence, and hardware architecture are probably the most demanding.

In this thesis, a device for the read out and manipulation of superconducting flux-qubits will be discussed. The device is a superconducting transmission line resonator with microstrip geometry. In **Chapter 1** an introduction to Circuit-**Q**uantum **E**lectro**D**ynamics (Circuit-**QED**) will be given. We will discuss the basic properties of qubits with the main emphasis on the **r**adio-**f**requency **S**uperconducting **QU**antum **I**nterference **D**evice (**rf-SQUID**). After that, we will describe the interaction between the qubit and the resonant cavity. **Chapter 2** deals with transmission lines and waveguides. An introduction to transmission line theory is followed by the discussion of the two transmission line structures important for this work – the microstrip and the coplanar waveguide. The fundamental properties of these waveguiding structures are presented first for normal metals and are then modified for superconducting materials. This also includes the investigation of attenuation and dispersion. Finally, resonant systems based on transmission line structures are discussed. In **Chapter 3** the actual design of our resonant structures is presented. The reader is introduced to the fundamental mode of operation of this device, providing the strong coupling between the cavity and the qubit. Computer simulations of the inductance of the slitted groundplane – which is a crucial feature in the design of our resonators – are compared to analytical results. A transmission line model that allows for the calculation of the resonance frequencies is presented. Finally, we discuss the topic of coupling capacitors and quality factors of our device. In **Chapter 4**

we first explain the measurement setup and the different calibration schemes used. Then, the S-parameter measurements of several of our resonators are discussed thoroughly and the results are compared to theory. In **Chapter 5** a summary and an outlook concerning future experiments will be given.

Contents

Chapter 1

Circuit-QED – Quantum Optics in Solid State Physics

1.1 Introduction

In this chapter the interaction between a quantum bit and the electromagnetic field in a solid-state transmission line, the Microstrip Resonator, is discussed. A short overview over the main properties of quantum bits and possible realizations in solid-state physics with focus on the *rf-SQUID* is given. Next, the Hamiltonian for the coupled qubit-cavity system, leading to the *Jaynes-Cummings-Hamiltonian*, is derived and will be discussed in more detail.

1.2 Quantum Bits

In classical computers information is processed and stored using classical bits (**bi**nary digi**ts**) usually denoted as "0" and "1". In modern microprocessors for example, the information is processed and stored using transistors. The smallest building block in quantum computers are called quantum bits or qubits. In general, a qubit is a quantum two-level system and can be represented as,

$$|\Psi(t)\rangle = \alpha(t)|0\rangle + \beta(t)|1\rangle \qquad \text{with} \qquad \alpha(t), \beta(t) \in \mathbb{C} \quad . \tag{1.1}$$

Measuring the quantum state of a qubit would yield $|0\rangle$ with a probability

$|\alpha(t)|^2$ and $|1\rangle$ with a probability $|\beta(t)|^2$. The coefficients $\alpha(t)$ and $\beta(t)$ must satisfy the normalization condition,

$$|\alpha(t)|^2 + |\beta(t)|^2 = 1 \quad . \tag{1.2}$$

The first key difference between a classical bit and a qubit is that the latter can not only exist in the "0" and "1" states of classical bits but also in a *superposition* of these states. An illustration of the qubit state as a unit vector on the Bloch sphere is found reference [4] and is shown in Figure 1.1. The qubit state can therefore be described by means of the two angles θ and ϕ as

$$|\Psi(t)\rangle = \cos\frac{\theta(t)}{2}\exp(-i\phi(t)/2)|0\rangle + \sin\frac{\theta(t)}{2}\exp(i\phi(t)/2)|1\rangle \quad . \tag{1.3}$$

A quantum computer consisting of 100 qubits represents a quantum superposition of 2^{100} states. A single operation on that particular system operates on all 2^{100} states simultaneously leading to massive quantum parallelism. One would need approximately 2^{100} classical processors to carry out the same operation in the same amount of time. It is the measurement process that projects one of these 2^{100} states to the qubits computational basis states, leading to a classical list of 100 zeros and ones.
The second key difference is the existence of *entanglement* between two or more qubits if there is finite interaction between the subsystems. Entangled qubit states are states that cannot be expressed mathematically as a product of the qubit basis states, $|\Psi\rangle \neq |\Psi_1\rangle \otimes \ldots \otimes |\Psi_n\rangle$. Physically speaking, the measurement of the state of one qubit in an entangled system is determining the state of the other qubit *instantly*. In principal this means infinite fast communication between entangled states.

1.3 Superconducting Flux Qubits – The rf-SQUID

There are many possible physical realizations of qubits, e.g. optical photon qubits, ion traps, nuclear magnetic resonance qubits, and quantum dots in semiconducting materials. From the solid-state implementations of qubits

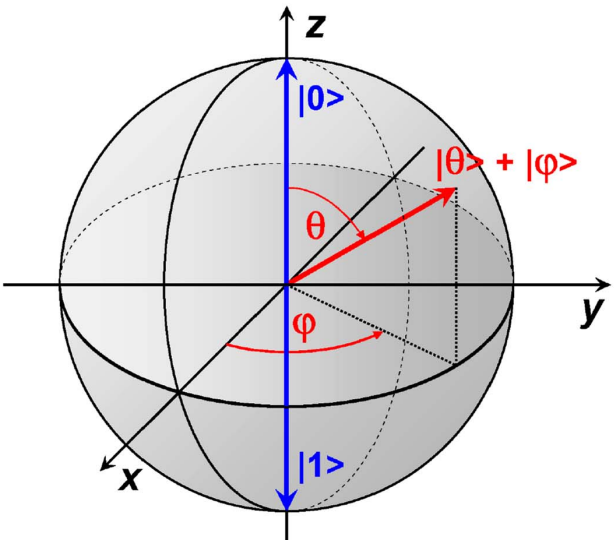

Figure 1.1: Representation of the qubit state as unit vector on the Bloch sphere.

we want to focus on the superconducting flux qubit. The use of superconducting materials has several advantages. First, the superconducting ground state is separated from the quasiparticle states by an energy gap Δ ($\sim$ meV) and therefore quasiparticle excitations are suppressed at very low temperatures. Second, the superconducting state represents a macroscopic, well-defined ground state. Last but not least, due to the large electron density in superconducting metals, perturbing background charges are screened.
In general, a superconducting flux qubit consists of a SQUID loop with inductance L interrupted by one or three Josephson junctions (JJs) [1] with capacitance C and critical current I_c. The SQUID loop interrupted by a single junction is called *rf-SQUID* while the three JJ SQUID loop is in general referred to as *flux qubit*. The rf-SQUID had been discussed in the mid 1980s as a realization of a macroscopic quantum two-level system in references [5] and [6]. However, only very recently the level repulsion near the degeneracy point has been demonstrated in reference [7]. An experimental realization of a qubit with three JJs is found in reference [8]. In equilibrium, a dissipation less supercurrent can flow inside the loop, depending on the difference of the flux Φ penetrating the loop and the external flux Φ_{ex} applied to the loop.

[1] A good overview over the physics of Josephson junctions is given in reference [4].

This either clock-wise or counter-clock-wise circulating screening current defines the two states of the qubit. The phase differences across the junctions in a SQUID device and the flux threading the superconducting loop are related by the fluxoid quantization,

$$\sum_i \gamma_i = 2\pi \frac{\Phi}{\Phi_0} + 2\pi n \quad \text{with} \quad n \in \mathbb{N} \quad . \tag{1.4}$$

Φ_0 denotes the flux quantum $h/2e$. The first experimental proof of flux quantization in superconducting loops was reported in references [9] and [10].

We will now give a theoretical description of the rf-SQUID. The Hamiltonian of the rf-SQUID is found in many textbooks (e.g. reference [11]) and can be expressed as

$$\hat{\mathcal{H}} = \frac{\hat{Q}^2}{2C} - E_\mathrm{J} \cos\left(2\pi \frac{\hat{\Phi}}{\Phi_0}\right) + \frac{(\hat{\Phi} - \Phi_{ex})^2}{2L} \quad \text{with} \quad E_\mathrm{J} = \frac{\Phi_0 I_c}{2\pi} \quad . \tag{1.5}$$

The first term describes the charging energy E_C associated with the charge $\hat{Q}$ on the capacitance C of the JJ. This term can be interpreted as the kinetic energy as $\hat{Q}$ and $\hat{\Phi}$ are canonically conjugate variables[2] with $[\hat{Q}, \hat{\Phi}] = i\hbar$ and therefore[3]

$$\frac{\hat{Q}^2}{2C} = -\frac{\hbar^2}{2C} \frac{\partial^2}{\partial \hat{\Phi}^2} \quad . \tag{1.6}$$

The second term in (1.5) accounts for the energy stored in the junction. Similar to the binding energy of a molecule this energy results from the overlap of the macroscopic wavefunctions across the superconducting electrodes. The third term finally takes into account the self-inductance L of the qubit loop. The last two terms determine the potential energy of the rf-SQUID and can be rewritten as

$$U(\hat{\Phi}) = U_0 \left[\frac{1}{2} \left(\frac{2\pi(\hat{\Phi} - \Phi_{ex})}{\Phi_0} \right)^2 - \beta_L \cos\left(2\pi \frac{\hat{\Phi}}{\Phi_0}\right) \right] \quad , \tag{1.7}$$

[2] Like momentum $\hat{p}$ and spatial coordinate $\hat{x}$ in quantum mechanics, $\hat{Q} = -i\hbar\partial/\partial\hat{\Phi}$

[3] Note the similarity to the kinetic energy term in a Hamiltonian describing the motion of a particle with mass M = C and spatial coordinate $\hat{x} = \hat{\Phi}$

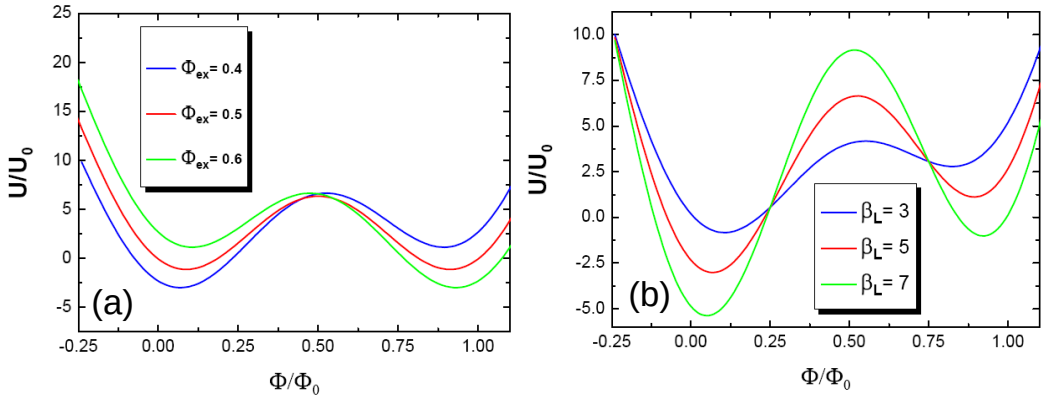

Figure 1.2: (a) Normalized potential for three different values of Φ_{ex} and $\beta_L = 5$. (b) Normalized Potential for three different values of β_L and $\Phi_{ex} = 0.4$.

where $U_0 = \Phi_0^2/4\pi^2 L$ and $\beta_L = E_J/U_0$. For $\beta_L > 1$ a double-well potential is formed with a barrier height depending on β_L and thus on I_c and L. Figure 1.2 (a) shows the potential landscape for different values of the external flux Φ_{ex} and $\beta_L = 5$. The potential is symmetric for an external applied flux of $\Phi_{ex} = 1/2$. Any other value of Φ_{ex} tilts the potential landscape. The inductance was chosen to be 0.4 nH leading to an $I_c \approx 4\mu$A. The plot in Figure 1.2 (b) shows the dependence of the barrier height for different values of β_L and an external applied flux $\Phi_{ex} = 0.4$.

1.3.1 Low-temperature approximation

In general, the rf-SQUID is a multi-level system. The states in each well correspond to opposite circulating currents. At low temperatures however, only the lowest states have to be taken into account. Therefore, the Hamiltonian can be reduced to an effective two-level system and is given by

$$\hat{\mathcal{H}} = \begin{pmatrix} \epsilon & \Delta \\ \Delta & -\epsilon \end{pmatrix} = \epsilon\hat{\sigma}_z + \Delta\hat{\sigma}_x \quad , \tag{1.8}$$

where $\hat{\sigma}_z$ and $\hat{\sigma}_x$ are the Pauli spin-matrices, the energy bias is $\epsilon = (E_1 - E_2)/2$ and a constant offset of $(E_1 + E_2)/2$ is neglected. The effective potential landscape can be seen in Figure 1.3. The lowest energy levels in each

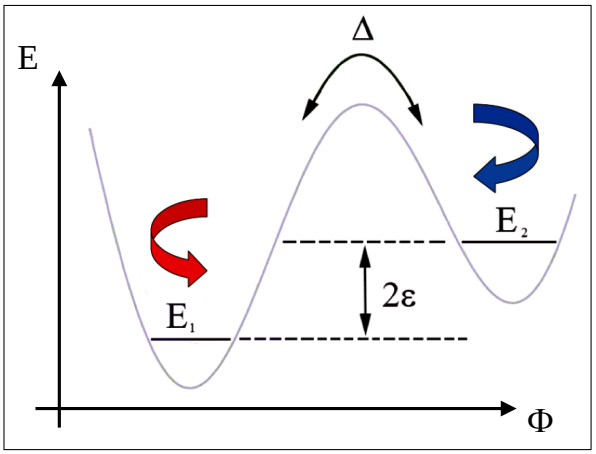

Figure 1.3: Effective potential of the rf-SQUID in the low-temperature approximation. E_1 and E_2 are the unperturbed energy levels in the absence of interaction between the wells. The arrows indicate opposite circulating currents.

well, E_1 and E_2, are the unperturbed energy levels in the absence of interaction. The tunneling amplitude Δ, which depends[4] on E_J and thus on I_c, can be derived using the WKB-approximation.
Formally, the Hamiltonian $\hat{\mathcal{H}}$ is identical to that of a spin-1/2 system in a static magnetic field $\mathbf{B}$ whose components can then be expressed in terms of E_1 and E_2. In general, this can be done with every quantum two-level system. As this concept is only a formal (but very helpful) interpretation one refers to it as the *fictitious spin* model. Diagonalizing $\hat{\mathcal{H}}$ yields the eigenenergies of the two-level system (Figure 1.4). At the degeneracy point $\epsilon = 0$ the level splitting is Δ and the eigenstates are symmetric and antisymmetric superpositions of the qubits basis states. The energy bias ϵ can be tuned by varying the external flux Φ_{ex} and is given by

$$\epsilon = 2I_q \left(\frac{\hat{\Phi}}{\Phi_0} - \frac{1}{2} \right) = 2I_q \left(f - \frac{1}{2} \right) \quad , \tag{1.9}$$

where $f = \hat{\Phi}/\Phi_0$ denotes the so-called *frustration* and I_q is the persistent current in the qubit loop.

[4] In a conventional rf-SQUID with one JJ it is not possible to vary E_J. However, by replacing the single JJ with a dc-SQUID, E_J can be changed by varying the flux Φ_{dc} through the dc-SQUID.

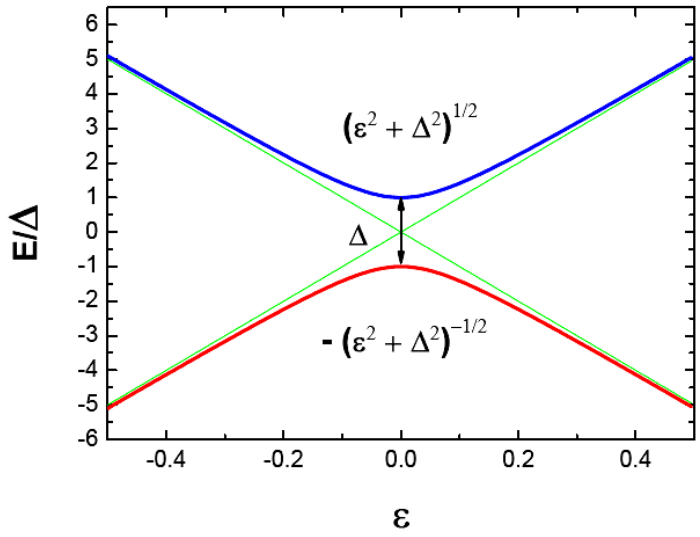

Figure 1.4: Plot of the eigenenergies for the effective Hamiltonian in the low-temperature approximation.

1.4 Qubit inside a resonant cavity

Figure 1.5 gives an idea of the capacitively coupled Microstrip Resonator (MR) to be discussed later in more detail. The qubit is placed in the center of the coil leading to an inductive coupling. The Hamiltonian of the joint qubit-cavity system can be written as

$$\hat{\mathcal{H}} = \hat{\mathcal{H}}_\mathrm{c} + \hat{\mathcal{H}}_\mathrm{q} + \hat{\mathcal{H}}_\mathrm{i} \quad , \tag{1.10}$$

where $\hat{\mathcal{H}}_\mathrm{c}$ is the cavity Hamiltonian, $\hat{\mathcal{H}}_\mathrm{q}$ is the qubit Hamiltonian and $\hat{\mathcal{H}}_\mathrm{i}$ models the interaction between them.

The Hamiltonian of the single-mode cavity is given by

$$\hat{\mathcal{H}}_\mathrm{c} = \hbar\omega_r \left(a^\dagger a + \frac{1}{2} \right) \quad . \tag{1.11}$$

This result is obtained by quantizing the classical expression for the Hamiltonian of a series LC-circuit and is given in Appendix A.

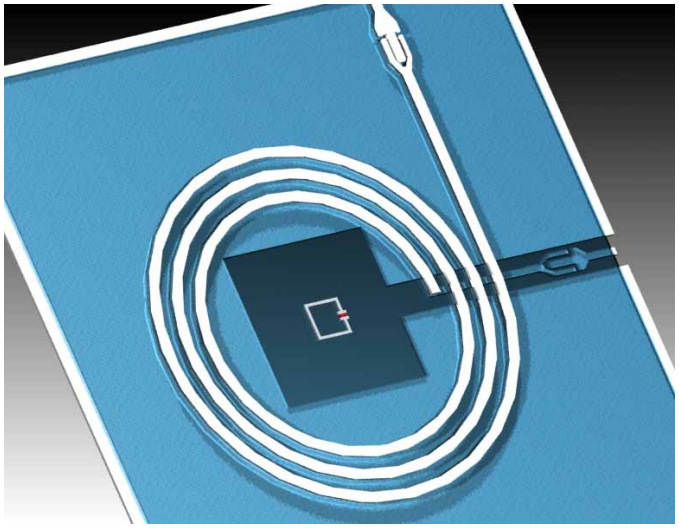

Figure 1.5: Section of the capacitive coupled Microstrip Resonator (schematic). The qubit is placed in the center of the coil. The resonator is a three layer device consisting of a washer groundplane, a dielectric (blue), and a spiral coil.

The qubit Hamiltonian in the low-temperature approximation was already given in Equation (1.8),

$$\hat{\mathcal{H}}_{\mathrm{q}} = \frac{1}{2}\begin{pmatrix} \epsilon & \Delta \\ \Delta & -\epsilon \end{pmatrix} = \frac{1}{2}\epsilon\hat{\sigma}_z + \frac{1}{2}\Delta\hat{\sigma}_x \quad . \tag{1.12}$$

The factor 1/2 arises from the renormalization of the energy scales.

The cavity and the qubit are coupled via their mutual inductance $M_{\mathrm{q,c}}$ with a coupling energy given in reference [12] as

$$\hat{\mathcal{H}}_{\mathrm{i}} = -M_{\mathrm{q,c}}\hat{I}_c\hat{I}_q \tag{1.13}$$

where $\hat{I}_c$ and $\hat{I}_q$ are the current operators of the resonant cavity and the qubit, respectively. Following a similar normal mode expansion of the cavity as given in reference [13], the current operator of the cavity field can be expressed as

$$\hat{I}_c = i \cdot I_{c,k_{o/e}}(z)\ [a^\dagger - a] \tag{1.14}$$

with

$$I_{c,k_{o/e}}(z) = \sum_{k_o=1}^{\widetilde{k_o}} \sqrt{\frac{\hbar\omega_{k_o}}{Dl}} \cos(k_o \pi z/D) + \sum_{k_e=2}^{\widetilde{k_e}} \sqrt{\frac{\hbar\omega_{k_e}}{Dl}} \sin(k_e \pi z/D) \qquad (1.15)$$

being the vacuum current for odd (k_o) and even (k_e) cavity modes. $a^\dagger$ and a in Equation (1.14) are the bosonic creation and annihilation operators, respectively. $D = \lambda/2$ is the length of the resonator along the z-axis[5] and l is the total inductance per unit length.
The cavity is chosen to operate at $k_o = 1$ and the qubit is preferably placed at an antinode ($\cos(\pi z/D) = 1$) of the vacuum current. Therefore, the expression for the vacuum current simplifies to,

$$I_{c,k_{o/e}} = \sqrt{\frac{\hbar\omega_r}{L_{\text{tot}}}}\eta \quad , \qquad (1.16)$$

where $L_{\text{tot}} = Dl$ is the total series inductance and ω_r is the cavity resonance frequency for $k_o = 1$. The dimensionless parameter $\eta \in [0; 1]$ has been introduced to account for the factor $\cos(\pi z/D)$ and models the position of the qubit with respect to the nodes and antinodes of the vacuum current.
Differentiation of Equation (1.12) with respect to the frustration f under consideration of Equation (1.9) yields the expression for the current operator of the qubit $\hat{I}_q$,

$$\hat{I}_q = \frac{\partial \hat{\mathcal{H}}_{\text{q}}}{\partial f} = I_q \hat{\sigma}_z \quad . \qquad (1.17)$$

Now, the total Hamiltonian of the joint qubit-cavity system can be written as

$$\hat{\mathcal{H}} = \hbar\omega_r \left(a^\dagger a + \frac{1}{2}\right) + \frac{1}{2}\left(\epsilon\hat{\sigma}_z + \Delta\hat{\sigma}_x\right) - i \cdot \underbrace{M_{\text{q,c}} I_q \eta \sqrt{\frac{\hbar\omega_r}{L_{\text{tot}}}}}_{g'} [a^\dagger - a]\hat{\sigma}_z \quad (1.18)$$

Diagonalization of $\hat{\mathcal{H}}$ in the eigenbasis of the qubit yields

[5] The cavity is assumed to be quasi-one-dimensional, meaning, that the spatial dimensions along the x- and y-axis are negligible to its dimension along the z-axis.

$$\hat{\mathcal{H}} = \hbar\omega_r \left(a^\dagger a + \frac{1}{2}\right) + \frac{\hbar\Omega}{2}\hat{\sigma}_z^{'} + i \cdot g^{'} \ [a^\dagger - a][\cos(\theta)\hat{\sigma}_z^{'} + \sin(\theta)\hat{\sigma}_x^{'}] \quad , \quad (1.19)$$

where $\Omega = \hbar^{-1}\sqrt{\epsilon^2 + \Delta^2}$ and $\theta = \arctan(\epsilon/\Delta)$ is the mixing angle. At the degeneracy point $\theta = \pi/2$ and by introducing the Pauli raising and lowering operators

$$\hat{\sigma}_{\pm}^{'} = \frac{\hat{\sigma}_x^{'} \pm i \ \hat{\sigma}_y^{'}}{2} \quad , \quad (1.20)$$

the total Hamiltonian can be simplified to

$$\hat{\mathcal{H}} = \hbar\omega_r \left(a^\dagger a + \frac{1}{2}\right) + \frac{\hbar\Omega}{2}\hat{\sigma}_z^{'} + i \cdot \hbar g \ [a^\dagger \hat{\sigma}_-^{'} - a\hat{\sigma}_+^{'}] \quad . \quad (1.21)$$

Here we neglected the fast oscillating terms[6], omitted damping, and defined the cavity-qubit coupling as $g := g^{'}/\hbar$. Equation (1.21) is the so-called *Jaynes-Cummings-Hamiltonian*.

A. Blais *et al.* have shown theoretically in reference [13] how the state of the qubit[7] acts on the resonance frequency ω_r of the cavity. For large qubit-cavity detuning $\delta = \Omega - \omega_r \gg g$, the system is in the dispersive regime which is favorable for readout of the qubit. By applying the unitary transformation

$$U = \exp\left[\frac{g}{\delta}(a\hat{\sigma}_+^{'} - a^\dagger\hat{\sigma}_-^{'})\right] \quad (1.22)$$

on $\hat{\mathcal{H}}$ and expanding to second order in g one obtains

$$U^\dagger\hat{\mathcal{H}}U \approx \hbar\left[\omega_r + \frac{g^2}{\delta}\hat{\sigma}_z^{'}\right] a^\dagger a + \frac{\hbar}{2}\left[\Omega + \frac{g^2}{\delta}\right]\hat{\sigma}_z^{'} \quad . \quad (1.23)$$

[6]This is the so-called *rotating wave approximation*: terms that contain $a^\dagger\hat{\sigma}_+^{'}$ and $a\hat{\sigma}_-^{'}$ are oscillating in the interaction picture at twice the frequencies of interest ω_r and Ω and are therefore neglected.

[7]The calculations were carried out for the case of a superconducting charge qubit, also known as the *Cooper Pair Box*. However, this is no limitation and the physical principals are also valid for a superconducting flux qubit, provided that the coupling between the qubit and the cavity is strong enough.

The first term in Equation (1.23) accounts for an ac-Stark shift of the cavity transition by $\hat{\sigma}_z^{'}\ g^2/\delta$. Driving the resonator with an appropriate frequency will induce a shift of the cavity resonance frequency ω_r by an amount $\pm g^2/\delta$, depending of the state of the qubit. This situation – the so-called vacuum Rabi splitting – is shown in Figure 1.6, where $\kappa = \omega_r/Q$ is the decay rate and Q is the quality factor of the cavity. The state-dependent pull of ω_r can be used to entangle the state of the qubit with that of the photons transmitted or reflected by the resonator. Due to the strong coupling between the qubit and the cavity they form a kind of '*molecule*' with two new energy levels separated by $2g^2/\delta$. For a drive frequency $\omega_{\mathrm{mw}} \simeq \omega_r \pm g^2/\delta$, the transmission of the cavity will be close to unity for one state of the qubit and close to zero for the other. By choosing the drive frequency $\omega_{\mathrm{mw}} \simeq \omega_r$, the state of the

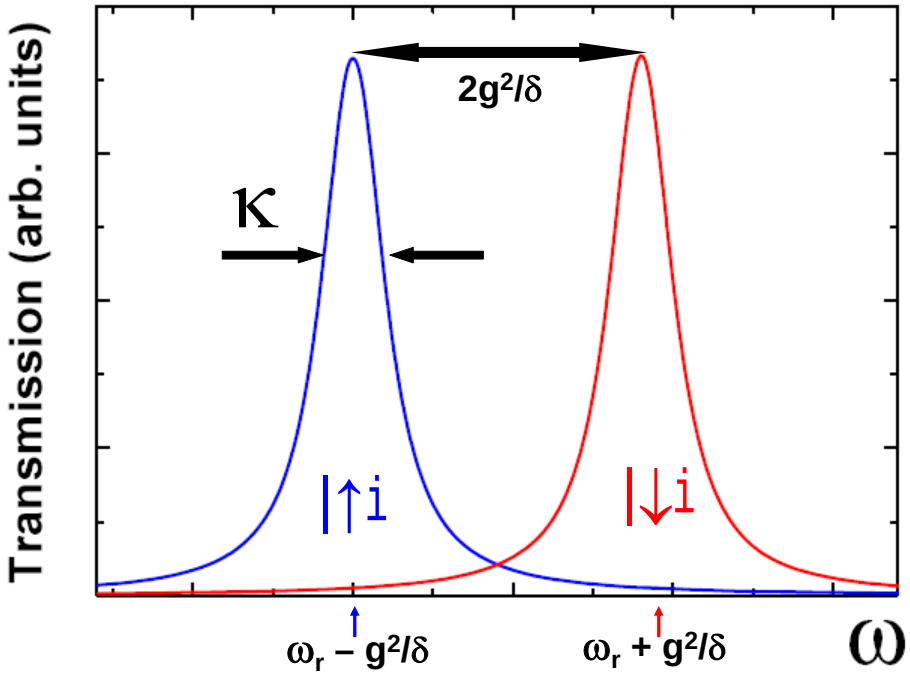

Figure 1.6: Transmission spectrum of the cavity. The resonance frequency is shifted by an amount $\pm g^2/\delta$. (red: qubit in the excited state. blue: qubit in the ground state.)

qubit is encoded in the phase of the reflected and transmitted microwaves. In reference [14] it is shown that such entangled states can be used to couple

qubits in distant resonators and therefore allowing quantum communication.

Finally, we want to give an estimate for the coupling g for the case of the Microstrip Resonators to be discussed in this thesis. To this end, we have to use some of the results that will be discussed in the subsequent chapters. With the induction extraction program *FastHenry*© we estimated the mutual inductance between the cavity and the qubit to be

$$M_{\mathrm{q,c}} \approx 1 \text{ pH} \quad , \tag{1.24}$$

where we assumed a square shaped rf-SQUID with a edge length of 10 μm and a line width of 0.5 μm. Further assuming a reasonable current through the qubit of $I_q = 1$ μA and a total inductance[8] of $L_{\mathrm{tot}} = 3^2 \cdot 848$ pH we get for a resonance frequency of $\omega_r = 2\pi 5$ GHz a coupling of

$$g = 197 \text{ MHz} \quad . \tag{1.25}$$

This value is approximately twice the calculated value in reference [13]. The experimental realization to this proposal was reported by A. Wallraff *et al.* in reference [15]. This was the first experiment that showed the coherent coupling between a single (microwave) photon and a superconducting qubit establishing the term *Circuit-QED*.

[8] In chapter 3 it will be shown that the total inductance of our resonators is dominated by the inductance of the groundplane and the number of turns of our spiral input coil. Here we assumed a coil with 3 turns, the inductance of the groundplane is calculated to be 848 pH.

Chapter 2

Transmission Lines and Waveguides

2.1 Introduction

Electrical transmission lines are used to transfer electromagnetic waves - and therefore electromagnetic energy - from a source to a device or system in which it is to be used. In general, transmission lines consist of two or more parallel conductors and support the propagation of transverse electromagnetic (TEM) waves. For a TEM wave the electric field **E** is perpendicular to both, the magnetic field **B** *and* the direction of propagation **k**.
A parallel two-wire system is a typical and important example of the transmission lines to be studied in this chapter. The concepts of energy propagation, phase and group velocity, and the effects of losses can be extended from these transmission-line results to the more general classes of guiding structures.

2.2 Transmission Line Theory

2.2.1 The Lumped-Element Circuit Model

Transmission line structures can be satisfactorily analyzed on the basis of line voltages and currents when the wavelengths of the signals being transmitted are of the same order as or a considerable fraction of the physical dimensions. The theory thus developed is often referred to as *distributed circuit theory*. A

piece of line with infinitesimal length Δz shown in Fig. 2.1 can be modeled as a lumped-element circuit, where R, L, G, and C are quantities per unit length defined as:

- R = series resistance [Ω/m]
- L = series inductance [H/m]
- G = shunt conductance [S/m]
- C = shunt capacitance [F/m]

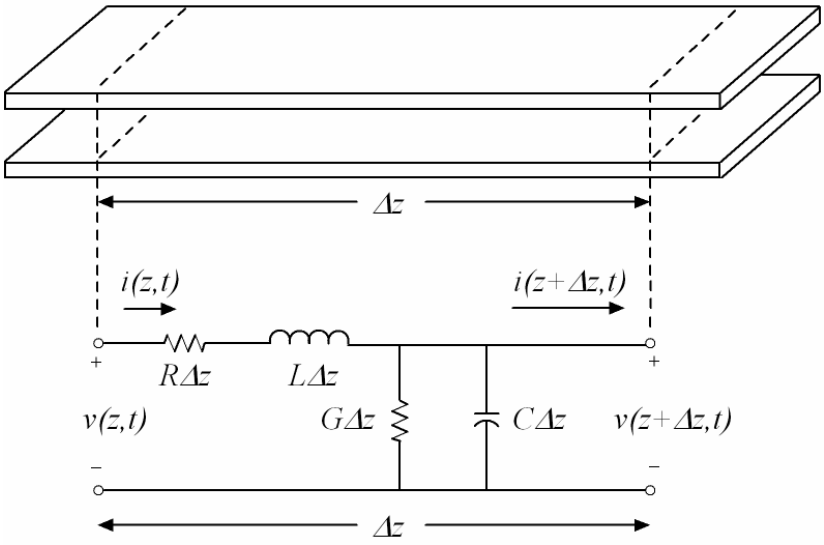

Figure 2.1: Voltage and current definitions and equivalent circuit for an incremental length of a transmission line.

The series inductance L represents the total self-inductance of both conductors while the shunt capacitance C is due to the close proximity of the two conductors. The series resistance R accounts for losses due to the finite conductivity of the conductors and the shunt conductance G represents dielectric losses. A finite length of transmission line can be regarded as many successive sections as the one shown in Fig. 2.1.
Let the input voltage and current, both dependent on position and time, of our incremental line with length Δz be $v(z,t)$ and $i(z,t)$, respectively. Then

the output voltage and current can be written as $v(z+\Delta z,t)$ and $i(z+\Delta z,t)$ and by applying Kirchhoff's voltage and current laws to the input and output nodes we obtain

$$v(z,t) - R\Delta z \cdot i(z,t) - L\Delta z \cdot \frac{\partial i(z,t)}{\partial t} - v(z+\Delta z,t) = 0 \quad , \tag{2.1}$$

$$i(z,t) - G\Delta z \cdot v(z+\Delta z,t) - C\Delta z \cdot \frac{\partial v(z+\Delta z,t)}{\partial t} - i(z+\Delta z,t) = 0 \quad . \tag{2.2}$$

Dividing equations (2.1) and (2.2) by Δz and taking the limit $\Delta z \to 0$ leads us to the following differential equations:

$$\frac{\partial v(z,t)}{\partial z} = -R \cdot i(z,t) - L\frac{\partial i(z,t)}{\partial t} \quad , \tag{2.3}$$

$$\frac{\partial i(z,t)}{\partial z} = -G \cdot v(z,t) - C\frac{\partial v(z,t)}{\partial t} \quad . \tag{2.4}$$

These are the time-domain forms of the general transmission line equations, often referred to as the *Telegrapher's Equations*. Note that space and time derivatives are partial derivatives as the reference point may be changed in space and time in independent fashion. Assuming a harmonic time dependence $e^{j\omega t}$ and denoting $v(z,t) = \Re\{V(z)e^{j\omega t}\}$ and $i(z,t) = \Re\{I(z)e^{j\omega t}\}$, where $\Re$ represents the real part of a complex quantity, equations (2.3) and (2.4) can be further simplified to

$$\frac{\partial V(z)}{\partial z} = -(R + j\omega L) \cdot I(z) \quad , \tag{2.5}$$

$$\frac{\partial I(z)}{\partial z} = -(G + j\omega C) \cdot V(z) \quad . \tag{2.6}$$

By inserting equation (2.6) into the derivative of equation (2.5) with respect to z (and vice versa) one obtains the differential equations for $V(z)$ and $I(z)$:

$$\frac{\partial^2 V(z)}{\partial z^2} - \gamma^2 V(z) = 0 \quad , \tag{2.7}$$

$$\frac{\partial^2 I(z)}{\partial z^2} - \gamma^2 I(z) = 0 \quad , \tag{2.8}$$

where

$$\gamma = \alpha + j\beta = \sqrt{(R + j\omega L)(G + j\omega C)} \tag{2.9}$$

is the complex *propagation constant*, which is a function of frequency, its unit is [m^{-1}]. Equations (2.7) and (2.8) represent *one-dimensional wave equations* for which the solutions can be easily found to be

$$V(z) = V_0^+ e^{-\gamma z} + V_0^- e^{\gamma z} \tag{2.10}$$

and

$$I(z) = I_0^+ e^{-\gamma z} + I_0^- e^{\gamma z} \quad . \tag{2.11}$$

Converting back to the time domain [1], the voltage waveform can be expressed as

$$v(z,t) = |v_0^+| \cos(\omega t - \beta z + \Phi^+) e^{-\alpha z} + |v_0^-| \cos(\omega t + \beta z + \Phi^-) e^{\alpha z} \quad , \tag{2.12}$$

where $\Phi^{\pm}$ is the phase angle of the complex voltage $V_0^{\pm} = |v_0^{\pm}| e^{j\Phi^{\pm}}$. In the same way one obtains the expression for the current wave. We see that the propagation factor $e^{-\gamma z}$ represents a wave traveling in the $+z$ direction. Furthermore, from the damping factor $e^{-\alpha z}$ one can deduce that α represents the decay with distance and is therefore called the *attenuation constant* [Nepers

[1] This is done by multiplying $V(z)$ by the harmonic time dependence and taking the real part: $\Re\{V(z)e^{j\omega t}\}$.

m^{-1} or dB m^{-1}]. β is the *phase constant* of the propagating wave [rad m^{-1} or deg m^{-1}]. In general, α and β are not constant but depend on ω which can be seen from equation (2.9). The *phase velocity* v_p is the velocity of a fixed phase point and can be calculated as

$$v_p = \frac{dz}{dt} = \frac{d}{dt}\left(\frac{\omega t + \Phi^+ - const.}{\beta}\right) = \frac{\omega}{\beta} \quad . \tag{2.13}$$

The *wavelength* λ is the distance between two successive reference points on the wave with the same phase at a fixed instant of time. Thus,

$$[\omega t - \beta z] - [\omega t - \beta(z + \lambda)] = 2\pi \quad , \tag{2.14}$$

and therefore,

$$\lambda = \frac{2\pi}{\beta} = \frac{2\pi v_p}{\omega} = \frac{v_p}{f} \quad . \tag{2.15}$$

We already derived some useful expressions of important transmission line quantities. The last one to be discussed in this section is the *characteristic impedance* Z_0 [Ω], which relates the voltage wave to the corresponding current wave at any point of the line,

$$\frac{V_0^+}{I_0^+} = Z_0 = \frac{-V_0^-}{I_0^-} \quad . \tag{2.16}$$

Z_0 can be evaluated by inserting equation (2.10) into the time-harmonic form of the general transmission line equation (2.5) which yields

$$Z_0 = \frac{R + j\omega L}{\gamma} = \frac{\gamma}{G + j\omega C} = \sqrt{\frac{R + j\omega L}{G + j\omega C}} \quad . \tag{2.17}$$

2.2.2 The Low-Loss Line

In practice all transmission lines are lossy due to a finite conductivity and/or dielectric losses, but these losses are usually small. In many practical problems these losses can then be neglected, but sometimes the effect of loss may

be of interest (e.g. when dealing with the quality factor Q of a resonant cavity). We will now see how the assumption of low losses simplifies the expressions for the general transmission line parameters γ and Z_0.
The general expression for the complex propagation constant is given by equation (2.9),

$$\gamma = \alpha + j\beta = \sqrt{(R + j\omega L)(G + j\omega C)} \tag{2.18}$$

which can be rearranged as

$$\begin{aligned} \gamma &= \sqrt{(j\omega L)(j\omega C)\left(1 + \frac{R}{j\omega L}\right)\left(1 + \frac{G}{j\omega C}\right)} \\ &= j\omega\sqrt{LC}\sqrt{1 - j\left(\frac{R}{\omega L} + \frac{G}{\omega C}\right) - \frac{RG}{\omega^2 LC}} \quad . \end{aligned} \tag{2.19}$$

For the low-loss line we can assume $R \ll \omega L$ and $G \ll \omega C$ which expresses that both, conductor and dielectric losses are small. Then, $RG \ll \omega^2 LC$ and equation (2.19) reduces to

$$\gamma = j\omega\sqrt{LC}\sqrt{1 - j\left(\frac{R}{\omega L} + \frac{G}{\omega C}\right)} \quad . \tag{2.20}$$

Ignoring the $(R/\omega L + G/\omega C)$ term would lead to a purely imaginary propagation constant which accounts for a lossless line. A Taylor series expansion $\sqrt{1+x} \simeq 1 + x/2 + \ldots$ is used to obtain the first higher order real term for γ :

$$\gamma \simeq j\omega\sqrt{LC}\left[1 - \frac{j}{2}\left(\frac{R}{\omega L} + \frac{G}{\omega C}\right)\right] \quad , \tag{2.21}$$

so that

$$\alpha \simeq \frac{1}{2}\left(R\sqrt{\frac{C}{L}} + G\sqrt{\frac{L}{C}}\right) = \frac{1}{2}\left(\frac{R}{Z_0} + GZ_0\right) \quad , \tag{2.22}$$

$$\beta \simeq \omega\sqrt{LC} \quad , \tag{2.23}$$

where

$$Z_0 = \sqrt{\frac{R + j\omega L}{G + j\omega C}} \cong \sqrt{\frac{L}{C}} \tag{2.24}$$

is the characteristic impedance for both, the low-loss and the lossless case (equal sign in (2.24)). Note, that the first term in (2.22) is due to conductor loss while the second term models dielectric losses. Equations (2.22) – (2.24) are known as the high-frequency, low-loss approximations for transmission lines.

2.2.3 The Terminated Lossy Line

Figure 2.2 shows a length l of a lossy transmission line with characteristic impedance Z_0 terminated in an arbitrary load impedance Z_L as often encountered in practical problems. In general $Z_L \neq Z_0$ and therefore an incident wave $V_0^+ e^{-\gamma z}$ generated from a source at $z < 0$ will be reflected at the interface between the line and the load. The presence of a reflected wave leads to standing waves where the magnitude of the voltage on the line is not constant.

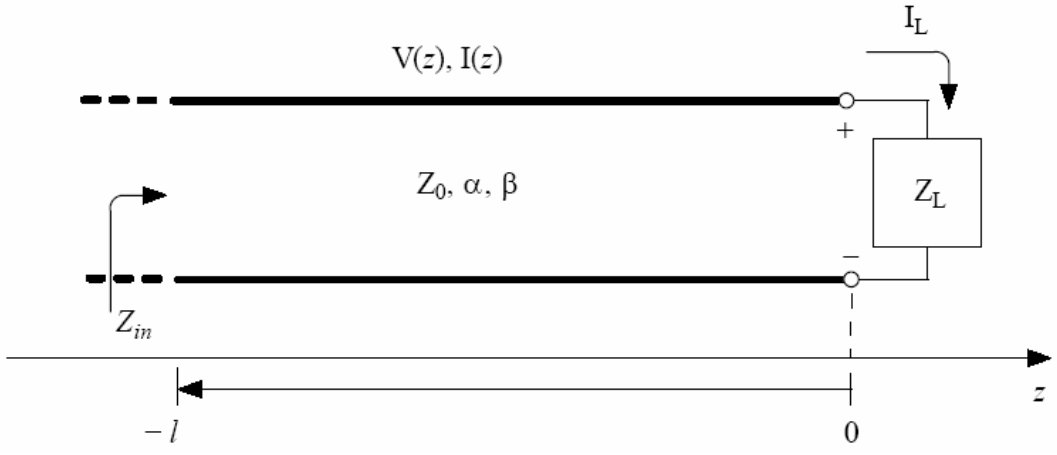

Figure 2.2: A transmission line terminated in a load impedance Z_L.

The voltage on the line can be written as in (2.10) as a sum of an incident and reflected wave:

$$V(z) = V_0^+ e^{-\gamma z} + V_0^- e^{\gamma z} \quad . \tag{2.25}$$

With (2.11) and (2.16) the current on the line can be expressed as

$$I(z) = \frac{V_0^+}{Z_0} e^{-\gamma z} - \frac{V_0^-}{Z_0} e^{\gamma z} \quad . \tag{2.26}$$

The load impedance at $z = 0$ is then given by

$$Z_L = \frac{V(0)}{I(0)} = \frac{V_0^+ + V_0^-}{V_0^+ - V_0^-} Z_0 \tag{2.27}$$

and solving for V_0^-/V_0^+ leads to

$$\Gamma = \Gamma(z = 0) = \frac{V_0^-}{V_0^+} = \frac{Z_L - Z_0}{Z_L + Z_0} \quad . \tag{2.28}$$

Γ is called *reflection coefficient* and gives the amplitude of the reflected wave normalized to the amplitude of the incident wave at the point of the load. For a *matched* line $\Gamma = 0$ (no reflected wave), otherwise the line is called *mismatched*.
The voltage and current on the line can be rewritten in terms of Γ as

$$V(z) = V_0^+ \left[e^{-\gamma z} + \Gamma e^{\gamma z} \right] \quad , \tag{2.29}$$

$$I(z) = \frac{V_0^+}{Z_0} \left[e^{-\gamma z} - \Gamma e^{\gamma z} \right] \quad . \tag{2.30}$$

Thus, the input impedance Z_{in} looking towards the load at a point $z = -l$ is

$$Z_{\text{in}}(l) = \frac{V(-l)}{I(-l)} = Z_0 \frac{1 + \Gamma e^{-2\gamma l}}{1 - \Gamma e^{-2\gamma l}} = Z_0 \frac{Z_L + Z_0 \tanh(\gamma l)}{Z_0 + Z_L \tanh(\gamma l)} \quad , \tag{2.31}$$

which is an important result that correlates the characteristic impedance of a length of transmission line with an arbitrary load impedance. Equation (2.31) is called the *transmission line impedance equation*. The input impedance for the lossless case where $\alpha = 0$ is easily obtained by inserting

$\gamma = j\beta$ into equation (2.31) and using $\tanh(j\beta) = j\tan(\beta)$.
In the same way we can generalize the expression for Γ for any point on the line $z = -l$. From (2.25) the ratio of the reflected component to the incident component is

$$\Gamma(l) = \frac{V_0^- e^{-\gamma l}}{V_0^+ e^{\gamma l}} = \Gamma e^{-2\gamma l} \quad , \tag{2.32}$$

where $\Gamma = \Gamma(z = 0)$ as described in (2.28).

2.3 Planar Transmission Lines

Several different forms of wave-guiding structures made from metal strips on a dielectric substrate are used for applications in microwave engineering. The superconducting microstrip resonator discussed in this thesis is a hybrid structure, formed of a section of microstrip (MS) line with a transition to a section of coplanar waveguide (CPW). In this section we will briefly discuss the geometry of these transmission lines and give some useful analysis formula that apply to the normal conducting case.

2.3.1 Microstrip

The MS is one of the most popular types of planar transmission lines, primarily because it can be fabricated by photolithographic processes and is easily implemented in other passive or active microwave devices. Figure 2.3 shows the geometry of a MS transmission line. A conductor of width w is printed on a thin, grounded dielectric substrate with thickness h and relative dielectric permittivity ϵ_r. The thickness of the strip and the groundplane are t_s and t_g, respectively.
In a MS most of the electrical field **E** is concentrated in the dielectric region between the strip conductor and the groundplane but a certain fraction is in the air region around the strip conductor. Therefore, a MS cannot support a pure TEM wave as the phase velocity v_p in the dielectric region ($c/\sqrt{\epsilon_r}$) is not equal to that in air (c). In most practical applications though the dielectric region is electrically very thin ($h \ll \lambda$) and the fields can be approximated by quasistatic or static solutions. The fundamental mode of propagation is therefore called a *quasi-TEM mode*.

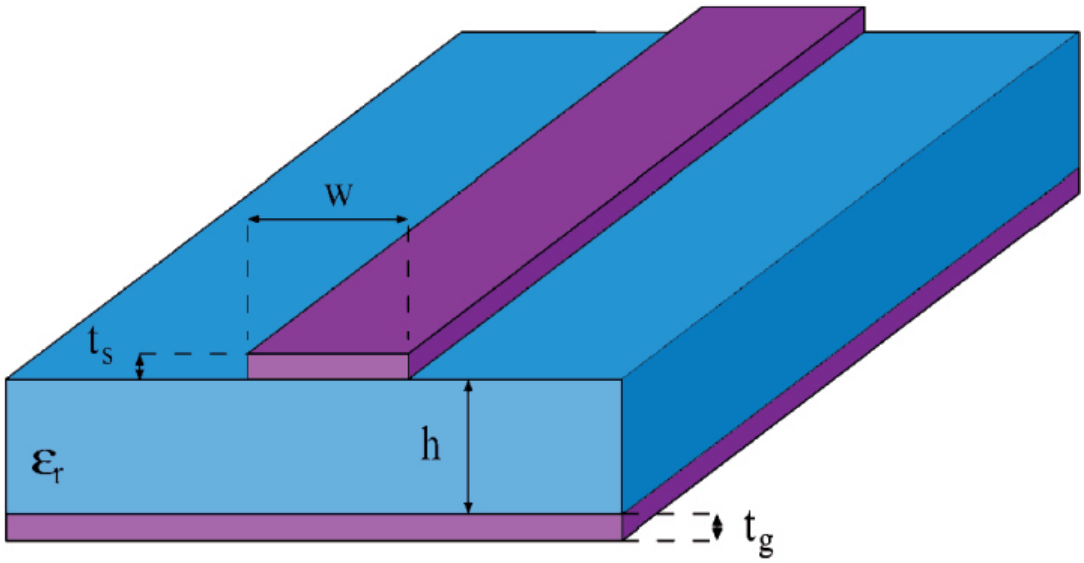

Figure 2.3: Section of a MS transmission line.

Various textbooks and publications deal with the calculations of the fundamental transmission line parameter Z_0. A particularly useful expression for the characteristic impedance is found in reference [16],

$$Z_0 = \frac{120\pi}{\sqrt{\epsilon_{\text{eff,qs}}}} \left[\frac{w}{h} + 1.98 \left(\frac{w}{h} \right)^{0.172} \right]^{-1} \quad , \tag{2.33}$$

which is accurate within $< 0.3\%$ for all $w/h > 0.06$. This expression is an approximation to the exact solution found by means of conformal mapping techniques and applies for $t_s \to 0$. Formulas that include a finite strip thickness are found in reference [17] but the effects on the design parameters are very small.

The *effective dielectric constant* $\epsilon_{\text{eff,qs}}$ in (2.33) models a MS with an effective dielectric material, filling the whole space but leading to the same capacitance per unit length as if the MS had an air/ϵ_r interface. The index *qs* in (2.33) reminds that this expression refers to the quasi-static case. A widely used expression for $\epsilon_{\text{eff,qs}}$ is found in reference [18],

$$\epsilon_{\text{eff,qs}} = 1 + \frac{\epsilon_r - 1}{2} \left[1 + \frac{1}{\sqrt{1 + 10h/w}} \right] \quad , \tag{2.34}$$

which is always between unity and ϵ_r.

Dispersion in MS

In general, the non-linear dependence of the wavelength on the frequency is called *dispersion*. In the case of the MS, dispersion has to be taken into account for frequencies $f > 1$ GHz. At high frequencies the electric field becomes more confined to the region between the center strip and the ground plane resulting in a frequency-dependent effective permittivity $\epsilon_{\text{eff}}(f)$ and therefore a frequency-dependent Z_0 in (2.33). For computer-aided design (CAD) of MS circuits it is important to have simple and accurate formulas for $\epsilon_{\text{eff}}(f)$. Kirschning and Jansen [19] developed an expression for $\epsilon_{\text{eff}}(f)$ which is claimed to be valid up to 60 GHz with an accuracy better than 0.6 %. This model has the restriction $0 \leq h/\lambda_0 \leq 0.13$ with λ_0 being the free-space wavelength.
Here, we present the formulation for dispersion calculation that is given by Kobayashi [20]. This work is based on the concept of a significant 50 % dispersion point at which the effective MS permittivity is the arithmetic mean of the substrate relative permittivity ϵ_r and the quasi-static value $\epsilon_{\text{eff,qs}}$ in (2.34). Kobayashi calculates the frequency for this condition and develops the dispersion expression,

$$\epsilon_{\text{eff}}(f) = \epsilon_r - \frac{\epsilon_r - \epsilon_{\text{eff,qs}}}{1 + (f/f_{50})^m} \quad , \tag{2.35}$$

where

$$f_{50} = \frac{f_{\text{k,TM}_0}}{0.75 + [0.75 - (0.332/\epsilon_r^{1.73})]\, w/h} \tag{2.36}$$

$$f_{\text{k,TM}_0} = \frac{c \cdot \arctan\left(\epsilon_r \sqrt{\frac{\epsilon_{\text{eff,qs}} - 1}{\epsilon_r - \epsilon_{\text{eff,qs}}}}\right)}{2\pi h \sqrt{\epsilon_r - \epsilon_{\text{eff,qs}}}} \tag{2.37}$$

$$m_0 = 1 + \frac{1}{1 + \sqrt{w/h}} + 0.332 \left(\frac{1}{1 + \sqrt{w/h}}\right)^3 \tag{2.38}$$

$$m_c = \begin{cases} 1 + \dfrac{1.4}{1 + w/h}\left[0.15 - 0.235 \exp\left(\dfrac{-0.45 f}{f_{50}}\right)\right] & \text{for } w/h \leq 0.7 \\ 1 & \text{for } w/h > 0.7 \end{cases} \tag{2.39}$$

$$m = \begin{cases} m_0 m_c \text{ for } m_0 m_c \leq 2.32 \\ 2.32 \text{ for } m_0 m_c > 2.32 \end{cases} \tag{2.40}$$

In these formulas c is the speed of light, h is in mm, and the frequency f in GHz. The accuracy of Kobayashi's expressions is estimated to be within 0.6 % for $0.1 \leq w/h \leq 10$, $1 \leq \epsilon_r \leq 128$ and for *any* value h/λ_0. Figure 2.4 shows $\epsilon_{\text{eff}}(f)$ for $\epsilon_r = 4.69$ and $h = 500$ nm as encountered in our MS design.

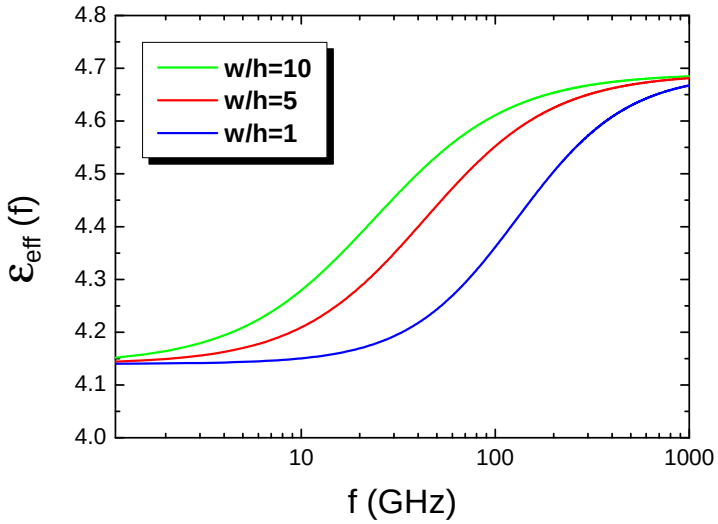

Figure 2.4: Frequency-dependent effective permittivity $\epsilon_{\text{eff,qs}}$ for three different aspect ratios w/h.

2.3.2 Coplanar Waveguide

Of the several different forms of wave-guiding systems in which all conductors are on one surface of a dielectric substrate, the most widely used is the CPW. Figure 2.5 shows the geometry of a CPW transmission line with two different dielectric substrates as encountered in our design. The signal voltage is applied between the center strip and the grounded outer strips, which are

separated symmetrically by a gap g. The quantity $w/(w+2g)$ is called aspect ratio. As with the MS, the fundamental mode of propagation is a quasi-TEM mode because the dielectric is not homogeneous in the transverse plane.

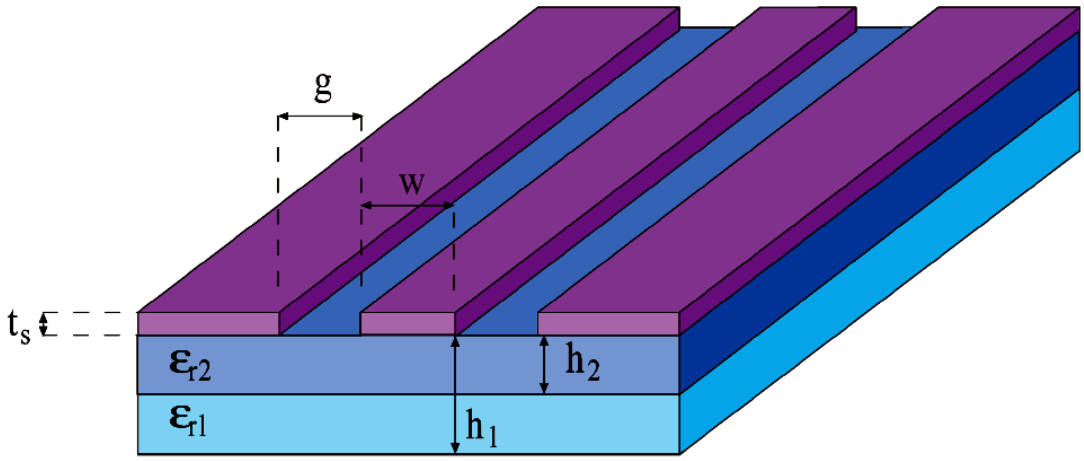

Figure 2.5: Section of a CPW transmission line with two different dielectric substrates.

We will now derive an analytical expression for the characteristic impedance Z_0 of a CPW with zero-thickness conductors and infinitely wide ground plane. The phase velocity can be expressed in terms of capacitance and inductance by combining equations (2.23) and (2.13),

$$v_{ph} = \frac{1}{\sqrt{LC}} \stackrel{!}{=} \frac{c}{\sqrt{\epsilon_{\text{eff,qs}}}} \quad . \tag{2.41}$$

Thus, Z_0 can be written as

$$Z_0 = \sqrt{\frac{L}{C}} = \frac{1}{cC_{\text{Air}}\sqrt{\epsilon_{\text{eff,qs}}}} \quad , \tag{2.42}$$

where

$$\epsilon_{\text{eff,qs}} = \frac{C}{C_{\text{Air}}} \quad , \tag{2.43}$$

is the effective dielectric constant under quasi-static approximation. C and C_{Air} are the capacitances of the CPW with and without dielectrics, respectively. These capacitances can be expressed by complete elliptic integrals of the first kind as shown in reference [21],

$$C = 4\epsilon_0 \frac{K(k_0)}{K(k_0')} + 2\epsilon_0(\epsilon_{r1} - 1)\frac{K(k_1)}{K(k_1')} + 2\epsilon_0(\epsilon_{r2} - \epsilon_{r1})\frac{K(k_2)}{K(k_2')} \quad , \tag{2.44}$$

$$C_{\mathrm{Air}} = 4\epsilon_0 \frac{K(k_0)}{K(k_0')} \quad , \tag{2.45}$$

where

$$k_0 = \frac{w}{w + 2g} \quad \text{and} \quad k_0' = \sqrt{1 - k_0^2} \quad , \tag{2.46}$$

$$k_i = \frac{\sinh(\pi w/4h_i)}{\sinh(\pi(w + 2g)/4h_i)} \quad \text{and} \quad k_i' = \sqrt{1 - k_i^2} \quad \text{with} \quad i = 1, 2 \quad . \tag{2.47}$$

Inserting equations (2.44) and (2.45) into (2.42) and (2.43) gives

$$Z_0 = \frac{30\pi}{\sqrt{\epsilon_{\mathrm{eff,qs}}}} \frac{K(k_0')}{K(k_0)} \quad , \tag{2.48}$$

$$\epsilon_{\mathrm{eff,qs}} = 1 + \frac{(\epsilon_{r1} - 1)}{2} \frac{K(k_1)}{K(k_1')} \frac{K(k_0')}{K(k_0)} + \frac{(\epsilon_{r2} - \epsilon_{r1})}{2} \frac{K(k_2)}{K(k_2')} \frac{K(k_0')}{K(k_0)} \quad . \tag{2.49}$$

Figure 2.6 shows $\epsilon_{\mathrm{eff,qs}}$ and Z_0 as a function of the dielectric height h_1 and the three realized aspect ratios of our CPW section. $w + 2g = 30$ μm is constant in all designs of the MS resonator. The dielectric with height h_2 has an $\epsilon_{r2} = 4.69$ (SiO_2). Depending on the production run of *Hypres, Inc.*, h_2 is either 500 nm or 50 nm, where the latter case refers to our designs. The other dielectric layer has $h_1 \approx 600$ μm and $\epsilon_{r1} = 11.9$ (Si). For a height $h_1 = 50$ μm the effective dielectric constant $\epsilon_{\mathrm{eff,qs}} \approx 6.37$ can be assumed to be constant for all three aspect ratios and we will use this value for further calculations. Even though one could neglect the last term in (2.49) due to

the very thin SiO_2 layer[2] the complete expression is given for the sake of completeness.

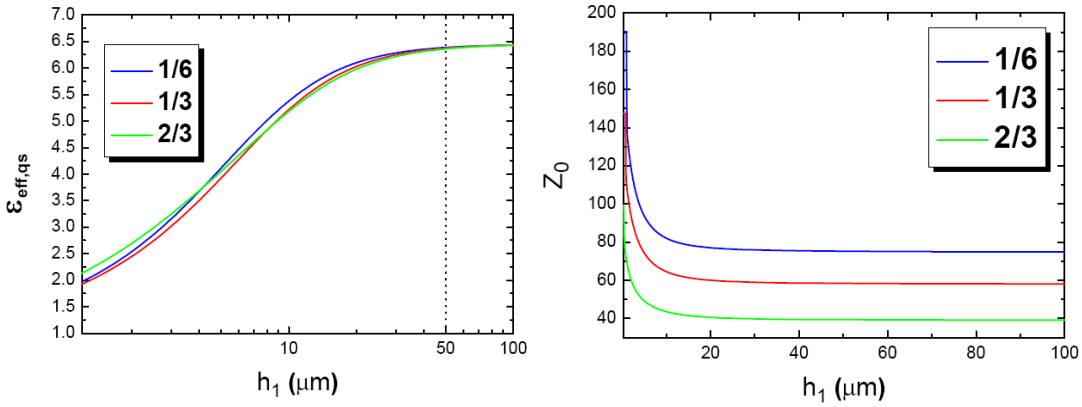

Figure 2.6: Effective dielectric constant $\epsilon_{\text{eff,qs}}$ and characteristic impedance Z_0 for different aspect ratios as a function of dielectric height h_1.

Dispersion in CPW

An empirical formula to compute $\epsilon_{\text{eff}}(f)$ of the CPW shown in Figure 2.5 has been obtained by curve fitting the dispersion data using the spectral domain method and is given in reference [22] as

$$\sqrt{\epsilon_{\text{eff}}(f)} = \sqrt{\epsilon_{\text{eff,qs}}} + \frac{\sqrt{\epsilon_r} - \sqrt{\epsilon_{\text{eff,qs}}}}{1 + aF^{-1.8}} \tag{2.50}$$

where

$$F = \frac{f}{f_{\text{TE}}} \qquad \text{and} \qquad f_{\text{TE}} = \frac{c}{4h\sqrt{\epsilon_r - 1}} \tag{2.51}$$

are the normalized frequency and the cut-off frequency (for the lowest-order TE mode), respectively. Equation (2.50) disregards the presence of a double-layer dielectric substrate. For our case however, this is not important as

[2]Calculations showed that even when h_2 would have been 500 nm, $\epsilon_{\text{eff,qs}}$ is mainly dominated by the thick Si-layer leading to approximately the same dielectric constant. Actually, the effect of the SiO_2 dielectric is only noticeable when h_2 is increased to $\approx 1.7\ \mu$m

we will neglect the very thin SiO_2 layer in our calculation and therefore $\epsilon_r = \epsilon_{r1} = 11.9$. The factor a in (2.50) is computed from the expression

$$\log(a) \approx u \log\left(\frac{w}{g}\right) + v \tag{2.52}$$

where u and v depend on the substrate thickness h_1 and are given by

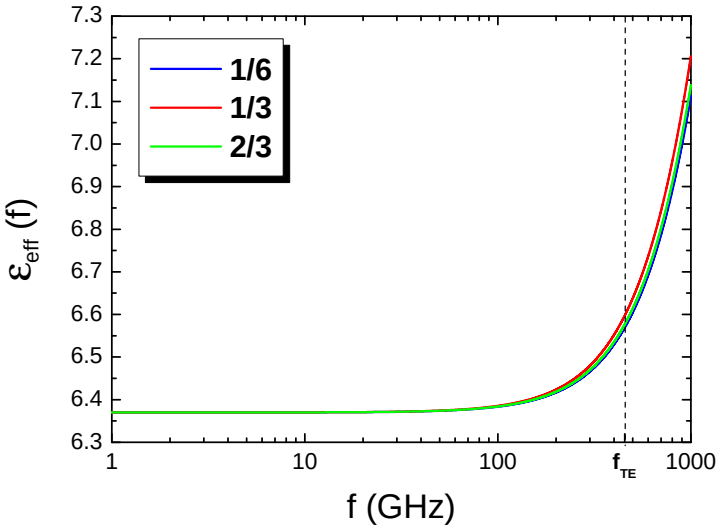

Figure 2.7: Frequency dependent effective dielectric constant $\epsilon_{\text{eff}}(f)$ for three different aspect ratios. The cut-off frequency $f_{\text{TE}} \approx 454$ GHz is indicated by the dotted line.

$$u \approx 0.54 - 0.64q + 0.015q^2 \quad , \tag{2.53}$$

$$v \approx 0.43 - 0.86q + 0.540q^2 \quad , \tag{2.54}$$

with

$$q = \log\left(\frac{w}{h_1}\right) \quad . \tag{2.55}$$

Expression (2.50) is claimed to be valid up to the THz regime with an accuracy better than 5 % for $0.1 < w/g < 5$, $0.1 < w/h_1 < 5$, $1.5 < \epsilon_r < 50$,

and $0 < f/f_{\mathrm{TE}} < 10$. In order to stay in this range of recommended parameters the calculations are carried out for a height $h_1 = 50$ μm as the minimum width for our CPW section is $w_{\mathrm{min}} = 5$ μm. Figure 2.7 presents the calculated data. The CPW shows negligible dispersion for frequencies $f <$ 100 GHz. Compared to the MS (see Figure 2.4), $\epsilon_{\mathrm{eff}}(f)$ increases more gradually in this regime until f is comparable to the cut-off frequency. At infinite frequencies $\epsilon_{\mathrm{eff}}(f)$ approaches ϵ_r.
In order to legitimate the assumption $h_1 = 50$ μm for our calculations a section of CPW with an aspect ratio of 2/3 and dimensions as encountered

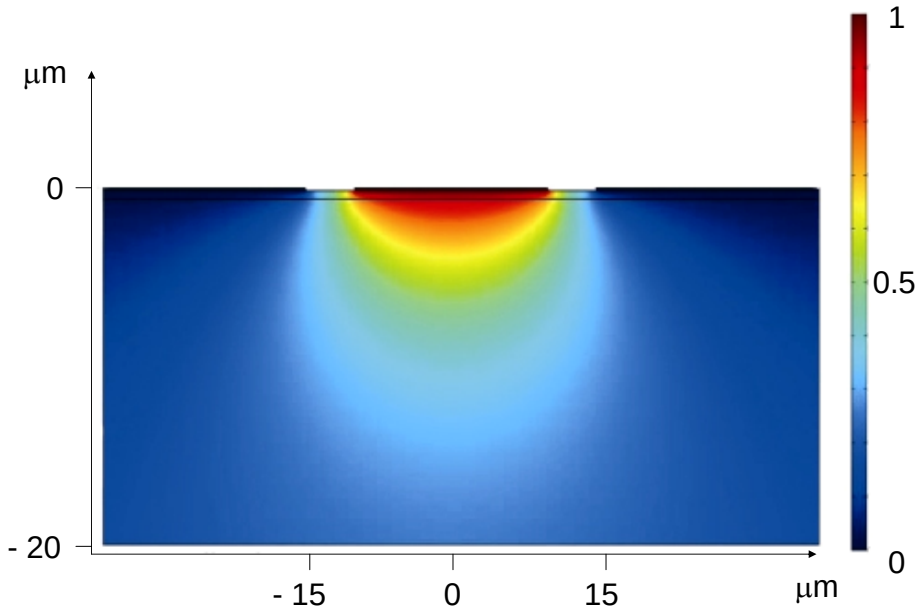

Figure 2.8: 2D plot with color-coded equipotential lines for a section of CPW with aspect ratio 2/3 and $w = 20$ μm.

in our design was simulated using the FemLab© software. Unfortunately the material library did not include perfect electric conductors (PEC) or superconductors, so the simulation was carried out for a thin copper film. Figure 2.8 shows a 2D plot with color-coded equipotential lines. The potential across the inner conductor and the groundplanes is assumed to be static. In a depth of 20 μm from the dielectric-conductor interface the normalized potential decreases to $\approx 25\%$ of its value at the surface. Under these circumstances the approximation for $h_1 = 50$ μm seems quite reasonable.

2.3.3 Superconducting Microstrip

The definitions of the fundamental transmission line parameters are still valid for MS consisting of superconducting materials. Now we have to derive expressions for the inductance L, the capacitance C, and the attenuation α that take into account superconducting materials.

Inductance

In general, the inductance per unit length of a superconductor consists of two different parts. The *internal* or *kinetic* inductance is associated with the kinetic energy of the Cooper pairs and the *external* inductance with the energy stored in the external field outside the superconductor. This interpretation results from the expression for the energy stored in the magnetic field and is given in reference [23] as,

$$W_{\mathrm{m}} = \int_{\text{all space}} \frac{1}{2}\mu \mathbf{H}^2 \, dV + \int_{\mathrm{SC}} \frac{1}{2} m v^2 n \, dV \quad , \tag{2.56}$$

where m, v, and n are the mass, velocity, and density of the Cooper pairs, respectively. For a superconductor of uniform cross section and current density $\mathbf{J}$ whose material properties are independent of $\mathbf{H}$ and $\mathbf{J}$, Equation (2.56) can be expressed as

$$W_{\mathrm{m}} = \frac{1}{2} L_{\mathrm{ext}} I^2 + \frac{1}{2} \underbrace{\frac{m}{ne^2}\frac{l}{A}}_{L_{\mathrm{kin}}} I^2 \tag{2.57}$$

where l is the length and A is the cross-sectional area of the superconductor. The concept of kinetic inductance is inherent in the London theory of superconductivity.
W.H. Chang derives in reference [24] an analytical formula to calculate the inductance of a finite-width superconducting strip transmission line using conformal mapping techniques and evaluating the fluxoid of the strip line. The formula gives an accurate inductance value when the aspect ratio $w/h > 1$ and is given by

$$L = \frac{\mu_0}{wF(w,h,t_s)} \left[h + \lambda_s \coth\left(\frac{t_s}{\lambda_s}\right) + \lambda_g \coth\left(\frac{t_g}{\lambda_g}\right) \right] \quad , \tag{2.58}$$

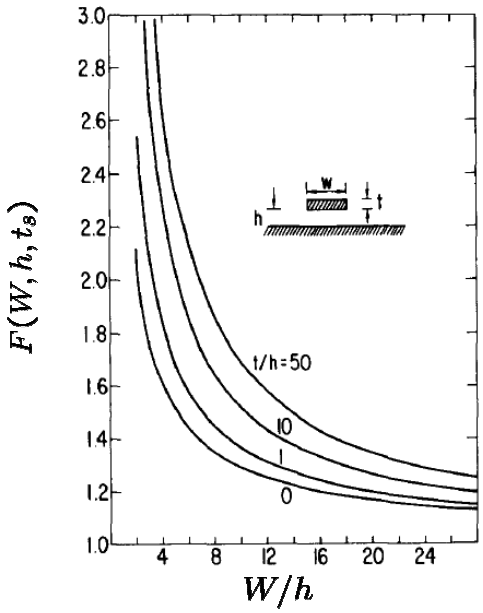

Figure 2.9: The fringe field factor $F(w, h, t_s)$ as a function of the aspect ratio. This plot is taken from reference [24].

where λ_s and λ_g are the penetration depths[3] of the metal strip and the groundplane, respectively. The first term in Equation (2.58) represents the contribution due to the external field (L_{ext}), the second term is the contribution from the strip conductor, and the last term is the contribution from the groundplane (the second and third term thus represent L_{int}). $F(w, h, t_s)$ is called the fringe field factor and is plotted in Figure 2.9 for different ratios t_s/h. When the aspect ratio $w/h \to \infty$, then $F(w, h, t_s) \to 1$ and Equation (2.58) reduces to that derived by Swihart in reference [25]. When the fringe field cannot be neglected, the inductance is reduced as though the width of the strip line is increased by a factor of $F(w, h, t_s)$. With $t_s = 600$ nm and $h = 500$ nm, the MS sections of all our resonators have a ratio $t_s/h \sim 1$, and an aspect ratio $w/h = 10$ leading to a fringe field factor $F(w, h, t_s) \sim 1.4$

[3] In general, the London penetration depth is temperature dependent and is given by $\lambda(T) = \lambda(0)\left(1 - (T/T_c)^4\right)^{-1/2}$. The measured $T_c(\mathbf{H} = 1000$ Oe) of our Nb-MRs is 8.6 K ($T_c(\mathbf{H} = 0$ will be slightly higher). As our measurements are carried out at 4.2 K this leads to an error of approximately 3% when neglecting the temperature dependence in Equation (2.58).

and therefore reducing the inductance by almost 30% of its value when fringe fields are neglected. With $w = 5$ μm, $\lambda_{s,g} = 90$ nm, $t_s = 600$ nm, and $t_g = 300$ nm the calculated external inductance is $L_{\text{ext}} = 90$ nH/m while the contribution from the internal inductance is $L_{\text{int}} = 32$ nH/m, leading to a total inductance of $L_{\text{tot}} = 122$ nH/m. Thus, neglecting the internal inductance would cause another error of approximately 30%. The values for $\lambda_{s,g}$ and $t_{s,g}$ are taken from reference [26].

Capacitance

The capacitance per unit length of a superconducting strip line is the same as for the normal conducting case and is given by

$$C = \frac{\epsilon_{\text{eff}}(f)\epsilon_0 w}{h} F(w, h, t_s) \quad , \tag{2.59}$$

where $\epsilon_{\text{eff}}(f)$ is the frequency-dependent effective dielectric constant calculated in 2.35. Calculating the capacitance per unit length in the frequency regime of interest (0 - 10 GHz) yields a mean value of $C = 0.52$ nF/m.

Attenuation

In section 2.2.2 we derived an expression for the attenuation constant α in the case of a low-loss line,

$$\alpha \simeq \frac{R}{2Z_0} + \frac{GZ_0}{2} = \alpha_c + \alpha_d \quad , \tag{2.60}$$

where α_c represents the attenuation due to conductor losses while α_d accounts for losses in the dielectric. In general, there is one more source for attenuation namely radiation loss. However, for our frequency regime of interest, $f < 10$ GHz, these losses can be neglected. The characteristic impedance for the superconducting case $Z_0 = \sqrt{L/C}$ can be easily calculated using Equations (2.58) and (2.59). In general, the shunt conductance is given by

$$G = \omega C \tan\delta \quad , \tag{2.61}$$

where C is the capacitance per unit length from Equation (2.59) and $\tan\delta$ is the so called *loss tangent*. The loss tangent is a frequency dependent value,

defined as the ratio between the real and the imaginary part of the total displacement current[4]. It was difficult to find appropriate values for the loss tangent of SiO_2 for a frequency span of 0 - 10 GHz in literature[5]. In reference [27] the value for the loss tangent for fused quartz (which consists mainly of SiO_2) at 10 GHz is given by $\tan\delta = 3 \cdot 10^{-4}$. This value will be taken for further calculations.

For the evaluation of R in Equation (2.60) we will shortly introduce the *two-fluid model* for superconductors which is discussed in more detail in various textbooks, e.g. [28]. In the framework of this model, current is carried by two non-interacting fluids consisting of normal and superconducting electrons, respectively. Like electrons in normal metals, the normal electrons are causing dissipation which can be modeled by a channel consisting of a resistor in parallel with an inductor. The channel for the superconducting electrons, however, manifests itself as a purely inductive channel. Figure 2.10 shows an equivalent circuit representing the basic idea of the two-fluid model. The total current density is the sum of the current densities for the normal and superconducting channel, $J_{tot} = J_n + J_s$. This leads to a complex conductivity for superconductors given by

$$\sigma = \sigma_1 - j\sigma_2 = \sigma_{1n} - j(\sigma_{2n} + \sigma_{2s}) \quad , \tag{2.62}$$

where the indices n and s denote normal and superconducting charge carriers, respectively. The full expression for the complex conductivity σ is given in reference [28],

$$\sigma = \frac{n_n e^2 \tau}{m(1+\omega^2\tau^2)} - j\left(\frac{n_n e^2 \omega^2 \tau^2}{m\omega(1+\omega^2\tau^2)} + \frac{n_s e^2}{m\omega}\right) \quad . \tag{2.63}$$

Here, n_n and n_s are the number densities of electrons in the normal and superconducting channel, τ is the momentum relaxation time, $\omega = 2\pi f$ is

[4]The loss tangent is defined as $\tan\delta = \frac{\omega\epsilon^{''}+\sigma}{\omega\epsilon^{'}}$. $\epsilon^{'}$ and $\epsilon^{''}$ are the real and imaginary part of the complex permittivity ϵ and σ is the conductivity. See reference [27] for further reading.

[5]The *Hypres, Inc.* design rules given in reference [26] lack any information about the loss tangent of their SiO_2 dielectric. Up to now, no measurements were performed to determine $\tan\delta$ [S. Tolpygo, *Hypres, Inc.*; private communication].

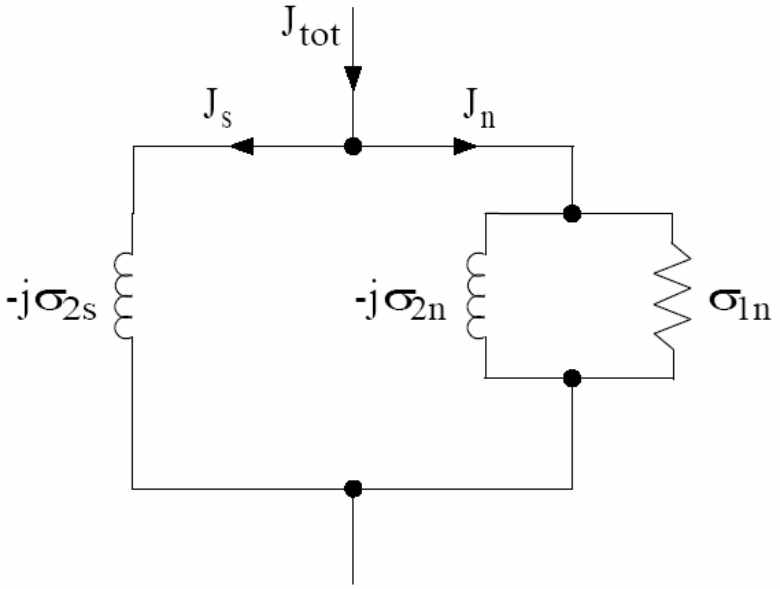

Figure 2.10: Equivalent circuit for the admittance of a unit volume of superconductor in the two-fluid model.

the angular frequency, and m is the mass of the charge carriers. As we will see later on, the number densities are temperature dependent.
For frequencies $f < 100$ GHz we can approximate $\omega^2\tau^2 \ll 1$ and Equation (2.63) gives the effective conductivity in the form

$$\sigma_{\text{eff}} = \sigma_n \frac{n_n}{n} - j\frac{1}{\omega\mu_0\lambda^2} \quad , \tag{2.64}$$

where $n = n_n + 2n_s$ is the temperature independent total density of conduction electrons in the normal state, $\sigma_n = ne^2\tau/m$ is the conductivity in the normal state, and

$$\lambda = \sqrt{\frac{m}{\mu_0 n_s e^2}} \tag{2.65}$$

is the London penetration depth. As mentioned before the number densities for the paired and unpaired electrons are temperature dependent,

$$n_n(T) = n\left(\frac{T}{T_c}\right)^4 \quad , \tag{2.66}$$

$$n_s(T) = \frac{1}{2}n\left(1 - \left(\frac{T}{T_c}\right)^4\right) \quad , \tag{2.67}$$

where T_c is the transition temperature for the superconducting state. The factor 1/2 in Equation (2.67) arises from the fact that Cooper pairs consist of two electrons with opposite spin and momentum. Equations (2.66) and (2.67) are of course only valid for $T \leq T_c$.
The resistance R per unit length is now given by,

$$R = \frac{\Re\{2Z_S\}}{w} \quad , \tag{2.68}$$

where

$$Z_S = \sqrt{\frac{j\omega\mu_0}{\sigma}} \quad , \tag{2.69}$$

is the complex surface impedance of the superconductor. $\Re$ denotes the real part and the factor 2 arises as we have to take into account both, the metal strip and the ground plane. Inserting the two-fluid relation for the effective conductivity σ_{eff} from Equation (2.64) into Equation (2.69), using a binomial expansion and the fact that

$$n \overset{(2.66)}{=} n_n(T)\left(\frac{T}{T_c}\right)^{-4} \quad , \tag{2.70}$$

the expression for the resistance R can finally be written as

$$R = \frac{\omega^2\mu_0^2\lambda^3\sigma_n}{w}\left(\frac{T}{T_c}\right)^4 \quad . \tag{2.71}$$

In reference [29], Mattis and Bardeen developed a microscopic theory for the complex conductivity that is more complicated and contains the effect of the energy gap as well as a more correct way of handling the paired and unpaired electrons. The limit of every model describing the high frequency

properties of superconductors is the fact that photon energies higher than twice the energy gap $\Delta(0)$ destroy superconductivity due to the breaking up of Cooper Pairs. In reference [30] one finds $2\Delta(0) \approx 3$ meV for Niobium which leads to a frequency of $f \approx 725$ GHz. This frequency is much higher than the operation frequencies of our MR, which are in the range of 2 - 10 GHz.
Inserting Equations (2.61) and (2.71) into Equation (2.60) gives the total attenuation in Nepers/m. Nepers can be converted to dB by multiplying

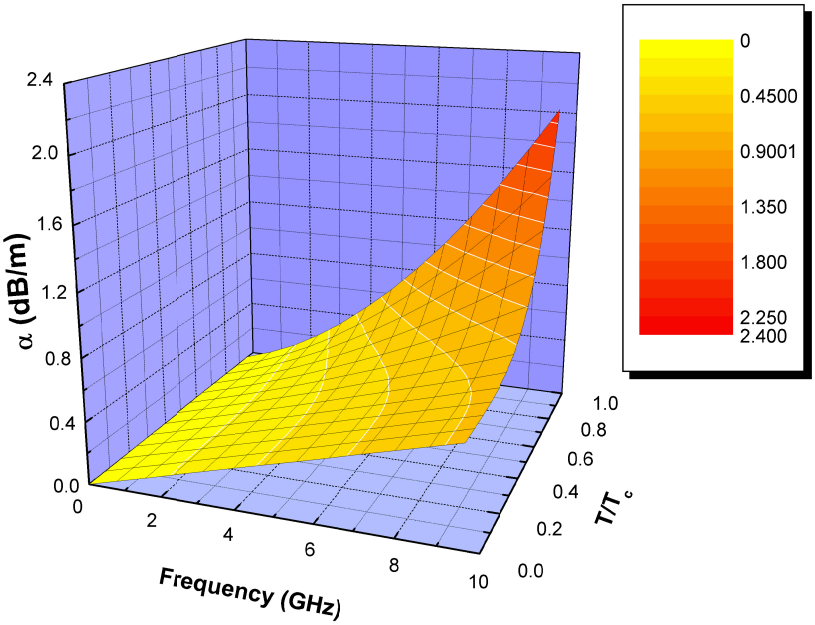

Figure 2.11: Frequency and temperature dependance of the attenuation α.

with the factor 8.686. Figure 2.11 shows the attenuation α as a function of frequency f and normalized temperature T/T_c. We calculated the data for this plot with the same set of parameters as encountered in our real MR design: transition temperature of Niobium $T_c(\mathbf{H} = 1000Oe) = 8.6$ K, normal conductivity of Niobium[6] $\sigma_n = 6.93 \cdot 10^6$ S/m, London penetration depth $\lambda = 90$ nm, width $w = 5$ μm, aspect ratio $w/h = 10$, strip thickness

[6] http://de.wikipedia.org/wiki/Niob

$t_s = 600$ nm, ground thickness $t_g = 300$ nm, effective dielectric constant $\epsilon_{\text{eff}}(10\text{ GHz}) = 4.25$, and fringe field factor $F(w, h, t_s) = 1.4$. As expected the attenuation is increasing both with temperature and frequency. In general, the increase of α_d is due to heating effects in the dielectric region between the two conductors and scales linearly with frequency. The increase od α_c is mainly determined by the power dissipation of currents flowing in a thin region $\sim \lambda$ of the conductors and scales with ω^2. The calculated attenuation is only an approximate value as we neglected the temperature dependence of λ and the penetration depth enters by the power of 3. On the one hand, for a measuring temperature of $T = 4.2$ K the error is only $\sim$ 10%. On the other hand, for $T \to T_c$ where λ diverges, one should take the calculated values from Figure 2.11 with a pinch of salt. Figure 2.12 shows α_d and α_c as function of frequency for a temperature of $T = 4.2$ K. In the superconducting state, the conductor losses are negligible compared to the dielectric losses. Furthermore, the calculated values for the attenuation are in good agreement with literature values found in references [31] and [32].

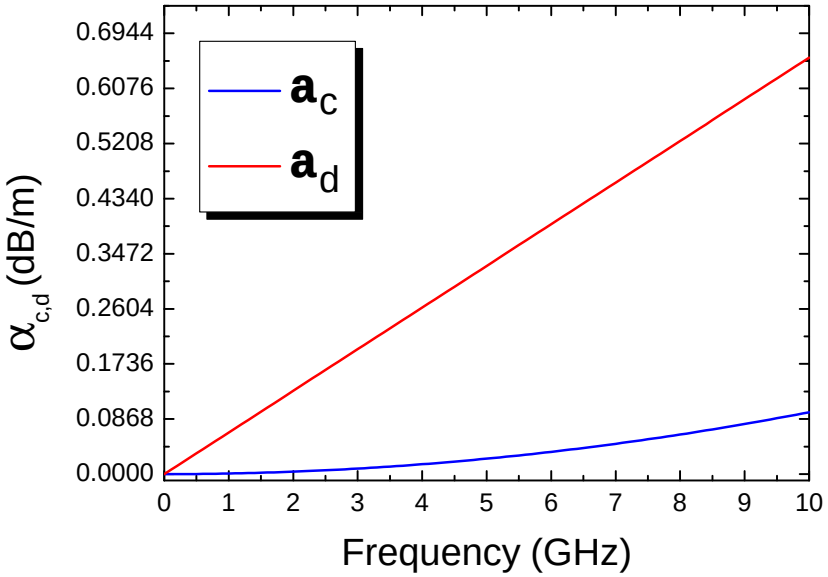

Figure 2.12: α_d and α_c as function of frequency for T = 4.2 K.

2.3.4 Superconducting Coplanar Waveguide

In this section we will shortly present the expressions for the inductance and attenuation in a superconducting CPW.

Inductance

In analogy to the superconducting MS, we have to take into account the two different contributions to the total inductance of a superconducting CPW, $L = L_{\text{int}} + L_{\text{ext}}$. However, the contributions from L_{int} are very small and it will be shown that they can be neglected for our case. In reference [33], a closed form expression for L_{int} is calculated for a static field approximation and by comparison with results from a partial wave analysis. In order to show that the contributions from the internal inductance are negligible in our case, we first have to derive an expression for L_{ext}. Using the general expression for the characteristic impedance we obtain,

$$Z_0 = \sqrt{\frac{L}{C}} = \frac{L}{\sqrt{LC}} = Lv_{ph} \overset{(2.41)}{=} L\frac{c}{\sqrt{\epsilon_{\text{eff,qs}}}} \quad . \tag{2.72}$$

Now, solving for L and using the relation for Z_0 from Equation (2.48) we get

$$\Longrightarrow L_{\text{ext}} = Z_0\frac{\sqrt{\epsilon_{\text{eff,qs}}}}{c} \overset{(2.48)}{=} \frac{30\pi}{c}\frac{K(k_0')}{K(k_0)} = \frac{\mu_0}{4}\frac{K(k_0')}{K(k_0)} \quad , \tag{2.73}$$

where all quantities are defined as in section 2.3.2. For the three different aspect ratios $k_0 = 1/6,\ 1/3,$ and $2/3$ that are realized in our designs we calculated values for the external inductance per unit length of $L_{\text{ext}} = 634$ nH/m, 491 nH/m,and 331 nH/m, respectively.
The expression for L_{int} is strongly dependent on λ and the aspect ratio of the CPW and is given by

$$L_{\text{int}} = \mu_0\lambda\frac{C}{4ADK(k_0)}\left(\frac{1.7}{\sinh(t/2\lambda)} + \frac{0.4}{\sqrt{[(B/A)^2-1][1-(B/D)^2]}}\right) \quad , \tag{2.74}$$

where

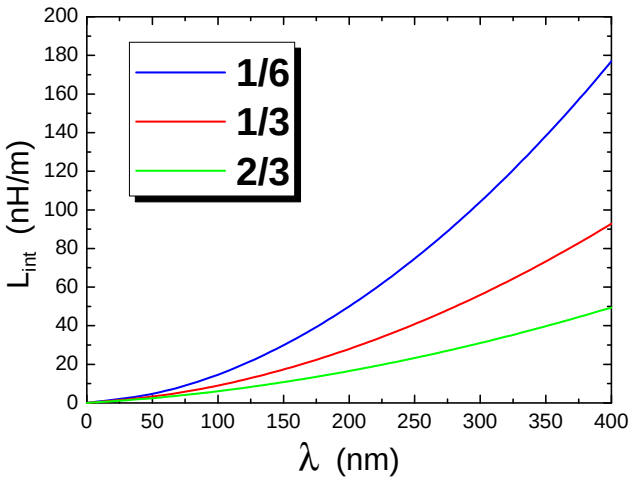

Figure 2.13: Internal inductance for the different aspect ratios of the CPW section realized in our design calculated from the closed form expression in reference [33].

$$
\begin{aligned}
A &= -\frac{t}{\pi} + \frac{1}{2}\sqrt{\left(\frac{2t}{\pi}\right)^2 + w^2} \quad , \\
B &= \frac{w^2}{4A} \quad , \\
C &= B - \frac{t}{\pi} + \sqrt{\left(\frac{t}{\pi}\right)^2 + g^2} \quad , \\
D &= \frac{2t}{\pi} + C \quad .
\end{aligned}
\tag{2.75}
$$

The quantities w, g, and t are defined as in Figure 2.5 and the temperature dependence of λ is explicitly suppressed here (see footnote on page 31). Figure (2.13) shows the calculated values for L_{int} as a function of λ. In our case, the penetration depth is $\lambda = 90$ nm leading to $L_{\text{int}} < 20$ nm/H $\ll L_{\text{ext}}$ for all aspect ratios. Thus, at low temperatures, the characteristic impedance for the superconducting CPW is mostly dominated by the expression for Z_0 for the normal conducting case. Finally, we give a short error estimation concerning the temperature dependence of λ. For $T = 0.9\ T_c$ the temperature dependent penetration depth is ~ 1.7 times its value at $T = 0$ K. Even for

$\lambda = 1.7 \cdot 90$ nm ≈ 150 nm the assumption $L_{\text{int}} \ll L_{\text{ext}}$ is still a very good approximation, leading to an error $< 5\%$ for all aspect ratios.

Attenuation

In this section we will again neglect the loss due to radiation as it is small compared to conductor and dielectric losses. In reference [34] an expression for α_c is found which is valid for arbitrary conductor thickness,

$$\alpha_c \approx \frac{R_{\text{sm}} b^2}{16 Z_0 [K^2(a/b)](b^2 - a^2)} \left(\frac{1}{a} \ln \left(\frac{2a(b-a)}{\Delta(b+a)} \right) + \frac{1}{b} \ln \left(\frac{2b(b-a)}{\Delta(b+a)} \right) \right) \quad ,$$

with $a = w/2$ and $b = w + 2g = 30$ μm for all our designs. This expression takes into account losses occurring in the center strip conductor and in the two ground planes. The groundplanes are assumed to extend to infinity, which is a good assumption for our MR as we will see later on. Δ is the so-called *stopping distance* which takes into account the edge profile θ, the strip thickness t, and the material properties. As we have no data for the edge profile we assume $\theta = 90°$. Various values for Δ are listed in reference [21]. For our case, the stopping distance was estimated to be $\Delta = 10/3$ nm. $K(a/b)$ is the complete elliptic integral of the first kind and R_{sm} is a modified surface impedance for a superconductor strip of thickness t given by

$$R_{\text{sm}} = \mu_0 \omega t \Im \left\{ \frac{\cot(k_c t) + \csc(k_c t)}{k_c t} \right\} \quad . \tag{2.76}$$

Here, the complex wavenumber k_c in a superconductor enters,

$$k_c^2 = (1/\lambda)^2 + 2j(1/\delta_s)^2, \tag{2.77}$$

with

$$\delta_s = \sqrt{\frac{2}{\mu_0 \omega \sigma_n}}$$

being the skindepth of the conductor. Figure 2.14 shows α_c for the different aspect ratios of our samples. Note, that for $w = 10$ μm the conductor losses are smallest; α_c is not linear in the aspect ratio. As expected, the conductor losses are very small and may be neglected in comparison to dielectric losses

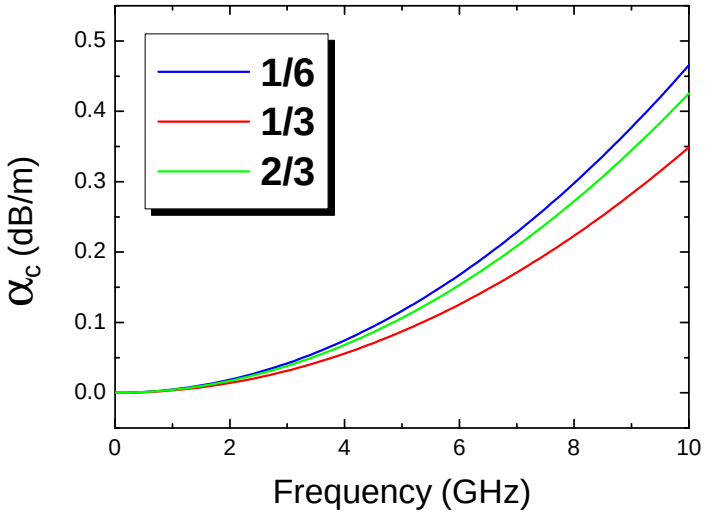

Figure 2.14: α_c as a function of frequency for the realized aspect ratios of our CPW section.

as we will see.
The attenuation constant due to dielectric losses is the same as for a normal conducting material. An expression for the attenuation constant due to dielectric losses is given in reference [35] as

$$\alpha_d = \frac{\pi}{\lambda_0} \frac{\epsilon_r}{\sqrt{\epsilon_{\text{eff,qs}}}} \, q \tan\delta \quad [\text{Neper/m}] \quad , \tag{2.78}$$

where λ_0 is the free-space wavelength and $\tan\delta$ is the loss tangent. ϵ_r and $\epsilon_{\text{eff,qs}}$ are the relative and effective dielectric constant, respectively. The filling factor q takes into account the geometry of the CPW and can be rewritten in terms of ϵ_r and $\epsilon_{\text{eff,qs}}$,

$$q = \frac{\epsilon_{\text{eff,qs}} - 1}{\epsilon_r - 1} \quad . \tag{2.79}$$

Thus, the geometry enters through the different $\epsilon_{\text{eff,qs}}$ for different aspect ratios. However, in our case $q = 0.49$ is a constant numerical factor as $\epsilon_{\text{eff,qs}} = 6.37$ for all realized aspect ratios and frequencies of interest (see sec-

tion 2.3.2). With $\epsilon_r = 11.9$ and $\tan\delta = 0.004$ at 10 GHz for Si[7] we get the result

$$\alpha_d \approx 8.41 \cdot 10^{-10}\ f \quad [\mathrm{dB/m}] \quad . \tag{2.80}$$

Figure 2.15 shows the frequency dependence of α_d. The dielectric losses

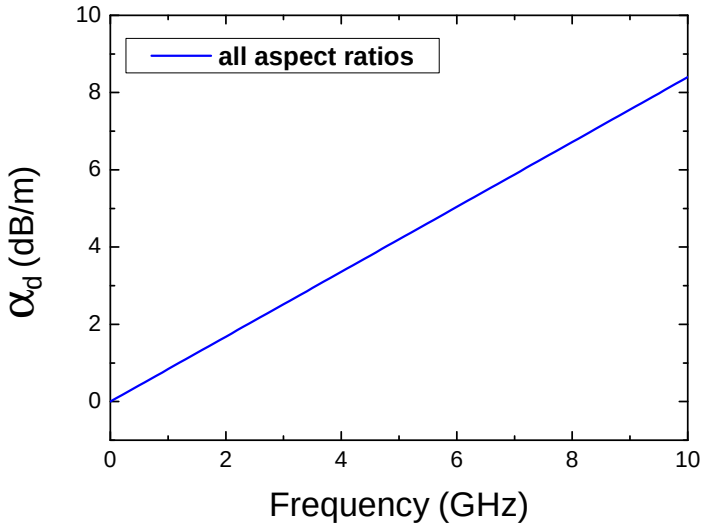

Figure 2.15: α_d as a function of frequency. α_d is not dependent on the aspect ratios as we assumed a constant $\epsilon_{\mathrm{eff,qs}}$ for the frequency range of interest.

exceed the conductor losses at least by a factor of 20. Comparing these values with those of the MS shows, that the dielectric losses in the CPW are the dominating factor and probably are the main source for a decrease in the quality factor of our MRs. The high values of α_d are mainly due to the presence of a dielectric with a higher permittivity. Replacing the Si dielectric with SiO_2 would reduce α_d by 3 dB/m for $f = 10$ GHz.

[7]Many different values for the loss tangent of Si were found in literature, though they may vary by a factor of 3. In reference [27] for instance, the loss tangent is stated to be $\tan\delta = 0.004$ at 10 GHz while in reference [17] a value of $\tan\delta = 0.01$ for the same frequency is found. As we have taken already the $\tan\delta$ value for SiO_2 from reference [27] we will do so for Si, too.

2.4 Distributed Resonators

Resonant circuits can be formed by combining discrete capacitors and inductors in parallel or series. These are so-called *lumped-element resonators* as their dimensions are small compared to the wavelength λ. In this type of resonators the capacitors are used for storing electric energy while the inductors store magnetic energy. Thus, both energies are stored in different spatial regions of the resonator. At the resonance frequency there is an exchange of energy between the capacitor and the inductor every quarter-cycle.
In contrast to the lumped-element resonators, the *distributed resonators* (usually formed by transmission lines) share the same region for storing electrical and magnetic energy and their dimensions – at least along one spatial coordinate – is comparable to the wavelength.
Whenever there is a mismatch of impedance between a transmission line and a load, reflections will occur. If the incident signal is a continuous ac waveform, these reflections will mix with the incident waveform to produce stationary waveforms, so-called *standing waves*. Depending on the termination impedance at the load end, transmission lines exhibit resonances at frequencies determined by the physical length l and the phase velocity v_{ph}. In this section we will focus on the *short*-circuit load ($Z_L = 0$) and the *open*-circuit load ($Z_L = \infty$). For both loads the incident wave will be fully reflected and the standing wave has to fulfill the boundary conditions at the short and open, respectively. This situation is analogous to standing sound waves in tubes.
In general, one can distinguish between asymmetrically and symmetrically distributed load ends which is schematically shown in Figure 2.16 (a) and (b), respectively. In the case of a microstrip geometry, the short can be realized by etching or milling a hole through the strip conductor and the dielectric and then short the strip conductor to the groundplane.
For a fixed length l and in the case of two different load ends, only odd multiples of a quarter-wavelength can fulfill the different boundary conditions. This situation is shown in Figure 2.16 (a) and this type of resonator is referred to as $\lambda/4$-resonator. In the case of symmetrical load ends, only even multiples of a quarter-wavelength satisfy the boundary conditions and one speaks of a $\lambda/2$-resonator. This situation is shown in Figure 2.16 (b). Replacing the short by an open and vice versa does not change the type of resonator, however, in the standing wave patterns of Figure 2.16 one has to replace voltage

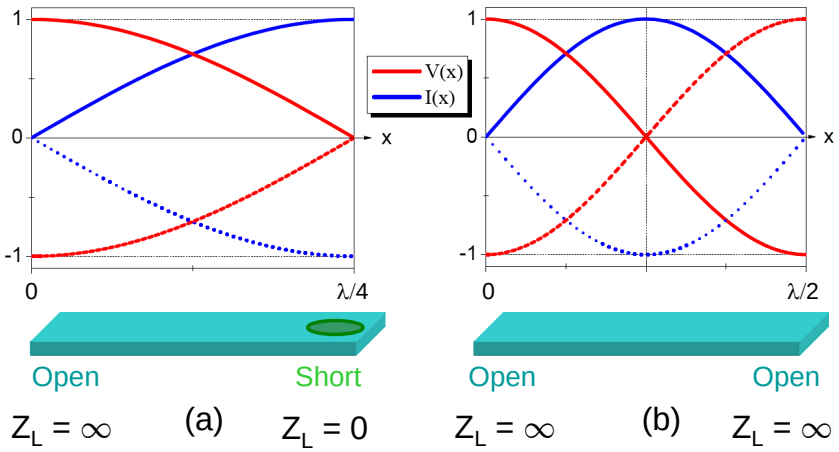

Figure 2.16: Standing wave patterns for a section of a transmission line. (a) Standing wave pattern for asymmetrically distributed load ends leading to $\lambda/4$-resonator. (b) Standing wave pattern for symmetrically distributed load ends leading to $\lambda/2$-resonator.

by current and vice versa. The most convenient way to couple these types of resonators to the external circuitry is by means of coupling capacitors. The presence of coupling capacitors effectively modifies the load impedance seen by the electromagnetic wave, however, as long as the coupling capacitors are small enough, $Z_L = \infty$ and $Z_L = 0$ are good approximations[8]. The MR to be discussed in the next chapter can be modeled as an open $\lambda/2$-resonator. The resonance frequencies of these types of resonators are given by

$$f_{n,\lambda/4} = n\frac{v_{\mathrm{ph}}}{4l} \quad (n \text{ odd}) \quad , \tag{2.81}$$

$$f_{n,\lambda/2} = n\frac{v_{\mathrm{ph}}}{4l} \quad (n \text{ even}) \quad . \tag{2.82}$$

[8]The actual value of the coupling capacitors for which the assumption $Z_L = \infty$ and $Z_L = 0$ are still valid strongly depends on the overall dimensions of the resonator. The coupling capacitors will be discussed in more detail in section 3.2.

Chapter 3

The Superconducting Microstrip Resonator

3.1 Introduction

A. Wallraff *et al.* experimentally showed strong coupling between a superconducting charge qubit, the Cooper Pair Box, and a superconducting CPW transmission line in reference [15]. For this purpose, transmission line resonators with a high internal quality factor Q are needed. The layout for the superconducting Microstrip Resonator (MR), to be discussed in this chapter, is based on the design of the dc SQUID microstrip amplifier originally proposed by M. Mück and J. Clarke in reference [36]. M. Mariantoni suggested this design for qubit manipulation and readout provided that the MR has both, a high quality factor $Q > 10^4$ and a high cavity-qubit coupling g in order to access the strong coupling regime of Circuit-QED.
In this Chapter the general layout of the MR is presented. We used the student version of the *Xic*© software from *Whiteley Research, Inc.* for designing our structures. Expressions for the resonance frequencies and the quality factor Q are presented and the presence of a slitted washer groundplane, effectively increasing the inductance per unit length of our transmission line, will be taken into account. The coupling capacitances of the MR as well as the washer inductance are estimated using the FastHenry©, FastCap©, and 3D-MLSI© simulation software. Finally, we theoretically discuss the quality factors and the resonance frequencies of our MR.

3.2 General Layout

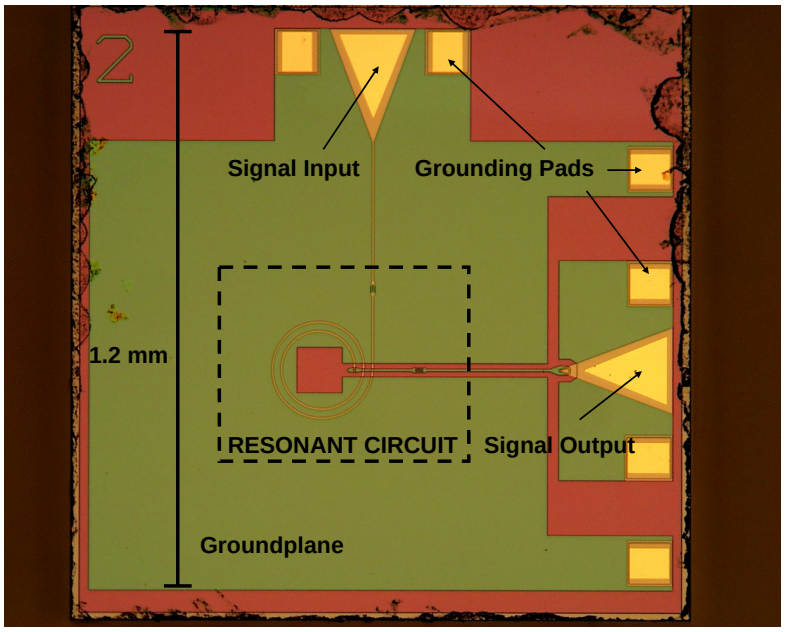

Figure 3.1: Photograph of a MR fabricated at *Hypres, Inc.*

The MR is a distributed transmission line resonator consisting of a niobium spiral coil deposited on top of a SiO_2 dielectric over a niobium groundplane. It has a microstrip geometry with a cross-section shown in Figure 2.3. Figure 3.1 shows a photograph of the whole chip containing the signal in- and output ports as well as the grounding pads of the groundplane. These pads consist of a thin Ti/PdAu film with a thickness of approximately 350 nm. The actual resonant circuit is defined by the section of transmission line coupled capacitively to the in- and output ports and is magnified in Figure 3.2. It is important to note, that the resonant LC-circuit is formed by the inductance of the coil and the capacitance between coil and groundplane and *not* by the capacitance of the coupling capacitors.
Looking at Figure 3.2 it becomes clear why we also discussed the CPW so intensely: in order to leave the uppermost layer containing the spiral input coil we have to break-through the dielectric layer and make a connection to a small section of CPW. In the following, this MS-to-CPW transition is referred to as *via*. Usually, vias are fabricated by etching a hole through the dielectric layer followed by metallization of the hole.

The via is a critical point in the design of our resonator since the impedance of the MS (Z_{MS}) is not equal to the impedance of the CPW section (Z_{CPW}). According to the *Hypres, Inc.* design rules given in reference [26], the via must have a minimum edge length of 3 μm and the niobium surrounding it must exceed the vias dimensions by at least 1.5 μm. Thus, the minimum width of the MS section was chosen to be 5 μm. The thickness of the SiO_2 dielectric can not be changed and has a value of $h = 0.5$ μm. With the calculated values for L and C in section 2.3.3 we get a characteristic impedance of

$$Z_{\mathrm{MS}} = \sqrt{\frac{L}{C}} = \sqrt{\frac{122 \text{ nH/m}}{0.52 \text{ nF/m}}} = 15.7\ \Omega \quad . \tag{3.1}$$

Increasing the width would decrease the characteristic impedance as Z_{MS}

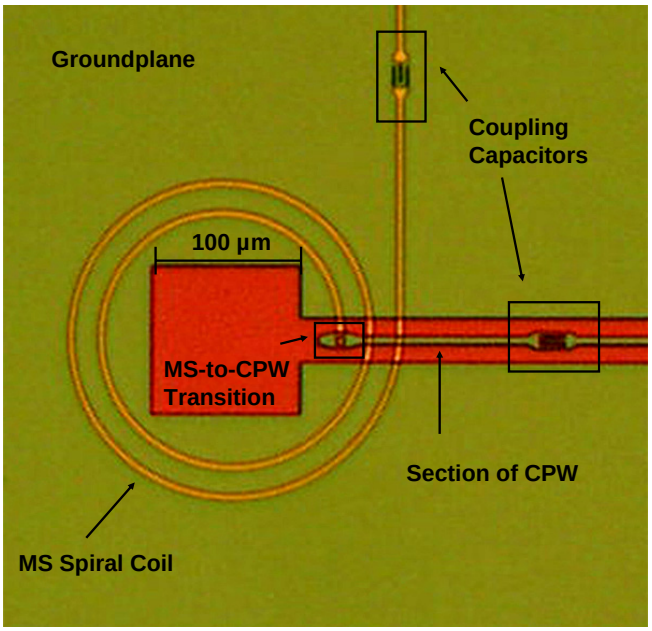

Figure 3.2: Magnified view on the actual resonant LC-circuit.

is proportional to $1/w$. On the other hand, we have some restrictions concerning the CPW section. For this layer the design rules require a minimum spacing of 2.5 μm between adjacent conductors which is then determining our minimum gap width g. In general, a smaller gap g leads to a smaller

$w[\mu\text{m}]$	10	50	250	2500	**20000**
Z_{CPW} [Ω]	38.4	26.5	21.7	17.6	**15.7**

Table 3.1: Calculated impedances for a minimum gap $g = 2.5$ μm using the TXLine© software package

impedance. To make a quick estimation of the width necessary to achieve an impedance around 15 Ω when the gap is fixed to $g = 2.5$ μm, we used the software tool TXLine© from *Applied Wave Research, Inc.*, which is capable of calculating impedances for various passive circuits and corresponding dimensions. The calculations were carried out for a conventional CPW with a height of $h = 50$ μm, a conductor thickness of $t = 0.3$ μm, an $\epsilon_r = 11.9$ and a loss tangent of $\tan\delta = 0.015$.

Table 3.1 shows the calculated impedances for different values of w of the CPW center strip. For a conventional MS, impedance matching at the point of the via would be impractical if we chose reasonable dimensions for our transmission lines. In the next section, we will see how the presence of a slitted groundplane will influence the properties of our MS leading to a higher impedance and thus better matching. We decided to design our CPW section with a fixed $w + 2g = 30$ μm and designed three different center strips with a width of $w = 5$ μm, 10 μm, and 20 μm, respectively. Using Equation (2.48) we calculate the following impedances for our different CPW sections:

$$\begin{aligned} Z_{\text{CPW},1/6} &= 75.3\ \Omega \quad , \\ Z_{\text{CPW},1/3} &= 58.5\ \Omega \quad , \\ Z_{\text{CPW},2/3} &= 39.3\ \Omega \quad . \end{aligned} \tag{3.2}$$

3.2.1 Mode of Operation

In section 1.4 we discussed the coupling between a resonant transmission line and a rf-SQUID qubit. The coupling g depends upon the mutual inductance between the qubit and the LC-circuit and on the currents flowing in the qubit and the transmission line. Now we will have a closer look on the presence of a slit in our superconducting groundplane. Figure 3.3 shows

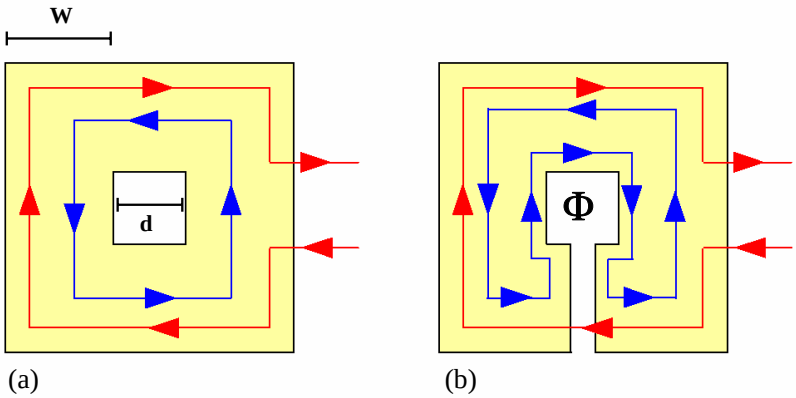

Figure 3.3: (a) In the absence of a slit, the current in the input coil (red) is fully screened by a counter-rotating current in the washer (blue). (b) The slit forces the screening current in the washer to complete its path by turning in towards the center of the washer and around the hole. This creates a net flux Φ in the center of the washer and thus increases the inductance in the input coil.

a schematic comparison between the paths of the screening currents (blue) with and without a slit in the washer. In the absence of the slit, screening currents in the washer are able to completely cancel the flux induced by the input current in the coil. The coil thus behaves as if it was stretched out linearly over an infinite groundplane. In the presence of the slit, however, the screening currents are forced to complete the circuit by following the inner path around the slit and washer hole. This current is not balanced by an oppositely directed current in the input coil and thus establishes a flux Φ in the center of the washer. This flux in turn increases the inductance reflected into the input coil.
In the model of Ketchen and Jaycox given in reference [37], the total inductance of a n-turn coil tightly coupled to washer with inductance L_{washer} is found to be

$$L_{\text{tot}} \simeq lL + n^2 L_{\text{washer}} \quad , \tag{3.3}$$

where l is the length of the input coil and L is its self-inductance per unit length. This effect is increasing the characteristic impedance of the MS sec-

tion and decreasing the resonance frequency of the MR as we will see later on. Furthermore, Ketchen and Jaycox state that the coupling coefficient α^2 and the mutual inductance between the washer and the coil are given by

$$\alpha^2 \simeq \left(1 + \frac{L}{n^2 L_{\text{washer}}}\right)^{-1} \quad , \tag{3.4}$$

$$M \simeq nL \quad . \tag{3.5}$$

The spiral input coil and the washer groundplane are coupled in essentially the same manner as a $n:1$ turn thin-film transformer.

Estimate of the Washer Inductance

In reference [37] Ketchen and Jaycox present a closed form expression for the inductance of a washer groundplane as shown in Figure 3.3 (a),

$$L_{\text{washer}} = 1.25\mu_0 d \quad \text{for} \quad W > d \quad , \tag{3.6}$$

where d is the width of the hole and W is the outer width of the washer. The hole size of our MR is $d = 100$ μm for all designs leading to a washer inductance of $L_{\text{washer}} = 157$ pH. Equation (3.6) does not take into account the presence of a slit.

To obtain more reliable data, we used two different software tools and modeled the washer groundplane with the exact dimensions we used in our MR designs. Inductance extraction algorithms need to simulate a current flowing through the conductor in order to solve the Maxwell- and London Equations. Thus, current input and output terminals have to be defined and it turned out that the calculated inductances depend on the location of these terminals. The two grounding pads extending the main washer area (right hand side of Figure 3.1) acted as current terminals for the simulations. For these terminals the current path is symmetric around the hole and the slit. In addition, this configuration yields the longest current path and therefore we get an upper limit for L_{washer}.

One program was the Fasthenry© inductance extraction program which is capable of simulating superconducting materials. Another advantage is that

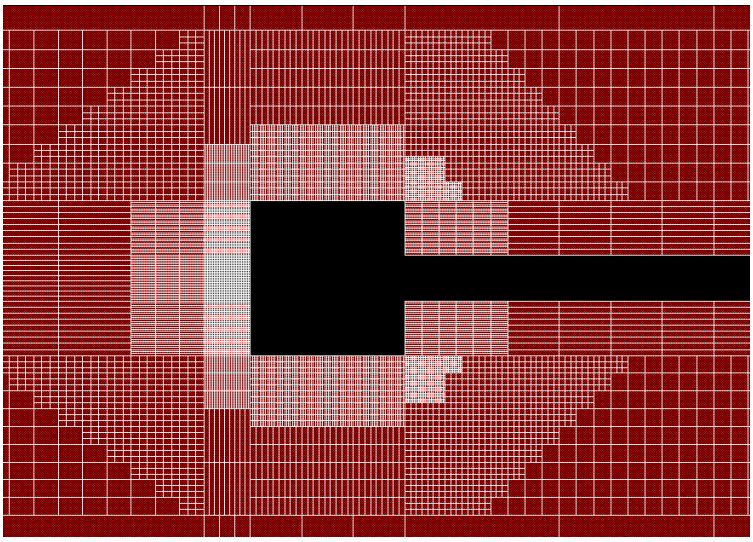

Figure 3.4: Screenshot of the *Xic*© design software in which Fasthenry© is implemented. The discretization grid of the area around the washer hole was chosen to be much smaller than in the rest of the groundplane area.

Fasthenry© is implemented in the *Xic*© software we used for designing our structures and allows an easy way for discretization the conductor area. Figure 3.4 shows a screenshot of the washer groundplane and its hole. As mentioned before, the screening currents on the washer are following the inner path around the slit and the hole. In this area the discretization of the conductor was chosen to be much finer than in the rest of the conductor area in order to obtain more accurate results. Fasthenry© calculated an inductance of $L_{\text{washer}} = 848$ pH in the frequency range from 0 - 10 GHz and for a thickness of $t_g = 300$ nm. This is more than 5 times the value obtained using Equation (3.6).

The other program used was the student version of 3D-MLSI©[1] which is also capable of simulating superconducting materials. In addition, one can visualize the current streamlines and the relative magnitude of the current densities. Unfortunately the program lacks the feature of local conductor discretization. Figure 3.5 (a) shows a screenshot of the complete washer and the

[1]M.M. Khapaev, Moscow State University, Dept. of Computational Mathematics and Cybernetics. Email: mkhap@pn.npi.msu.ru, http://www.cmc.msu.ru/vm/sotr/vmhap

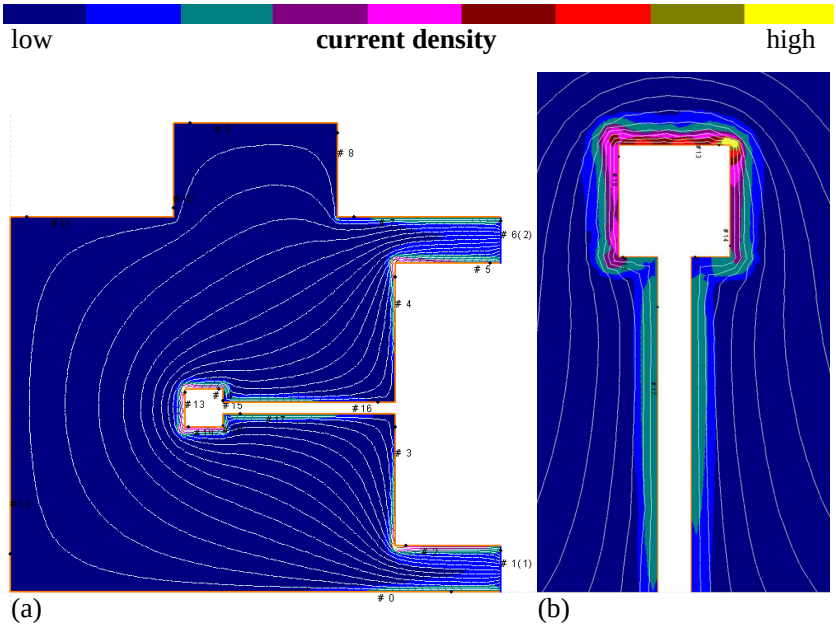

Figure 3.5: Screenshots of the 3D-MLSI© inductance extraction program. (a) Streamline plot of the Niobium groundplane. The terminals of the washer were chosen to be the two grounding pads that extend the groundplane area. (b) Magnified view of the relative current distribution around the washer hole.

current streamlines calculated with 3D-MLSI©. The calculated inductance was $L_{\text{washer}} = 880$ pH which is in good agreement with the value calculated with Fasthenry©. Figure 3.5 (b) shows a magnified view of the relative current densities flowing around the washer hole.

The large discrepancy between the simulated washer inductances and the inductance obtained by Equation (3.6) is rather disconcerting. The washer inductance is the dominating term in (3.3) because of the n^2 factor. On the one hand, Clarke and Mück used in reference [36] an inductance calculated by Equation (3.6). On the other hand, the measured resonance frequencies in reference [36] are a factor 2 - 3 smaller than predicted by theory. As we will see later on, the resonance frequency is proportional to $1/\sqrt{n^2 L_{\text{washer}}}$. The discrepancies in reference [36] could be assigned to a too small washer inductance. Therefore, we will take the result from Fasthenry© as many groups published results based on this simulation software, too. Furthermore, this result contains the effect of the slit which is clearly not included in Equation (3.6).

The typical length of our spiral input coil is in the range of 0.8 mm - 2.6

mm. Even for $n = 1$ the total inductance would be dominated by L_{washer} and therefore we will neglect the self-inductance of the coil. The characteristic impedance is then given by

$$Z_{\text{MS}} = \sqrt{\frac{n^2 L_{\text{washer}}}{lC}} \quad , \tag{3.7}$$

where l is the length of the input coil. The impedances of the MS section are increased by the presence of the slitted washer groundplane. The shortest sample has a length of 0.8 mm and 1 turn, the longest 2.6 mm and 4 turns. Therefore, the impedances of our MS sections lie in a range of 45.1 Ω - 100.2 Ω. Consequently, α_c and α_d of the MS section have to be modified while the expressions for the attenuation for the CPW can be adopted without change from section 2.3.4.

Modifications of the Microstrip attenuation

In section 2.3.3 we discussed the attenuation of a superconducting MS. In this model we assumed a conventional infinite groundplane. We now have to make corrections due to the presence of a slitted washer groundplane that effectively increases the characteristic impedance Z_{MS}. The expressions for conductor and dielectric losses from Equation (2.60) assumed a characteristic impedance $Z_0 = 15.7\ \Omega$ as given in Equation (3.1). Therefore, the calculated attenuation constants of section 2.3.3 have to be multiplied by a numerical factor that accounts for the impedance rise in presence of a slitted groundplane,

$$\alpha_c^{'} = \kappa \alpha_c \quad , \tag{3.8}$$

$$\alpha_d^{'} = \kappa^{-1} \alpha_d \quad , \tag{3.9}$$

where α_c and α_d are given in Equation (2.60). The numerical factor κ is given by

$$\kappa = \frac{15.7\ \Omega}{Z_{\text{MS}}} \quad , \tag{3.10}$$

where Z_{MS} is the actual impedance of the MS section given in Equation (3.7).

3.2.2 Transmission Line Analysis of the MR

In this section we want to model the MR by means of transmission line theory. Figure 3.6 shows a schematic view of our resonator and its outer circuitry. The actual resonator (dotted box) consists of two sections of transmission line with different impedance, length, and propagation constant $\gamma = \alpha + i\beta$. These sections are interconnected through a via and capacitively coupled to

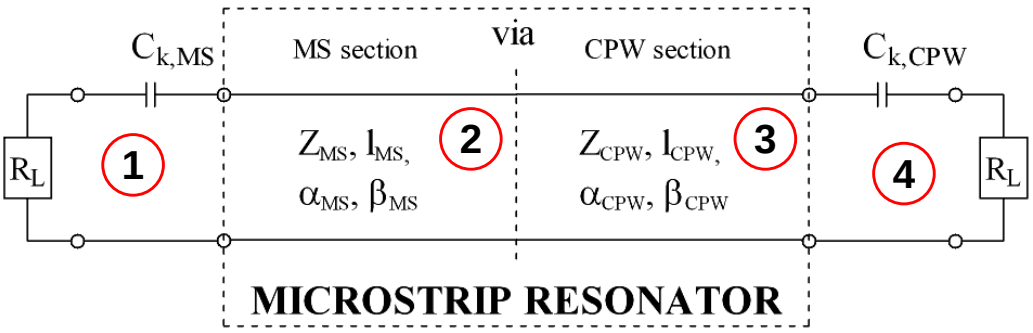

Figure 3.6: Schematic layout of the Microstrip Resonator. The different sections are denoted by numbers, $C_{\mathrm{k,MS}}$ and $C_{\mathrm{k,CPW}}$ are the coupling capacitors for the different transmission line sections, and R_{L} is the 50 Ω load modeling our outer circuitry.

the outer circuitry represented by a load resistance $R_{\mathrm{L}} = 50\ \Omega$.
In section 2.2.3 we derived an expression for the input impedance Z_{in} of a lossy transmission line terminated in an arbitrary load impedance Z_L,

$$Z_{\mathrm{in}}(l) = Z_0 \frac{Z_L + Z_0 \tanh(\gamma l)}{Z_0 + Z_L \tanh(\gamma l)} \quad . \tag{3.11}$$

For deriving Z_{in} for our MR we will use the following iterative procedure:

- Calculate the impedance $Z_1 = R_L - j/\omega C_{\mathrm{k,MS}}$ for section 1 as seen in Figure 3.6.
- Calculate $Z_{\mathrm{in},2}$ from Equation (3.11) with $Z_L = Z_1$ and $Z_0 = Z_{\mathrm{MS}}$ from section 2. Make sure to use the appropriate length l_{MS} and propagation constant $\gamma_{\mathrm{MS}} = \alpha_{\mathrm{MS}} + j\beta_{\mathrm{MS}}$. For the calculation α must be converted to [Nepers/m]. Note that α_{MS} is the sum of the impedance corrected expressions from Equations (3.8) and (3.9).
- Use this $Z_{\mathrm{in},2}$ as new load impedance Z_L and calculate $Z_{\mathrm{in},3}$ with $Z_0 = Z_{\mathrm{CPW}}$, l_{CPW} and γ_{CPW}.
- Calculate the overall input impedance in section 4, $Z_{\mathrm{in}} = Z_{\mathrm{in},3} - j/\omega C_{\mathrm{k,CPW}} + R_L$.

It is important to note that the propagation constant is a function of frequency, $\gamma \equiv \gamma(\omega)$, as α and β are frequency dependent. Therefore, $Z_{\mathrm{in}} \in \mathbb{C}$ is a frequency dependent quantity. At the resonance frequency, the real part of the input impedance will show a *finite* Lorentz peak in the frequency domain because we are treating lossy lines here. The impedance of an ideal line would diverge at the resonance frequency.
For the calculation of the phase constant β, the expression from Equation (2.23) was rewritten in terms of known quantities for the MS and CPW,

$$\beta_{\mathrm{MS}} = \omega \sqrt{\left(\frac{L_{\mathrm{washer}}}{l_{\mathrm{MS}}} + L_{\mathrm{MS}}\right) C_{\mathrm{MS}}} \qquad \text{for the MS,} \tag{3.12}$$

and

$$\beta_{\mathrm{CPW}} = L_{\mathrm{CPW}} \frac{\omega}{Z_{\mathrm{CPW}}} \qquad \text{for the CPW.} \tag{3.13}$$

Coupling Capacitors

In order to calculate the input impedance of our MR we have to know the value of our coupling capacitors. To obtain maximum power transfer between a resonator and a feedline, the resonator must be matched to the feed at the resonance frequency. The resonator is then said to be *critically coupled* to

the feed. In reference [27] an expression for C_k in case of critical coupling is given and may be rewritten for our case as,

$$C_k = \frac{b_c}{\omega Z_{\mathrm{MS}}} \quad , \tag{3.14}$$

where

$$b_c = \sqrt{\frac{\pi}{2Q}} \tag{3.15}$$

is the normalized coupling capacitor susceptance at resonance and Q is the quality factor of the resonator. As it is clear from Equation (3.14), a change in the length – and thus in the impedance of the MR – will change the value of the necessary capacitance for critical coupling. In reference [38] a general expression for Q is derived

$$Q \equiv \frac{\omega \cdot \text{ energy stored at frequency } \omega}{\text{average power loss at frequency } \omega} \quad , \tag{3.16}$$

which can be rewritten in terms of α and β as

$$Q = \frac{\beta}{2\alpha} \quad . \tag{3.17}$$

Here, α and β are the attenuation and phase constant at the resonance frequency. For the purpose of Circuit-QED (external[2]) quality factors $Q > 10^4$ are necessary. The theoretical calculated values for α and β of our MR yield a maximum (internal) quality factor of $Q \simeq 3 \cdot 10^4$ leading to a $b_c \approx 7.236 \cdot 10^{-3}$. Therefore, the minimum and maximum values of C_k for critical coupling are estimated to be

$$C_{\mathrm{k,min}} = \frac{7.236 \cdot 10^{-3}}{2\pi \cdot 10 \text{ GHz} \cdot \ 100.2\ \Omega} \approx 1.1 \text{ fF} \quad , \tag{3.18}$$

$$C_{\mathrm{k,max}} = \frac{7.236 \cdot 10^{-3}}{2\pi \cdot 1 \text{ GHz} \cdot \ 45.1\ \Omega} \approx 25.5 \text{ fF} \quad , \tag{3.19}$$

[2]The terms *internal* and *external* quality factor will be explained on page 59

in the frequency range from 0 - 10 GHz.
For implementation in our CAD designs we have to extract the capacitance out of the geometry of the specific capacitors. Therefore, we used the capacitance extraction program FastCap© that is, like FastHenry©, included in the *Xic*© design software. It is very important to treat the coupling capacitors for the MS and CPW sections separately: Firstly, because the groundplanes in the CPW section have strong influence on the value of C_k and secondly because the dielectric beneath is different for these sections.

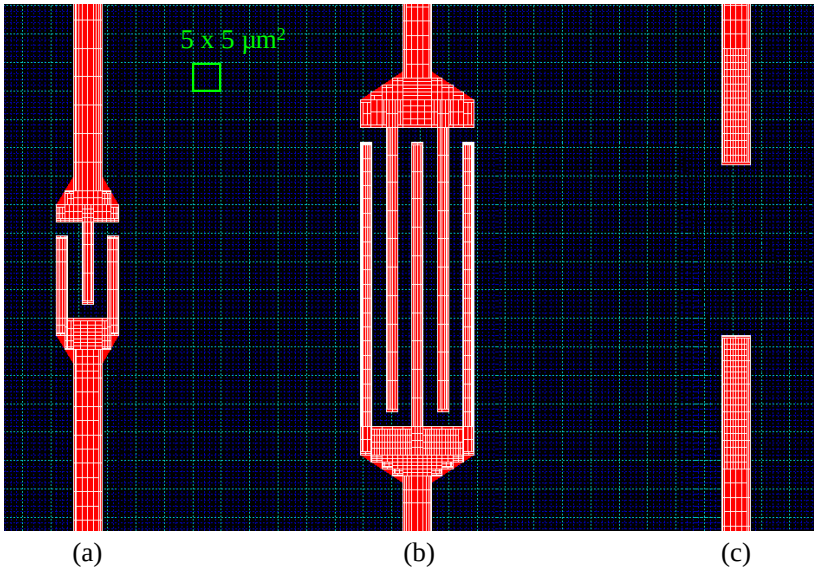

Figure 3.7: The three types of coupling capacitors (red) realized in our resonators. (a) and (b) represent interdigital finger capacitors while (c) is simply a gap capacitor. The discretization grid (white) of the FastCap© software tool is indicated.

In general, three different types of capacitors are realized in our designs. Figure 3.7 (a) and (b) are showing *interdigital finger capacitors* while (c) represents a simple *gap capacitance*. The green square in Figure 3.7 has an area of 25 μm^2. A photograph of the different capacitors in the CPW section is shown in Figure 3.8.
The MS and CPW sections of every resonator are equipped with the *same* coupling capacitor though, as mentioned before, the value of $C_{\mathrm{k,CPW}}$ is dif-

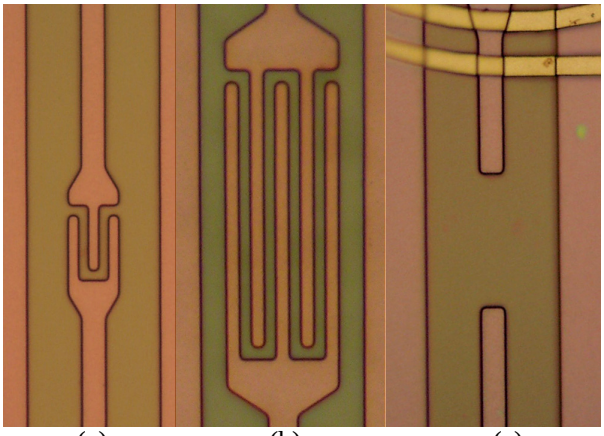

Figure 3.8: Photograph of the three different coupling capacitors discussed previously. (a) and (b): interdigital finger capacitors; (c): gap capacitance, here with a gap width of 30 μm. In (c) a small part of the spiral input coil can be seen. Note, that due to fabrication processes the edges are not sharp as designed in the CAD program.

ferent from $C_{\mathrm{k,MS}}$. In addition the CPW section is realized with different aspect ratios leading also to slightly different coupling capacitances. Table 3.2 lists values for some of the coupling capacitors realized in our designs.
The indices s, b, and g refer to the capacitors (a),(b), and (c) in Figure 3.7, respectively. The number after g stands for the width of the gap in μm. Capacitors in the CPW section have an additional number after the comma, indicating the center strip width of the CPW.
Table 3.2 lists approximate values since the fabrication at *Hypres, Inc.* involves photolithographic and etching processes. Thus, the size of structures on the wafer may differ somewhat from the design layout. The *Hypres, Inc.* design rules (see reference [26]) state the following biases for the different layers:

- MS-layer: (-0.2 ± 0.25) μm
- CPW-layer: (-0.3 ± 0.25) μm

Capacitor	Value [fF]
C_{s}	1.7
C_{b}	6.8
C_{g5}	0.6
C_{g10}	0.5
$C_{\mathrm{s,5}}$	1.8
$C_{\mathrm{s,20}}$	2.0
$C_{\mathrm{b,20}}$	10.0
$C_{\mathrm{g5,20}}$	1.4
$C_{\mathrm{g10,20}}$	0.9

Table 3.2: Values for the coupling capacitors calculated by FastCap©. The indices s, b, and g stand for *s*mall, *b*ig, and *g*ap, respectively. The number after g is the width of the gap in μm. A comma followed by a number stands for the capacitors in the CPW section, the number is the width of the CPWs center strip.

Quality Factors – Over- and Undercoupled Resonators

The quality factor defined in the preceding section is the *internal quality factor* Q_{int} of the resonant circuit in the absence of any loading effects caused by external circuitry. In practice, however, a resonant circuit is invariably coupled to external circuitry giving rise to the definition of an *external quality factor* Q_{ext}. Then, the overall, or loaded quality factor Q_{L} can be expressed as

$$\frac{1}{Q_{\mathrm{L}}} = \frac{1}{Q_{\mathrm{int}}} + \frac{1}{Q_{\mathrm{ext}}} \quad . \tag{3.20}$$

In Appendix B an expression for the external quality factor in dependence on known quantities is derived. The important fact is, that there are two regimes for our MR. On the one hand, if C_k is small enough, the resonant circuit will be *undercoupled* and the measured quality factor $Q_L \approx Q_{\mathrm{int}}$. On the other hand when C_k is large, the resonant circuit is said to be *overcoupled* allowing the measurement of $Q_L \approx Q_{\mathrm{ext}}$. As mentioned before, for Circuit-QED experiments an external quality factor of $Q_{\mathrm{ext}} > 10^4$ is favorable.
For *any* frequency the normalized susceptance b_c of a coupling capacitor C_k of our MRs may be written as

$$b_c = \omega C_k Z_{\mathrm{MS}} \quad . \tag{3.21}$$

Remember, that Equation (3.15) was only valid at the resonance frequency. Therefore, we can conclude:

$$C_k < \frac{1}{\omega Z_{\mathrm{MS}}} \sqrt{\frac{\pi}{2Q}} \rightarrow \text{undercoupled} \rightarrow Q_{\mathrm{int}} \tag{3.22}$$

$$C_k > \frac{1}{\omega Z_{\mathrm{MS}}} \sqrt{\frac{\pi}{2Q}} \rightarrow \text{overcoupled} \rightarrow Q_{\mathrm{ext}} \tag{3.23}$$

Actually, this discussion is only reasonable for the MS section of our MRs. Due to the very short length of our CPW section its internal quality factor is in the range of 100-300 leading to a b_c ten times larger than that for the MS. Therefore, the capacitors at the CPW section should be a factor ten times larger which is impractical for our designs.

3.3 Resonance Frequencies

In the preceding section we derived a way to calculate the resonance frequencies of our MRs by means of transmission line theory. However, the standard expression for calculating the *fundamental* resonance frequency of an electromagnetic resonator is found in many textbooks (e.g. [39]) and is given by

$$f_0 = \frac{v_{ph}}{2l} \quad , \tag{3.24}$$

where $v_{ph} = (LC)^{-1/2}$ is the phase velocity of the wave and $l = \lambda/2$ is the length of the resonator. L and C are quantities given per unit length. For our MR we have to include the increase of the inductance due to the presence of the slitted groundplane. Therefore the fundamental resonance frequency occurs at

$$f_{0,\lambda/2} = \frac{1}{2\sqrt{(lL + n^2 L_{\mathrm{washer}}) \cdot lC}} \quad . \tag{3.25}$$

The value of the resonance frequency is, as mentioned before, dominated by

the inductance of the washer. We neglected here the contribution from the short CPW section. The resonator is equivalent to a parallel tuned circuit. Higher order resonance frequencies are easily calculated from Equation (3.25),

$$f_{n,\lambda/2} = f_{0,\lambda/2} + n \cdot f_{0,\lambda/2} \quad , \; n \in \mathbb{N} \quad . \tag{3.26}$$

In the next chapter we will compare the measured resonance frequencies with the one obtained by the transmission line model and by Equations (3.25) and (3.26).

Chapter 4

Experimental Results

4.1 Introduction

In this chapter, the S-parameter measurements of several Microstrip Resonators (MR) are presented. The critical temperature T_c of a MR was determined in a SQUID magnetometer. The relevant dimensions of the MRs are summarized in Table 4.1 on page 76. A complete overview over all produced samples is found in Appendix C. We will begin with the presentation of the measurement setup, the sample box, and the different printed circuits boards used to mount the MRs. A brief introduction to S-parameters will be followed by a discussion of the calibration scheme. After the presentation of the experimental results we will give a conclusion and an outlook concerning improvements of the MR design and the calibration scheme. Finally, the cryogenic wafer probing system – allowing for measurements at 4.2 K without outer circuitry (e.g. bonding wires and printed circuit boards) – will be presented.

4.2 Measurement Setup

Figure 4.1 shows a schematic of the measurement setup. The setup consists of a cryostat where the device under test (DUT) is mounted onto a sample holder. A HP8722D network vector analyzer (NVA) is connected to the two ports of the DUT via coaxial cables and V-to-SMA adapters[1]. The tem-

[1]These adapters were necessary as the same measurement setup was also used by another student. For his experiments, V connectors were a crucial component so the coaxial

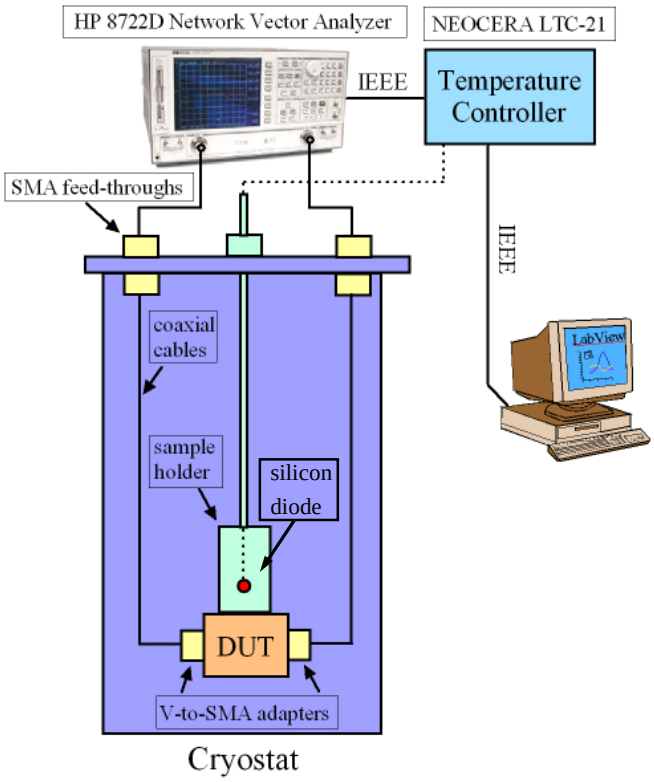

Figure 4.1: Schematic measurement setup. The DUT is mounted onto a sample holder and cooled down in a cryostat to a base temperature of 4.2 K. A HP8722D network vector analyzer (NVA) is connected to the DUT via coaxial cables, allowing S-parameter measurements at different temperatures. The temperature was read out using a NEOCERA LTC-21 temperature controller and a silicon diode attached to the outer surface of the sample holder (red dot). The NVA was controlled by LabView© via IEEE.

perature was measured using a NEOCERA LTC-21 temperature controller (TC) and a silicon diode attached to the outer surface of the sample holder. Since the measurement calibration is temperature dependent (c.f. section 4.4) it was essential to monitor the temperature during the measurement. The NVA and TC were read out via IEEE interface using a PC equipped with the LabView© software package. Furthermore, a 90 Ω heating resistor was attached 10 cm below the sample holder and connected to the analog heater output of the TC. This heating resistor was used to speed up the evaporation of liquid helium.
Most measurements were carried out using an output power of the NVA of $P_{\text{out}} = -30$ dBm. For output powers much lower than this value, the S-parameter measurements became very noisy though a *qualitative* change of the S-parameters in the power range from -5 dBm to -60 dBm could not be observed. The NVA is able to measure the S-parameters in a range from 50 MHz to 40 GHz with a maximum of 1601 data points per frequency sweep. Most of our measurements were carried out in a frequency range from 50 MHz to 12 GHz. The first fundamental resonance of all our measured samples was expected to be in that frequency range.

4.2.1 Sample Box and Printed Circuit Boards (PCB)

The measured MRs have an area of approximately 1.2 x 1.2 mm^2 (see Figure 3.1). The bonding pads for signal in- and output have a triangular shape with a base of 150 μm and a height of 180 μm, the grounding pads have an area of 100 x 100 μm^2. The most convenient way of connecting such small pads is to wire bond the pads to a much larger PCB and then to connect the PCB to the outer circuitry and the NVA.
Figure 4.2 (a) and (b) show the PCBs used for measurement and calibration, respectively. The circle in (a) indicates the position where the sample is glued. Both PCBs are designed in a CPW geometry with a center strip width of 1.6 mm and a gap of 0.8 mm. The dielectric is *RF-35* and has a permittivity of $\epsilon_r = 3.5$, a height of 0.76 mm, and the copper pattern has a thickness of 35 μm. With this dimensions, the software package *AppCad*© from Agilent Technologies© calculated an impedance of 50.3 Ω. It is im-

cables were originally produced with this connector type. However, SMA connectors are much more convenient for our purpose and thus we decided to use adapters (*INMET* 5154 and a combination of *INMET* 5149 & *Anritsu* 34VFK50).

portant to note, that the PCBs have an additional ground on the backside. Thus, for impedance calculation one has to make sure to use formulas for a so-called *conductor backed* CPW. The in- and output ports of the MR are then wire bonded to the center strip of the PCB in Figure 4.2 (a). The chamfered bend of the calibration PCB is a convenient way to reduce parasitic capacitances and bend reactances. The design for this mitered bend was adapted from reference [40].
Figure 4.2 (c) shows the brass sample box containing the calibration PCB. The SMA connectors are suitable for frequencies up to 18 GHz and the PCB center strip is connected with the SMA pin via silver glue. This is done primarily to reduce parasitic capacitances between the pin and the copper line and to improve electrical contact. A magnified view of the connector pin attached to the center strip is shown in Figure 4.2 (d). For measurements the sample box was closed with a bended brass top cover.

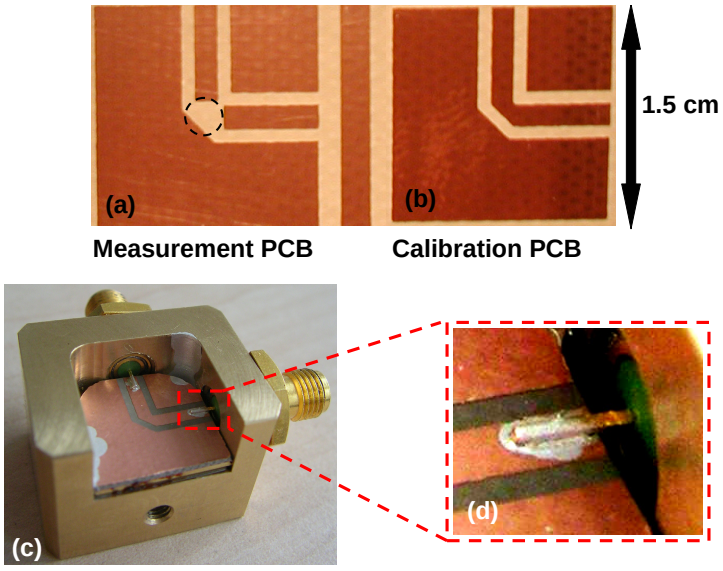

Figure 4.2: (a) 50 Ω measurement PCB. The circle indicates where the MR is glued. (b) 50 Ω calibration PCB. The chamfered bend is a convenient way of reducing parasitic reactances. (c) Brass sample box containing the PCB in (b). The box has inner dimensions of 1.5 cm x 1.5 cm and a height of 1.0 cm. The two SMA connector pins were attached to the center strip of the CPW PCB with silver glue. The grounding area of the PCBs were connected to the box with silver glue. (d) Magnified view of the SMA pin connected to the center strip.

Initially, we used a different box geometry as well as different PCBs (FR4 dielectric). The measurement results obtained with this old setup were not convincing. Therefore, the dielectric was changed from FR4 to RF-35 (more reliable at low temperatures and high frequencies), the dimensions of the brass box were reduced and the MR was mounted in a small recess in the PCB to allow for flat bonding wires [Stephan Manus, LMU München; private communication]. The hole was milled at the position indicated by the circle in Figure 4.2 (a). Figure 4.3 (a) and (b) show photographs from a bonded MR and the mounted sample box, respectively.

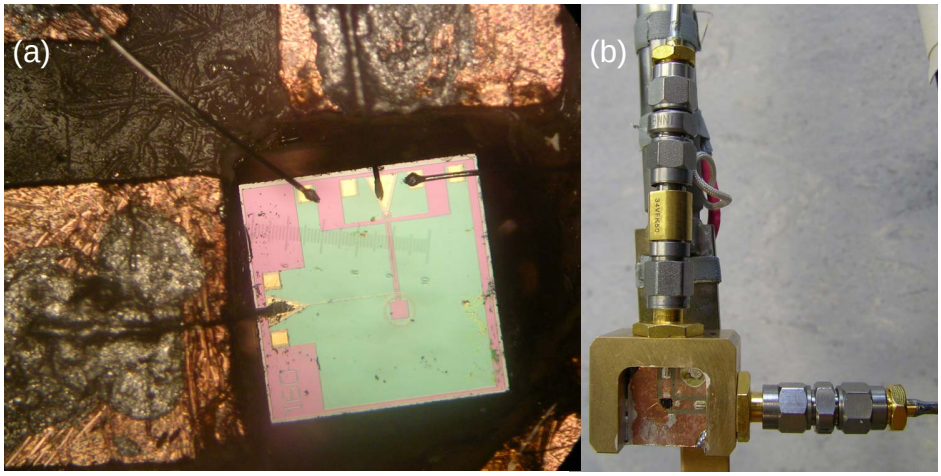

Figure 4.3: (a) Photograph of a bonded MR. The aluminum wire bonds over the copper line are covered with silver glue in order to reduce parasitic capacitances and improve the electrical contact. (b) Sample box with a bonded MR fastened to the sample holder.

4.3 S-parameters – The Scattering Matrix

A practical problem exists when trying to measure voltages and currents at microwave frequencies: direct measurements usually involve the magnitude and phase of a wave traveling in a given direction. One cannot simply connect a voltmeter or current probe and get accurate measurements due to the

impedance of the probes themselves and the difficulty of placing the probes at the desired positions. A representation in accordance with direct measurements, and with the ideas of incident, reflected, and transmitted waves, is given by the *scattering matrix*. The scattering matrix provides a complete description of the network as seen at its N-ports.
Consider the N-port network shown in Figure 4.4, where V_n^+ is the amplitude of the incident voltage wave at port n, and V_n^- is the amplitude of the reflected voltage wave from port n ($n = 1...N$). The scattering matrix, or

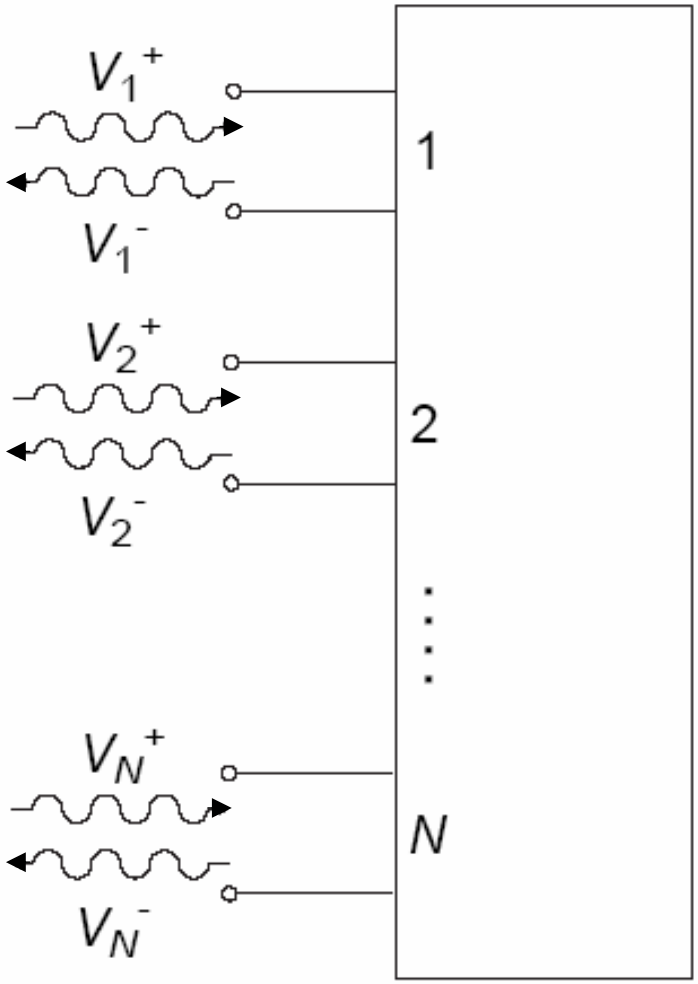

Figure 4.4: An arbitrary N-port microwave network.

$[S]$ matrix, is defined as

$$\begin{bmatrix} V_1^- \\ V_2^- \\ \vdots \\ V_N^- \end{bmatrix} = \begin{bmatrix} S_{11} & S_{12} & \cdots & S_{1N} \\ S_{21} & S_{22} & \cdots & S_{2N} \\ \vdots & \vdots & \ddots & \vdots \\ S_{N1} & S_{N2} & \cdots & S_{NN} \end{bmatrix} \begin{bmatrix} V_1^+ \\ V_2^+ \\ \vdots \\ V_N^+ \end{bmatrix} \tag{4.1}$$

or in short form

$$[V^-] = [S][V^+] \quad . \tag{4.2}$$

An element of the $[S]$ matrix can be written as

$$S_{ij} = \frac{V_i^-}{V_j^+}\Big|_{V_k^+ = \ 0 \text{ for } k \neq j} \quad . \tag{4.3}$$

That means the S-parameter S_{ij} can be found by driving port j with an incident wave of voltage V_j^+ and measuring the reflected wave amplitude V_i^- at port i. The incident waves on all other ports $k \neq j$ have to be zero, which means that these ports have to be terminated in matched loads in order to avoid reflections. It is important to emphasize that the reflection coefficient Γ_i looking into port i is not equal to S_{ii}, unless all other ports are matched. Similarly, the transmission coefficient from port j to port i is not equal to S_{ij}, unless all other ports are matched. The S-parameters of a network are inherent properties of the network and *defined* under the condition that all ports are matched. The accuracy of a S-parameter measurement depends strongly on this condition.
S-parameter measurements can be performed in frequency and time domain using a network vector analyzer (NVA). For a short explanation of the operation principle of the NVA see reference [27], a more detailed introduction (also about S-parameters and error correction) is given in reference [41].
The HP8722D NVA displays the S-parameters in a logarithmic magnitude format though S-parameters are inherently complex, linear quantities. The conversion between these two different formats is given by

$$S_{ij}[\text{dB}] \equiv 20 \cdot \log(|S_{ij}|) \quad , \tag{4.4}$$

$$|S_{ij}| \equiv 10^{\frac{S_{ij}[\mathrm{dB}]}{20}} \quad . \tag{4.5}$$

Point of interest

Figure 4.5 visualizes the S-parameters for a two-port network. A network is called *reciprocal* when $S_{ij} = S_{ji}$, which implies $[S] = [S^T]$. Practically

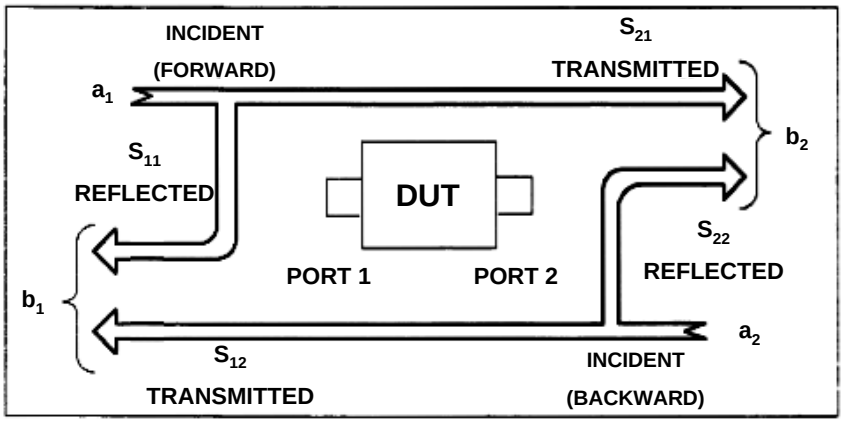

Figure 4.5: S-parameters for a two-port network.

this means that interchanging the input and output ports does not change the transmission properties. Our resonators, as passive devices consisting of a piece of transmission line, are a good example for reciprocal networks. This property of our network was verified during several experiments. Non-reciprocal networks are for example amplifiers and ferrite devices. Furthermore, a network is called *lossless* when the S matrix is unitary, $[S^\dagger] = [S^T]^{-1}$. This means that for a lossless network the dot product of any column of $[S]$ with the conjugate of that column gives unity, e.g. $|S_{11}|^2 + |S_{21}|^2 = 1$. However, this is not the case for our resonators.

An interesting example is a lossy resonator. Figure 4.6 shows the transmission and reflection spectrum for an ideal measurement. The peak in the

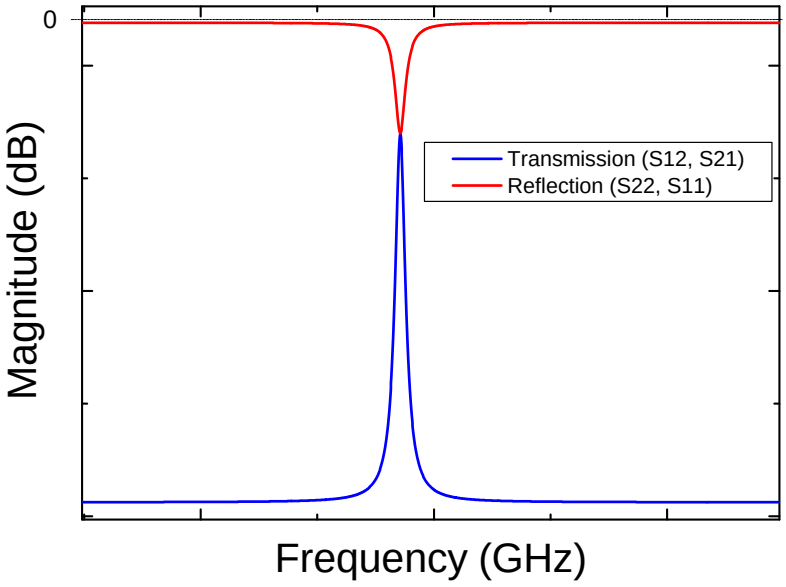

Figure 4.6: S-parameters for an ideal measurement of a lossy resonator.

transmission spectrum is accompanied by a corresponding dip in the reflection spectrum. The magnitude of S_{ij} at the resonance frequency is called *insertion loss* (IL).

4.4 Calibration of the Measurement Setup

In order to measure the S-parameters correctly the NVA must be calibrated with known calibration standards. These *calibration standards* are special connectors representing either a short, an open, or a broadband load termination. Our DUT is a two port device and the HP8722D provides six types of calibrations available for 2-port measurements although only the following three are important for us:

- S_{12} response calibration
- S_{11} 1-port calibration
- S_{22} 1-port calibration

A nice overview of the other calibration schemes is given in references [41, 42]. There the interested reader gets more detailed information about the type of error corrected, too.

4.4.1 Response Calibration – S_{12}

Response calibration is a normalized measurement in which a reference trace is stored in the network analyzers memory, and later on the measurement data is divided by the stored trace for normalization. This is the simplest calibration scheme to perform but only corrects two of the 12 possible systematic errors. The advantage of this error correction is the fact that only a 50 Ω through standard is needed which is provided by our calibration PCB in Figure 4.2 (b). Thus, we are able to perform a temperature dependent calibration[2] *and* we are able to remove the effects of the brass sample box as well as the attenuation in the PCB[3]. With this calibration scheme we are therefore able to measure the transmission through our MR *and* its bonding wires. The only way to measure the MR *without* the effects of bonding wires is to use a probe station. We will come to this topic later. Figure 4.7 (a) shows the calibration scheme for the S_{12} response calibration.
On resonance, the power transfer through our MR is maximum and therefore one should observe a peak at the resonance frequency in the S_{12} curve with a maximum magnitude of 0 dB.

[2]The previously mentioned calibration standards are very expensive devices that must be handled with much care. *In no case* one should cool down these standards to liquid helium temperatures or even liquid nitrogen temperatures. They should only be used at room temperature and thus, e.g. a temperature dependent full-2-port calibration, which would correct for all twelve systematic errors, is impractical.

[3]Remember, that both PCBs in Figure 4.2 have a designed impedance of approximately 50 Ω

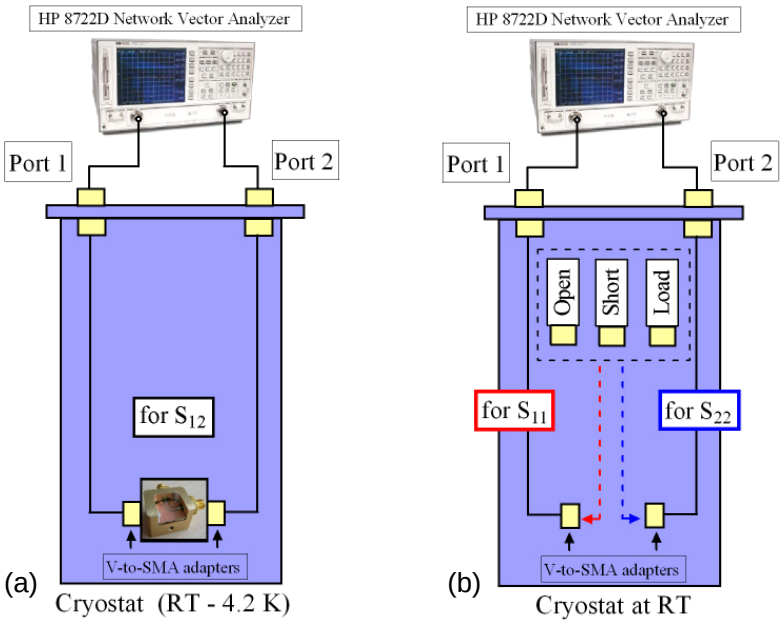

Figure 4.7: (a) Calibration scheme for the S_{12} response calibration. (b) Calibration scheme for the S_{11} and S_{22} 1-port calibration

4.4.2 Reflection calibration – S_{11} and S_{22} 1-port calibration

The S_{ii} parameters are a measure for the reflected power at port i. As just mentioned, on resonance the power transfer through the MR is maximum and thus, the S_{ii} curve should have dip at the resonance frequency. The S_{ii} 1-port calibration needs *all* three calibration standards (short, open, and broadband load). Therefore it is not possible to make a temperature dependent calibration (see the footnote on page 72). Instead we have to calibrate at room temperature (RT) and then recall the saved data at 4.2 K. Furthermore, a S_{11} measurement at 4.2 K then requires to connect the (matched) broadband load to port 2 of the cryostat SMA feed-through (and vice versa). Figure 4.7 (b) shows the calibration scheme for the S_{ii} 1-port calibration. Note, that the V-to-SMA adapters are included in the calibration data as the calibration standards are connected *after* the adapters.
In order to estimate the error we are inducing by neglecting the temperature dependent calibration data for the S_{ii} measurements, we performed a S_{12} calibration measurement with the coaxial cables and the adapters connected

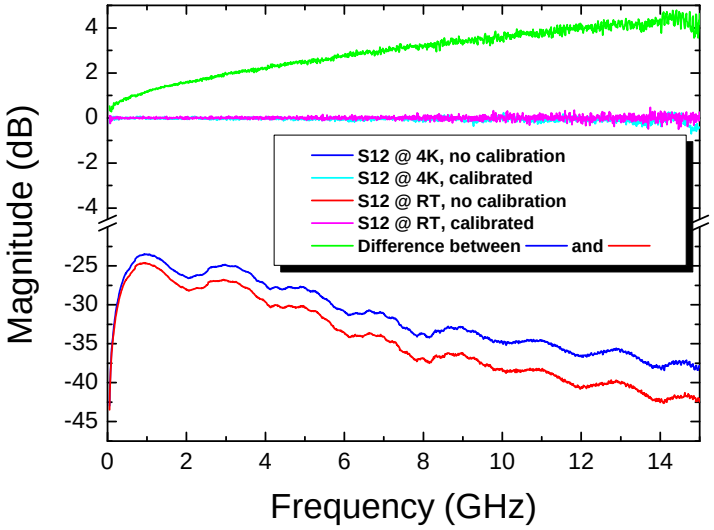

Figure 4.8: S_{12} measurement showing the uncalibrated and calibrated data of the cryostats coaxial cables and adapters. The green curve is the difference between the uncalibrated data at 4 K and RT.

via a SMA female/female through connector. Figure 4.8 shows the collected data. The green curve is the difference between the non-calibrated data collected at 4 K and at RT. Most of our S_{ii} measurements are performed up to a frequency of 10 GHz. At this frequency, the error induced by neglecting the temperature dependence of our whole setup is approximately 3.6 dB. This difference is due to the temperature *and* frequency dependent attenuation of the coaxial cables. In the measurements discussed in this chapter we will present the raw data and thus the reader should keep in mind that the S_{ii} spectra may exceed the 0 dB line.
The presented calibration schemes have one major disadvantage. After recording the temperature dependent calibration data for one set of parameters of the NVA, e.g. power or frequency span, it is not possible to make *any* changes to these parameters. In order to resolve a certain peak more clearly for example, a measurement with a different frequency span as in the calibration measurement would be necessary. This however, requires a new calibration of the whole setup.

4.5 Measurements

4.5.1 T_c-Measurement

In order to determine the value of T_c a measurement with a SQUID magnetometer was performed. The *Quantum Design*© SQUID was operated in the

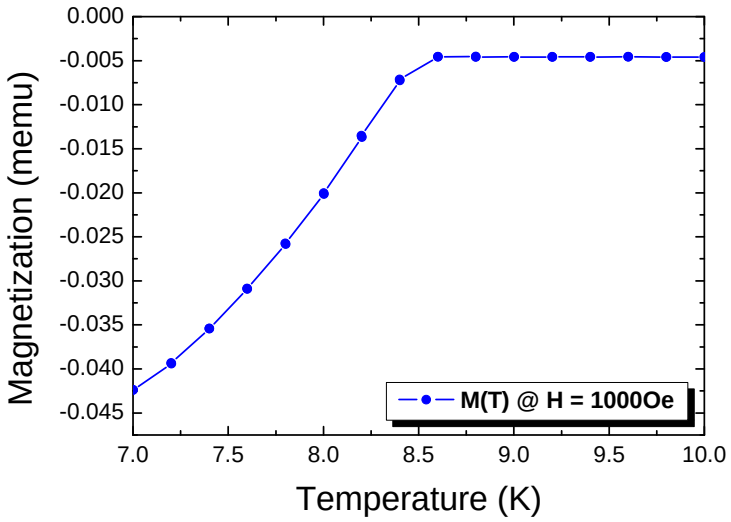

Figure 4.9: SQUID measurement for the determination of T_c. The applied field was set to 1000 Oe.

dc-mode. With an applied field of 1000 Oe we measured the magnetization dependent on the temperature. For temperatures lower than T_c the magnetization drops significantly due to the Meissner-Ochsenfeld-effect. Figure 4.9 shows the measured data and the critical temperature of our niobium MR is determined to be

$$T_c \approx 8.6 \text{ K} \quad . \tag{4.6}$$

This value is smaller than reference values of $T_c(\mathbf{H} = 0) = 9.20 \text{ K} - 9.46 \text{ K}$ found in literature which is at least partially due to the significant measuring filed. A detailed introduction into the working principles of SQUIDs is found, e.g. in reference [4].

Sample	**37**	**133**	**148**	**1**
n	3	3	3	3
l_{MS} [μm]	2140	2140	2447	2140
Z_{MS} [Ω]	84.2	84.2	79.0	84.2
C_{MS} [fF]	1.7	0.5	1.7	1.7
l_{CPW} [μm]	125	125	460	125
w_{CPW} [μm]	20	20	20	5
Z_{CPW} [Ω]	39.3	39.3	39.3	75.3
C_{CPW} [fF]	2.0	0.9	–	1.8
f_0 [GHz]	5.326	5.331	4.966	5.329
f_1 [GHz]	10.651	10.662	9.932	10.653
$f_{0,\lambda/2}$ [GHz]	5.335	5.335	4.977	5.335
$f_{1,\lambda/2}$ [GHz]	10.670	10.670	9.954	10.670
Washer	*n.g.*	*g.*	*g.* & *n.g.*	*g.*

Table 4.1: Properties of the measured MRs. n is the number of turns of the spiral input coil. $f_{0,1}$ are the fundamental and first harmonic resonance as calculated with the TLM. $f_{0,\lambda/2}$ and $f_{1,\lambda/2}$ are the fundamental and first harmonic resonance frequency calculated with Equations (3.25) and (3.26), respectively. The abbreviations *n.g.* and *g.* stand for *not grounded* and *grounded*.

4.5.2 Resonance Frequencies and Quality Factors

In this section we will present the S-parameter measurements of our MRs. We did not perform any phase measurements as the resonances should be clearly visible and the quality factors can be extracted by fitting[4] a Lorentzian to the measured transmission data at $T = 4$ K. The measured resonance frequencies are compared to the theoretical values obtained by the transmission line model (TLM) of section 3.2.2 and Equation (3.25). Table 4.1 lists the characteristic properties of the MRs. 28 different experiments were carried out and the measured data often was not consistent. Samples with very similar geometry showed very different transmission and reflection spectra. The data presented in the following sections represents the data where we could *clearly* observe peaks and corresponding dips in our spectra.
I want to point out the two major measurement schemes that were performed. For some measurements we did not ground the washer (floating groundplane)

[4]For the fitting procedure we used *Origin 7.0*©.

while for other experiments the washer was grounded with a bonding wire of approximately 3 mm length. The bonding wire has a width of 30 μm and represents an inductor that is connected in series to the groundplane. In reference [38] an approximate formula for the inductance of short round wires is found,

$$L_{\text{bond}}\ [\text{nH}] = 0.2l[\ln(4l/d) - 1 + d/2l] \quad , \tag{4.7}$$

where l and d are the wires length and diameter in mm, respectively. Thus, the used bonding wire[5] for grounding has an inductance of $L_{\text{bond}} \approx 3$ nH. M. Mück and J. Clarke reported in reference [36] that in the case of a floating washer the resonance frequencies increased by a factor of approximately 1.6 and the quality factor by 3. The rise in the resonance frequency is explained by a stronger feedback from the washer to the spiral input coil via their distributed capacitance.

Washer not grounded – Sample 37 & 148

We first want to turn to those measurements where we did not ground the washer. Sample 148 has a special design, the perceptive reader may have recognized that in table 4.1 no value for the capacitor at the CPW section is given. This is due to the fact that we designed Sample 148 to have its second capacitor on the inner edge of the input coil as shown in Figure 4.10, though this is actually not a photograph of Sample 148 itself[6]. It is easy to adapt this change to the presented TLM in section 3.2.2. The value for the series capacitor at the CPW section is replaced by that of the MS section and it is implemented in section 3 rather than in section 1.
Figure 4.11 shows the calculated real part of the input impedance for Sample 37 and Sample 148 as calculated with the TLM. The value for the fundamental resonance of both samples is in excellent agreement with the value calculated with Equations (3.25) and (3.26). The small deviation is not surprising as Equation (3.25) does not take into account the presence of the

[5]We also included the shorter ($\sim$ 1 mm) bonding wires that connect our specimen with PCB feed line in the TLM. They were included in series with the coupling capacitors, but even though they have a quite high reactance in the frequency range from 0 - 10 GHz, no shift in the calculated resonance frequency could be observed.

[6]Sample 148 has a $w_{\text{CPW}} = 30$ μm but the capacitor in Figure 4.10 is the same as for Sample 148.

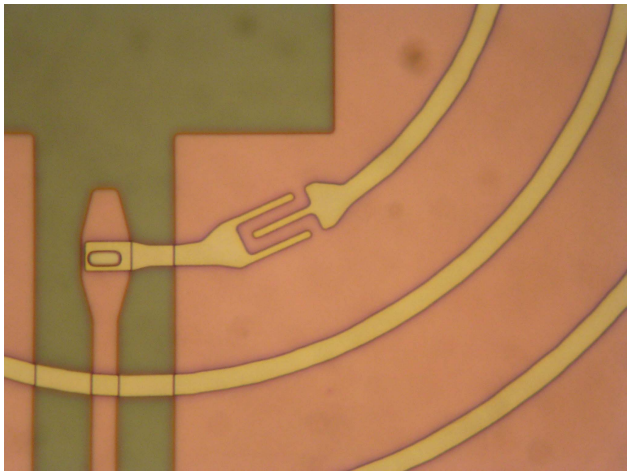

Figure 4.10: MR with the second capacitor at the inner edge of the spiral input coil. The capacitance is calculated to be 1.7 fF.

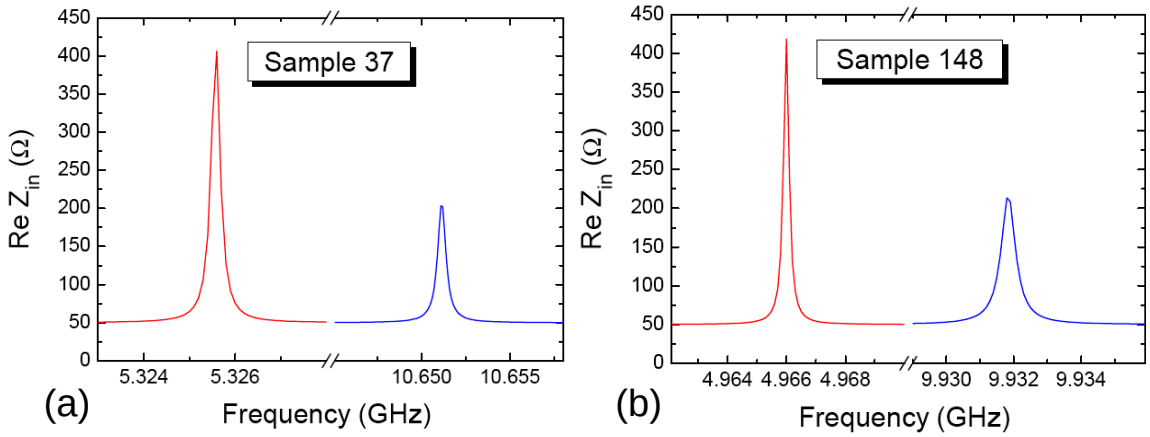

Figure 4.11: Real part of the input impedance versus frequency as calculated with the TLM of section 3.2.2. (a) Sample 37: fundamental resonance at $f_0 = 5.326$ GHz and first harmonic at $f_1 = 10.651$ GHz. (b) Sample 148: fundamental resonance at $f_0 = 4.966$ GHz and first harmonic at $f_1 = 9.932$ GHz.

very short CPW section. The second harmonics are at $f_2 = 15.977$ GHz (Sample 37) and $f_2 = 14.927$ GHz (Sample 148).
In reference [36] the authors observed that the first and second harmonic resonances are at higher frequencies as expected. They contributed their observation to the fact, that for higher order frequencies not all the current flowing in the resonator is in the same direction. Then, less current is forced around the slit and the hole and the inductance reflected into the input coil is reduced leading to higher resonance frequencies.
The measured S-parameters for Sample 37 are shown in Figure 4.12. The output power of the NVA was $P_{\text{out}} = -30$ dBm. For better clarity the S_{12} spectrum is shown from 2 - 10 GHz and for only 3 temperature values. At T = 4 K we can see a resonance peak at $f = 6.891$ GHz with a gain of approximately 4 dB. As expected, this peak is accompanied by a dip of roughly -5.8 dB in the S_{22} and -3.5 dB in the S_{11} spectrum. The second, much larger, dip at 7.276 GHz lacks the corresponding peak in S_{12}. The resonance vanishes at RT and shows a clear temperature dependence. At 40 K the resonance occurs at 6.958 GHz. This is quite astonishing as one expects a rise in the resonance frequency with lower temperature as observed in many other experiments, e.g. reference [43]. There are two additional peaks in the S_{12}

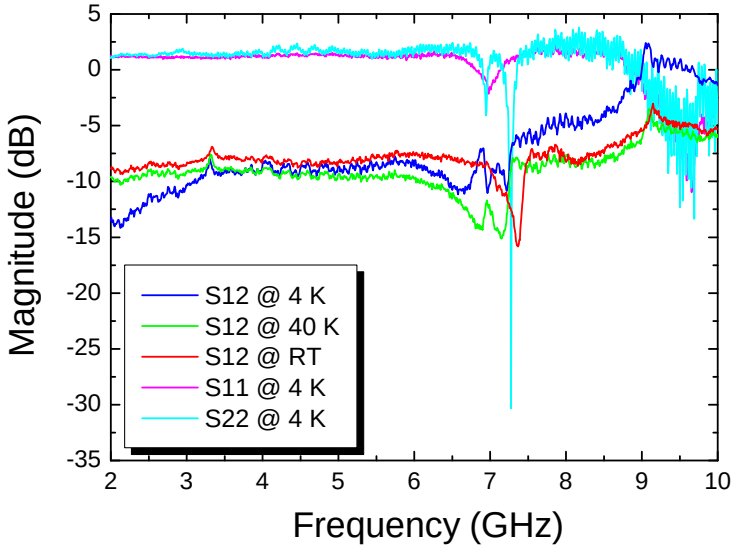

Figure 4.12: Measured S-parameters of Sample 37 (n.g.) at different temperatures.

spectrum. The very small peak at approximately 3.3 GHz, can not be assigned to our MR. Firstly, this peak has no corresponding dip in the S_{22} and S_{11} spectra, which is usually the strongest evidence for a resonance of our sample. Secondly, one sees neither an increase nor a shift of the peak position for different temperatures, just an overall reduction in magnitude, which can be clearly accounted for by the reduction of the attenuation for decreasing temperatures. Last but not least, this peak is also found in the spectrum of many other samples, e.g. Sample 148 and Sample 90, at *exactly* the same position. The second peak around 9 GHz is also observed for other samples (e.g. Sample 133) though with a less pronounced increase in magnitude as for Sample 37. This peak is not accompanied by a dip in the S_{ii} spectra and at $T = 4$ K the peak exceeds the 0 dB line, which is physically impossible[7]. A Lorentz fit to the S_{12} data at 4 K is shown in Figure 4.13. The fitted

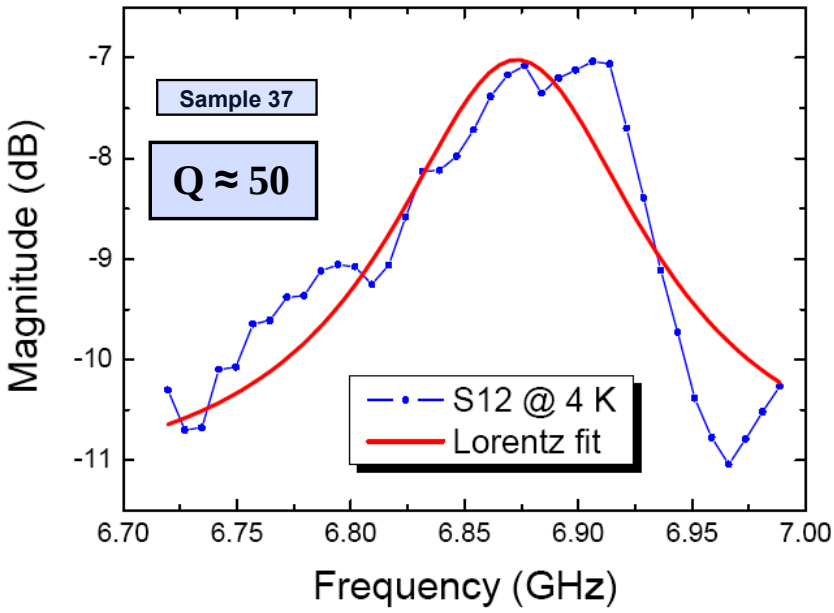

Figure 4.13: Lorentz fit to the S_{12} data of Sample 37 (n.g.) at $T = 4$ K.

peak frequency is $f_{\text{fit}} = 6.873$ GHz and the quality factor is determined by dividing the center frequency by the *full width at half maximum* (FWHM). This yields a relatively poor quality factor of $Q \approx 50$. Using Equation (3.22) we see that our MR should be undercoupled (Sample 37 has coupling capac-

[7]Remember that the S_{ii} spectra may exceed the 0 dB line.

itors like those in Figure 3.7 (a)), the measured quality factor is thus the internal quality factor Q_{int}. Frunzio et al. reported a $Q_{\text{int}} \approx 5000$ for a CPW resonator at $T = 4$ K. This value differs by a factor of 100 from our quality factor.
It is reasonable to fit for the washer inductance L_{washer} in order to match the observed resonance frequency. Assuming that the resonance we see is the fundamental $\lambda/2$ resonance and by using Equation (3.25) we get

$$L_{\text{washer,fit}} = 499 \text{ pH} \quad . \tag{4.8}$$

Inserting this result in the TLM and calculating the resonance frequency of the fundamental resonance yields $f_1 = 6.863$ GHz, which is in very good agreement with the observed resonance frequency.

We now turn to the measurement results for Sample 148. Figure 4.14 shows the S-parameter spectrum in the range from 2 - 10 GHz with $P_{\text{out}} = -30$ dBm. We see a resonance peak at 7.369 GHz which is accompanied by the corre-

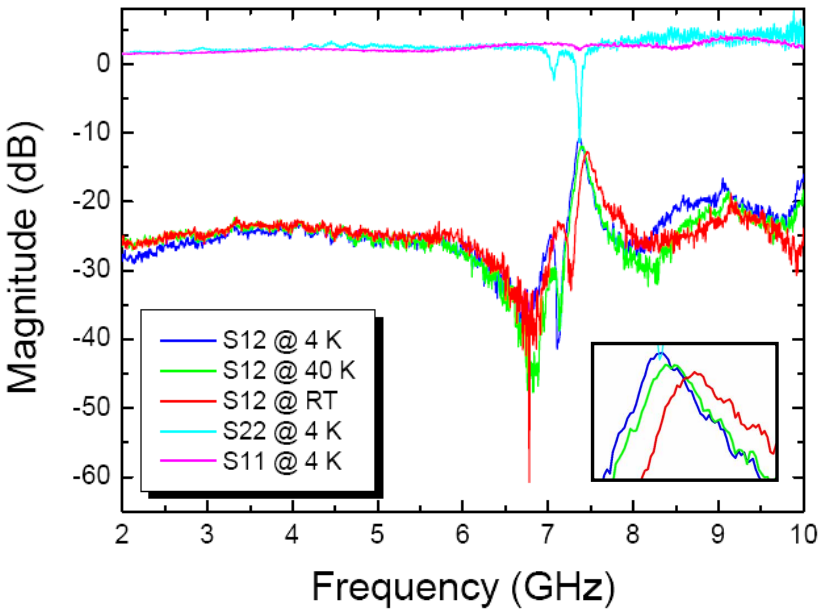

Figure 4.14: Measured S-parameters of Sample 148 (n.g.) at different temperatures. The inset shows the resonance in the region 7.2 GHz - 7.7 GHz.

sponding dips in the S_{22} (-14.0 dB) and S_{11} (-1.9 dB) spectra, though the dip in the S_{11} spectrum is very small. The inset illustrates the temperature dependent shift of the resonance peak. This resonance is approximately 2.4 GHz higher than expected from the TLM and Equation (3.25).
The Lorentz fit to the S_{12} data at $T = 4$ K is shown in Figure 4.15. The fitted peak frequency is $f_{\text{fit}} = 7.393$ GHz with a FWHM of 0.240 GHz yielding an internal quality factor of approximately 30 (like Sample 37, we are slightly undercoupled).

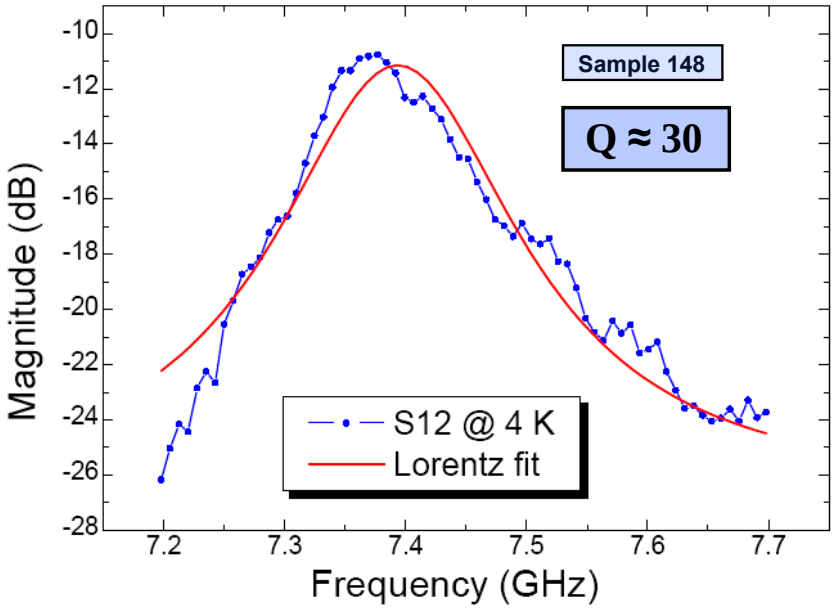

Figure 4.15: Lorentz fit to the S_{12} data of Sample 148 at $T = 4$ K.

A fit for the washer inductance assuming that the observed peak corresponds to the fundamental $\lambda/2$ resonance yields

$$L_{\text{washer,fit}} = 366 \text{ pH} \quad . \tag{4.9}$$

This result is not consistent with the fit obtained for Sample 37. Furthermore, from Equation (3.25) we see that the frequency of the fundamental resonance is inverse proportional to the length of a resonator, $f_{0,\lambda/2} \propto 1/l$. Sample 148 is about 300 μm longer than Sample 37 therefore we expect a lower resonance frequency (see Table 4.1). In our experiment, however,

the measured resonance frequency of Sample 148 is approximately 0.5 GHz higher. In addition, the question arises why the magnitude of the resonance peak of Sample 148 does not show the expected temperature dependence. The magnitude at 4 K, -10.7 dB, is only |-1.9 dB| larger than at RT. One would expect a much larger increase due to the effect of superconductivity which should especially reduce the conductor losses. Additionally, we observe the same temperature dependent shift as for Sample 37: the resonance frequency decreases for decreasing temperatures. This effect is not fully understood at this point. The poor internal quality factors are a factor of 100 (Sample 37) and 170 (Sample 148) smaller compared to the result L. Frunzio et. al in reference [43].

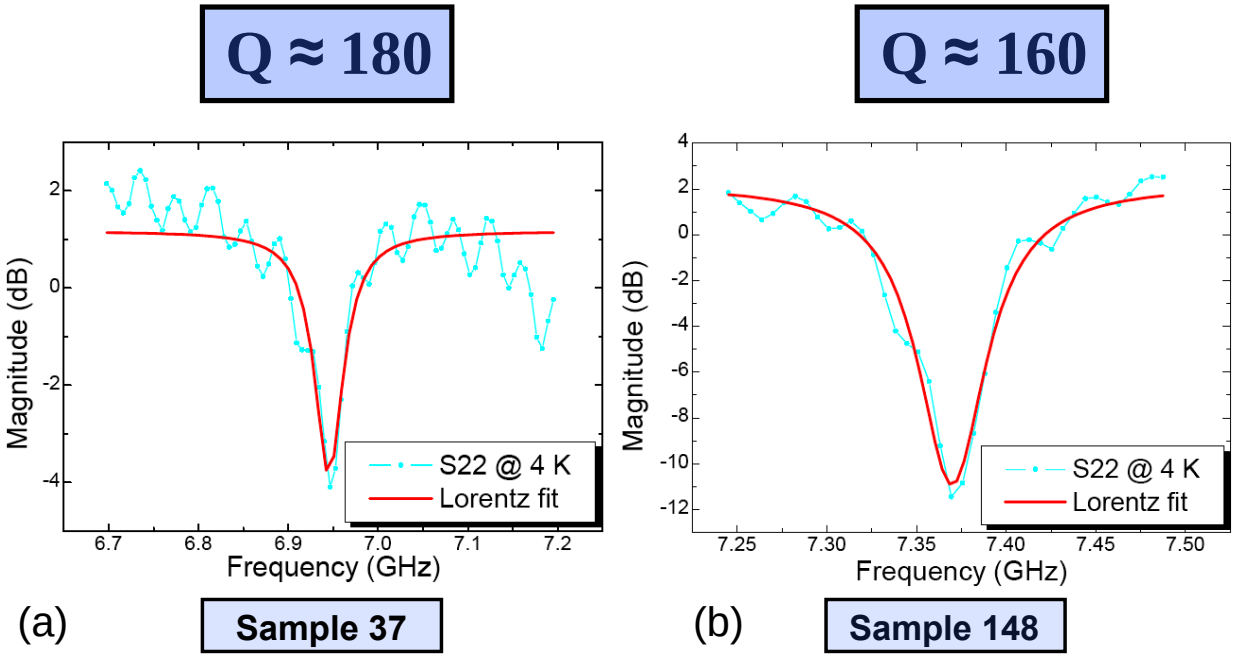

Figure 4.16: (a) Lorentz fit to the S_{22} data of Sample 37 at 4 K. (b) Lorentz fit to the S_{22} data of Sample 148 at 4 K.

In reference [15] Wallraff et al observed a shift of the resonance frequency – depending on the state of their qubit coupled to their cavity (see section

1.4) – in a transmission measurement. However, this shift should be observed in a reflection measurement, too. Then, the quality factors from the S_{ii} measurements are important and have to be extracted from the dips in the reflection spectra corresponding to the peaks in the transmission spectra [Robert Wanner, Lehrstuhl für Hochfrequenztechnik der TU München; private communication]. Figure 4.16 (a) and (b) show the Lorentz fit to the S_{22} data of Sample 37 and Sample 148 at $T = 4$ K, respectively. The quality factors of the S_{22} resonances increased by a factor of 3.6 (Sample 37) and 5 (Sample 148) in comparison to the transmission spectra. These quality factors are roughly a factor of 30 smaller compared to the values reported in reference [43].

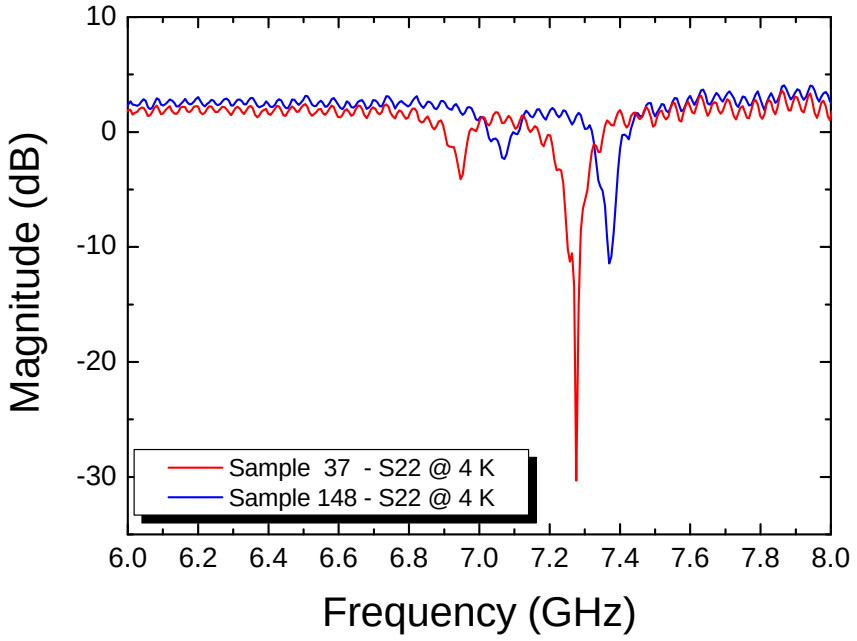

Figure 4.17: S_{22} data for Sample 37 & 148 at T = 4 K.

The reader may have recognized that the reflection spectra look similar for the two different samples. In Figure 4.17 we plotted the S_{22} data for Sample 37 and Sample 148 at $T = 4$ K in order to demonstrate that the observed resonances should indeed correspond to the different properties of our samples. The smaller dips in the reflection spectra are separated by 0.125 GHz while the larger dips are separated by 0.093 GHz. A systematic error in our measurement would imply an equidistant separation of both dips.

At the point of the via the reflection coefficient for both samples can be calculated using Equation (2.28),

$$\Gamma = \frac{Z_{MS} - Z_{CPW}}{Z_{MS} + Z_{CPW}} \approx 0.36 \quad . \tag{4.10}$$

Thus, $|\Gamma|^2 \approx 13\%$ of the incident power will be reflected at the via. Despite the fact that we do not observe two peaks in the S_{12} spectra, one could try to explain the two neighbouring dips in the S_{22} spectra assuming that a certain fraction of the energy is constantly reflected between the via and the open end – the coupling capacitor – of the MS section, while the other fraction of the energy is reflected between both coupling capacitors as expected from our $\lambda/2$ resonators. Thus, in the first case, the effective length of the resonator is smaller leading to a higher resonance frequency. However, this assumption is only valid for Sample 37 as Sample 148 has both coupling capacitors in the MS section (see Figure 4.10). Using Equation (3.25) the ratio of resonance frequencies f_{l_1}/f_{l_2} corresponding to different lengths l_1 and l_2 can be expressed as

$$\frac{f_{l_1}}{f_{l_2}} = \frac{\sqrt{l_2 L + n^2 L_{\text{washer}}}}{\sqrt{l_1 L + n^2 L_{\text{washer}}}} \quad . \tag{4.11}$$

With $f_{l_1} = 7.276$ GHz for $l_1 = l_{\text{MS}} = 2140\ \mu$m (second dip in Figure 4.17) and $f_{l_2} = 6.946$ GHz for $l_2 = l_{\text{MS}} + l_{\text{CPW}} = 2265\ \mu$m (first dip in Figure 4.17)we get

$$1.047 \approx \frac{f_{l_1}}{f_{l_2}} \neq \frac{\sqrt{l_2 L + n^2 L_{\text{washer}}}}{\sqrt{l_1 L + n^2 L_{\text{washer}}}} \approx 1.002 \quad , \tag{4.12}$$

where we used $L_{\text{washer}} = 499$ pH. This result is evident as the washer inductance is dominating the value of the resonance frequency[8].
The presented model is not able to explain the dips in the S_{22} spectrum of Sample 148. Furthermore, we should have observed similar reflection spectra like that in Figure 4.17 in more measurements, however, this was not the case. Thus, the assumption that the dips in the S_{22} spectra correspond to different effective lengths in our resonator is not correct. We have strong

[8]Neglecting the presence of the groundplane and using the figure of merit given in Equation (3.24) yields $1.047 \approx f_{l_1}/f_{l_2} = l_2/l_1 \approx 1.058$. Although the calculated values only differ by 2% the result is in contrast to the Ketchen-Jaycox model.

evidence that the observed resonances correspond to the different properties of our samples.

Washer grounded – Sample 148

We now want to turn to those measurements where we grounded the washer as shown in Figure 4.3 (a). Measurements on Sample 37 with a grounded washer were also performed, but unfortunately no peaks in the transmission spectrum could be observed. Sample 37 will be discussed later in combination with the data of Sample 1 so we first turn our attention to Sample 148. The spectra for an output power of $P_{\text{out}} = -30$ dBm are shown in Figure 4.18. The temperature dependent evolution of three peaks, one around 4.25 GHz

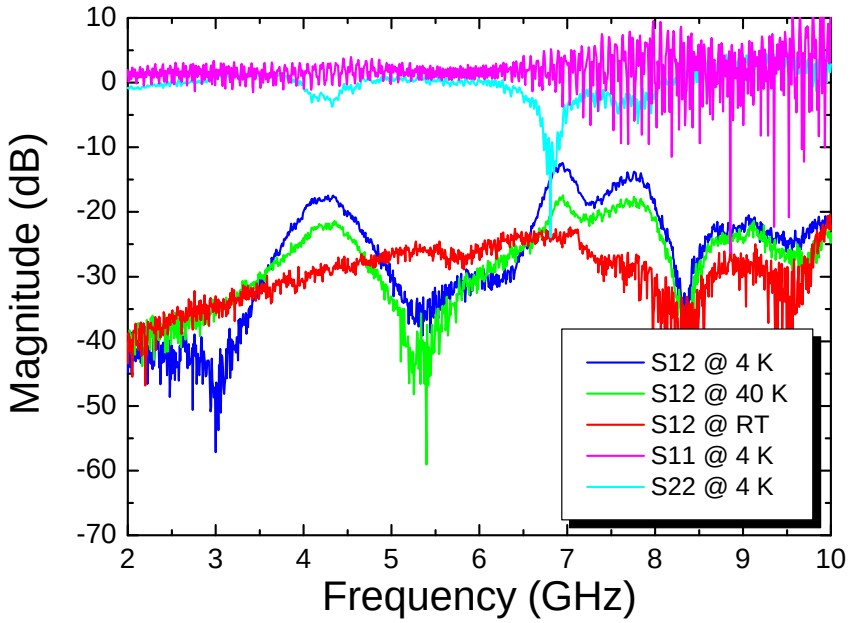

Figure 4.18: Measured S-parameters of Sample 148 (g.) at different temperatures.

and a double peak with center frequencies around 6.91 GHz and 7.78 GHz, can be clearly seen. For the peak at 6.91 GHz, the corresponding dip in the S_{22} spectrum (-23.9 dB) is shifted by approximately 0.11 GHz towards lower frequencies. This shift was also observed for Sample 133 and can actually not be explained by a measurement error as the other resonances and their corresponding dips occur more or less at the same frequency. Furthermore, in

comparison to the measurements with a floating groundplane, the S_{11} spectrum is very noisy and no dip at all can be observed. Let us first focus on the peak around 4.25 GHz.
The question arises to what extent we see the response of our resonator at this point. As mentioned before, Mück and Clarke observed a decrease in the resonance frequency of their device by a factor of 1.6 when grounding the washer. Assuming that the peak around 4.25 GHz is indeed our first harmonic and comparing to the measurement with the floating washer ($f_{\text{fit}} = 7.369$ GHz) we get a decrease by a factor of approximately 1.7, which would be in quite good agreement to reference [36]. In contrast to their measurements, however, we have a high decrease in the quality factor.

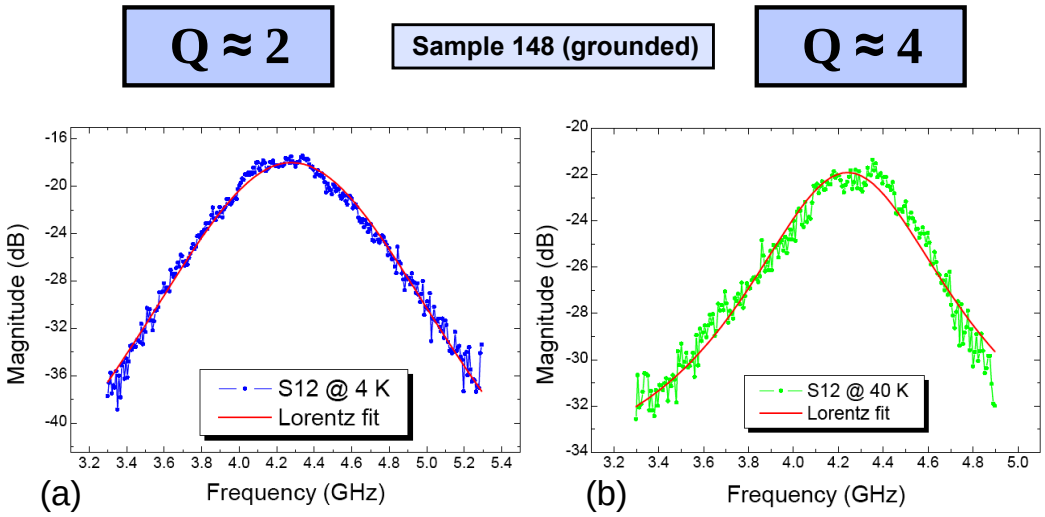

Figure 4.19: Lorentz fit to the S_{12} data of Sample 148 (g.) at (a) $T = 4$ K and (b) $T = 40$ K. K

Figure 4.19 (a) shows the Lorentz fit to the measured S_{12} data at $T = 4$ K. The fitted peak frequency is $f_{\text{fit}} = 4.278$ GHz with a FWHM of 2.409 GHz. Again this sample should be capacitively undercoupled, $Q \approx Q_{\text{int}}$. The quality factor, $Q_{\text{int}} \approx 2$, dropped by a factor of more than 15 in comparison to the previous measurement. As the resonance peaks are quite wide we also fitted the S_{12} data at $T = 40$ K in order to see the resonance shift

for different temperatures. The fit is shown in Figure 4.19 (b) and here the center frequency is calculated to be 4.241 GHz with a $Q_{\text{int}} \approx 4$. This is not consistent with previous measurements where we always observed a shift to lower frequencies with lower temperatures. However, the shift is very small. The measurments with the grounded washer are in better agreement with the TLM and Equation (3.25) compared to the measurement with the floating groundplane. A fit for the inductance of the washer groundplane assuming that the resonance at 4.278 GHz is the fundamental $\lambda/2$ resonance yields

$$L_{\text{washer,fit}} = 1159 \text{ pH} \quad . \tag{4.13}$$

This result could be explained by the presence of the bonding wire, effec-

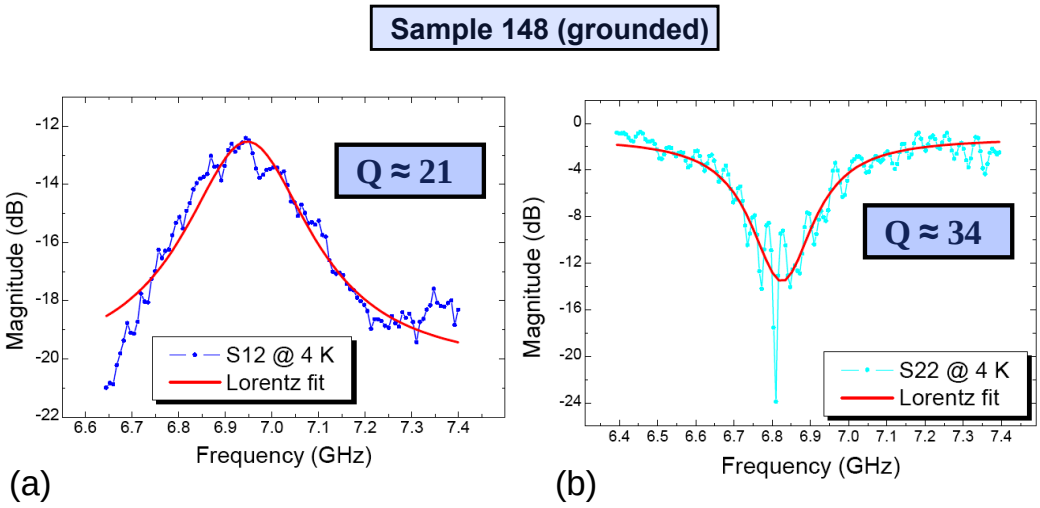

Figure 4.20: (a) Lorentz fit to the measured data of the resonance around 6.91 GHz at $T = 4$ K for (a) S_{12} and (b) S_{22}.

tively increasing the inductance of the groundplane. However, we can not observe the first harmonic $\lambda/2$ resonance, neither in S_{12} nor in S_{ii}.
The origin of the two peaks around 6.91 GHz and 7.78 GHz can not be explained by higher order $\lambda/2$ resonances. Both peaks clearly show the expected increase in magnitude for decreasing temperatures. However, the second peak lacks the corresponding dip in the reflection spectra. For the sake

of completeness we fitted the measured data for the S_{12} and S_{22} spectra of the resonance around 6.91 GHz. The fitted peak frequency is $f_{\text{fit}} = 6.947$ GHz with a FWHM of 0.336 GHz. Following the assumption that this resonance is the fundamental $\lambda/2$ resonance yields $L_{\text{washer,fit}} = 419$ pH which is not consistent with the results obtained so far. The quality factor of the fit to the S_{22} data represents a lower limit due to the noisy spectra.

Washer grounded – Sample 133

To shed some light on the measurement results obtained so far we performed an additional calibration scheme in parallel to the one mentioned in section 4.4. After the sample box was mounted into the cryostat, we performed a response calibration at RT *with the resonator already bonded*. The calibration data was saved onto a floppy disk. Then, we performed our usual measurement scheme. A $T = 4$ K the NVA was reset and the calibration data *containing the bonded sample* was recalled from the floppy disk. Thus, we get the S_{12} spectrum of our resonator at T = 4 K *normalized* to the spectrum at RT. Furthermore, we recalled this calibration data once more after heating up to RT. One then expects a flat line at 0 dB in the S_{12} spectrum assuming perfect reproducibility.

Figure 4.21 shows the conventional measurement of the S_{12}-parameters at 4 K, 40 K, and RT, respectively. As one can see from table 4.1, Sample 133 is constructed in the same way as Sample 37, except for the coupling capacitors which are in the case of Sample 133 gap capacitors with a gap of 10 μm. The TLM analysis of Sample 133 is essentially the same as for Sample 37, the fundamental resonance should occur at $f_0 = 5.331$ GHz, the first harmonic at $f_1 = 10.662$ GHz.
Around 6.0 GHz we see a shallow dip (-4.6 dB) in the S_{11} spectrum and another sharper dip (-8.6 dB) in the S_{22} spectrum around 7.1 GHz. Both dips lack the corresponding peaks in S_{12}, in fact we see also dips in the transmission spectrum. These dips are also seen at RT. A dip in the transmission spectrum implies that at this frequency less power is transmitted through our device. One would then expect that this fraction of power is either reflected or dissipated. The latter must be the fact for our case as reflected power would not cause dips in the S_{ii} spectra. Furthermore, these dips in S_{12} were not observed for Sample 37 when we grounded the washer. Another

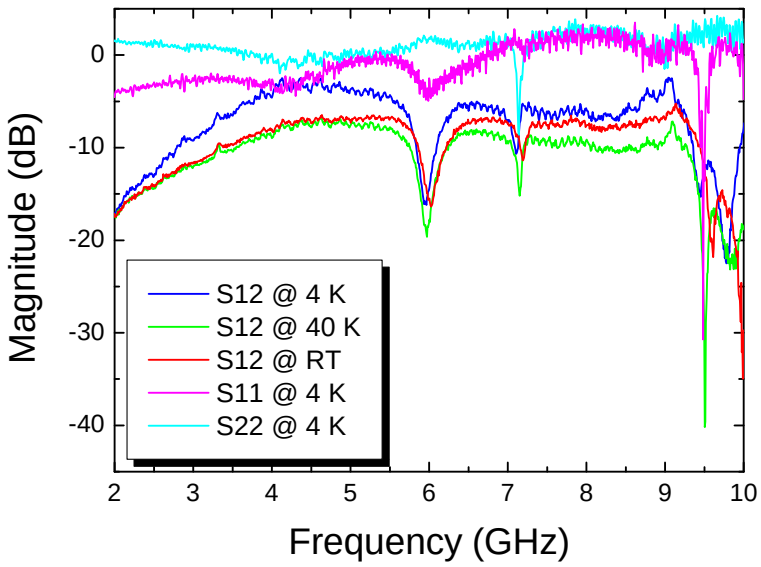

Figure 4.21: Measured S-parameters of Sample 133 (grounded washer) at different temperatures. The inset shows a magnified view of the resonance around 9.5 GHz

interesting fact is that for $T = 40$ K the dip is shifted to higher frequencies with respect to RT, while for $T = 4$ K it is shifted to lower frequencies. This behavior was not observed for any other specimen.
I want to turn the attention to the resonance near 9.5 GHz, which is magnified in the inset of Figure 4.21. This resonance shows the same temperature dependence, meaning the shift to lower frequencies for decreasing temperatures, as seen in the previous experiments. However, it needs some fantasy to see here the expected Lorentzian.
The S_{12} and S_{ii} spectra obtained with the additional calibration scheme[9] are shown in Figure 4.22. The resonance around 9.5 GHz is now clearly visible and shows the expected shape. A Lorentz fit shown in Figure 4.23 yields a quality factor of $Q_{\text{int}} \approx 56$ with a fitted center frequency of $f_{\text{fit}} = 9.592$ GHz. This resonance is more than 1 GHz lower in frequency than expected from the TLM and Equation (3.25). This result is in accordance with the previous measurement of Sample 148, where we observed a lower resonance as predicted by theory when grounding the washer. A fit for the washer inductance

[9]With this alternative measurement scheme the transmission spectrum may of course exceed the 0 dB line in contrast to the standard 50 Ω response calibration.

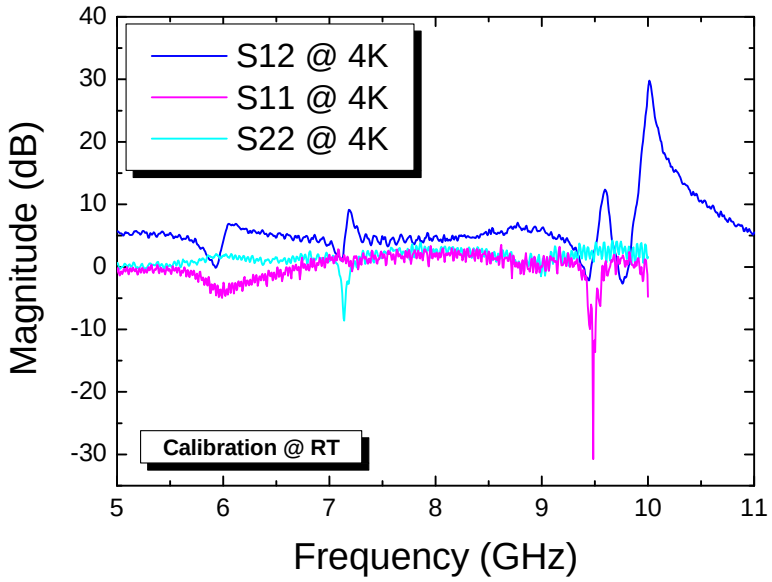

Figure 4.22: Measured S-parameters of Sample 133 (g.) at $T = 4$ K. As mentioned in the text, we used a different calibration scheme. This measurement shows the transmission at $T = 4$ K normalized to the transmission at RT in a frequency range from 5 - 11 GHz.

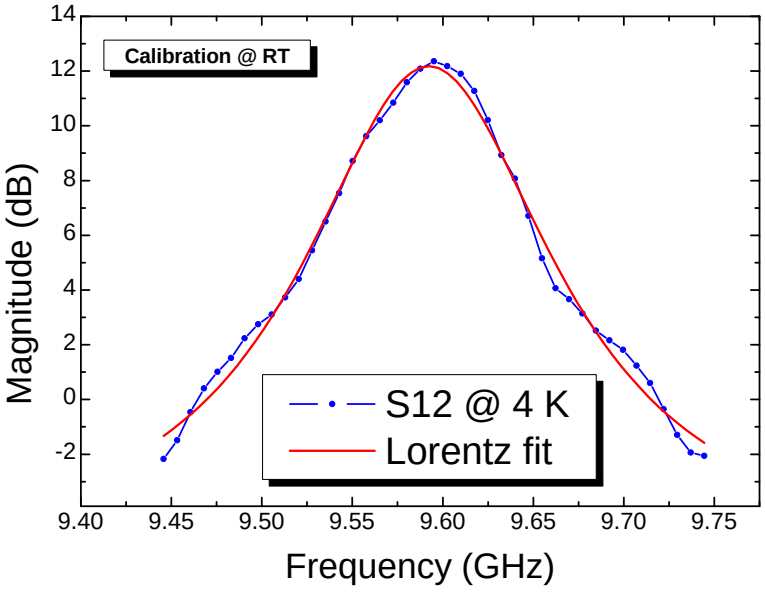

Figure 4.23: Lorentz fit to the S_{12} resonance of Sample 133 (g.) at $T = 4$ K for our alternative calibration scheme.

assuming the peak represents the first harmonic $\lambda/2$ resonance yields

$$L_{\text{washer,fit}} = 1056 \text{ pH} \quad , \tag{4.14}$$

which is in quite good agreement with the result obtained for Sample 148. In contrast to the previous measurements, the observed resonance is accompanied only by a dip in the S_{11} spectrum. This dip is shifted by 0.11 GHz towards lower frequencies as observed for Sample 148 when grounding the washer. Figure 4.24 shows the Lorentz fit to the S_{11} data a $T = 4$ K. The fitted dip frequency is $f_{\text{fit}} = 9.484$ GHz with a FWHM of 45.802 MHz yielding a $Q_{\text{int}} \approx 207$ which is a factor of 24 smaller than reported in reference [43]. This is the highest Q_{int} obtained so far[10].

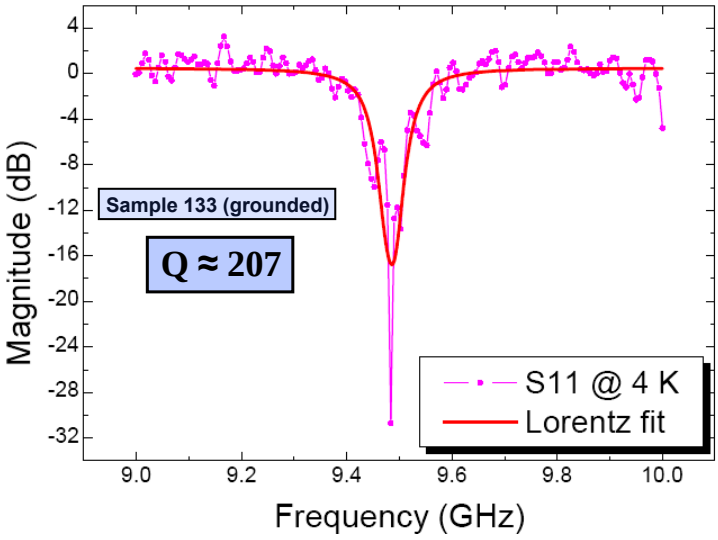

Figure 4.24: Lorentz fit to the S_{11} data of Sample 133 (g.) at $T = 4$ K.

The peak around 10.2 GHz in Figure 4.22 could not be observed in the standard calibration measurement from Figure 4.21 and unfortunately the S_{ii} spectra were only recorded in the range 0 - 10 GHz.
The small peak and its corresponding dip around 7.2 GHz in Figure 4.22 can not be explained by $\lambda/2$ resonances, provided that the previously discussed resonance is indeed the first harmonic $\lambda/2$ resonance. However, for the

[10]This value for Q_{int} represents a lower limit as the data point at -32 dB could not be implemented in our fit procedure.

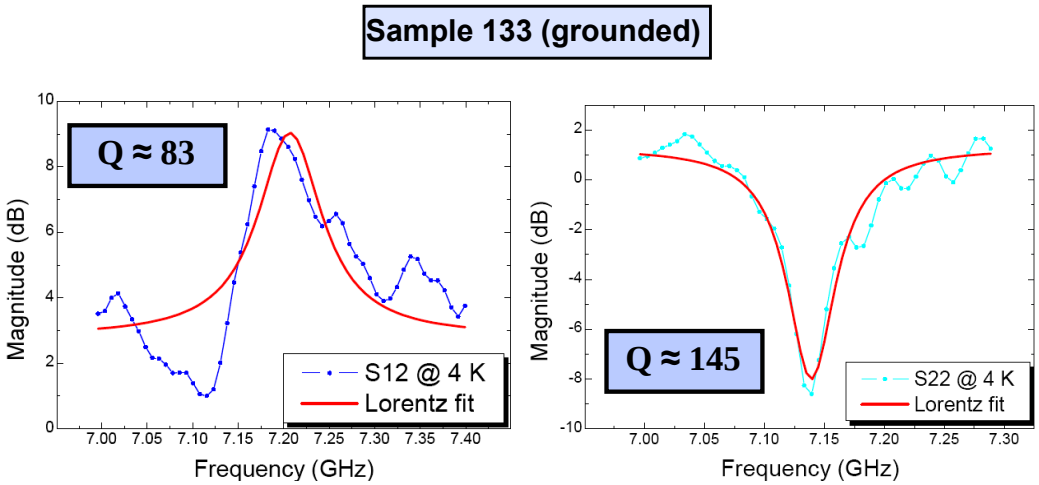

Figure 4.25: (a) Lorentz fit to the S_{12} spectrum around 7.2 GHz at $T = 4$ K. (b) Lorentz fit to the S_{22} spectrum around 7.2 GHz at $T = 4$ K.

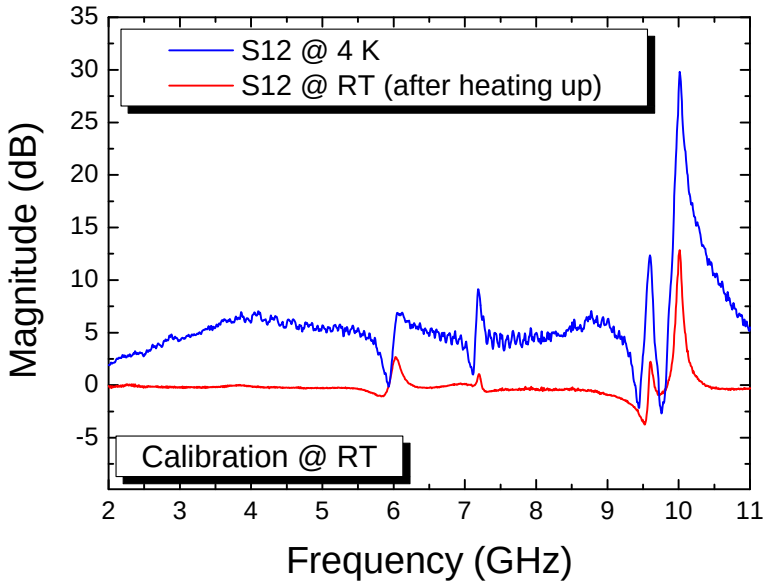

Figure 4.26: S_{12} data at $T = 4$ K and RT after heating up. The peaks observed at $T = 4$ K are still present at RT yet with a smaller magnitude.

sake of completeness, a Lorentz fit to the S_{12} and S_{22} spectrum around 7.2 GHz is shown in Figure 4.25 (a) and (b), respectively. The quality factor extracted from the peak in the S_{12} spectrum was $Q_{\text{int}} = 83$ with a center frequency of 7.207 GHz while the quality factor for the reflection measurement is $Q_{\text{int}} \approx 145$ at a center frequency of 7.139 GHz.
After heating up to RT we recalled the calibration data and expected to see a flat line at 0 dB. However, this was not the case and Figure 4.26 shows the measured data. In fact we observed peaks at the same positions as for the measurement at $T = 4$ K but with smaller magnitude. Under these circumstances, only the resonance around 9.5 GHz can be clearly assigned to our sample as it was observed for both calibration schemes.

Washer grounded – Sample 1 (no calibration) & Sample 37

In this section we will discuss the S-parameter measurements of Sample 1 and Sample 37 simultaneously. By combining the results of these two measurements we will get more insight into the behavior of our MRs when grounding the washer.
Both resonators are identical except for the width of the CPW section leading to a different Z_{CPW} and C_{CPW} (see Table 4.1). As the TLM is quite insensitive to Z_{CPW} and the coupling capacitors of the CPW section only differ by 0.2 fF, the calculated resonance frequencies are essentially the same for both specimen.
Sample 1 was the first resonator we measured and we did not perform the standard calibration scheme at this time. Furthermore, we were not aware of the importance of a simultaneous reflection measurement. Figure 4.27 shows the measured data in the frequency range from 4 - 4.9 GHz and for a broad range of temperatures. We observe a resonance peak at 4.677 GHz with an increase in magnitude for decreasing temperature, however, we expected a more explicit increase for $T < T_c$. The quality factor at $T = 4$ K is only $Q_{\text{int}} \approx 23$ with a center frequency $f_{\text{fit}} = 4.646$ GHz. In contrast to our previously discussed results, we observe the expected increase of the resonance frequency for decreasing temperature as reported in reference [43].
The measured S-parameters of Sample 37 with a grounded washer are shown in Figure 4.28. Although we see no resonances in the different S_{12} spectra[11],

[11]The increase in magnitude around 9 GHz was observed for many more samples and can not be accounted for by our MR as discussed earlier in the text.

the S_{11} spectrum clearly shows two dips at $f_{\text{fit},0} = 4.837$ GHz ($Q_{\text{int}} \approx 10$) and $f_{\text{fit},1} = 9.623$ GHz ($Q_{\text{int}} \approx 23$). The second dip is also observed in the S_{22} spectrum. These two dips are separated by 4.786 GHz $\approx f_{\text{fit},0}$ as expected

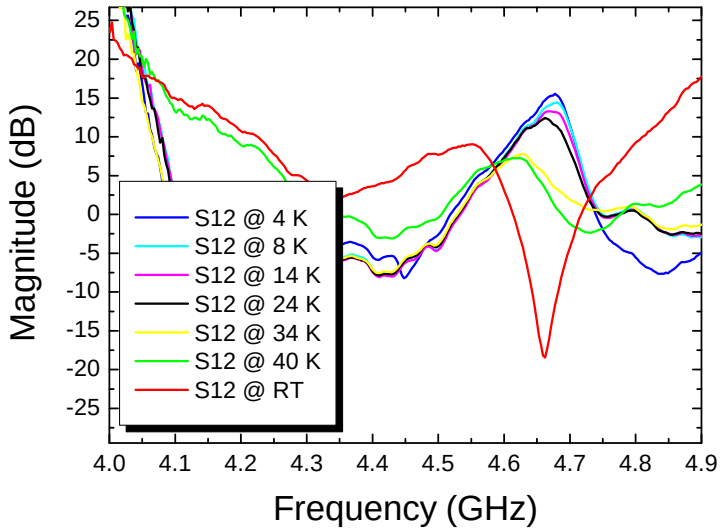

Figure 4.27: Measured S-parameters of Sample 1 (grounded washer) at different temperatures without calibration. The quality factor of the resonance peak at $T = 4$ K is $Q_{\text{int}} \approx 23$ with a center frequency of $f_{\text{fit}} = 4.646$ GHz.

for an open $\lambda/2$ resonator assuming that the dip at 4.837 GHz corresponds to the fundamental $\lambda/2$ resonance. Thus, we have strong evidence, that the peak at $f_{\text{fit}} = 4.646$ GHz observed for Sample 1 is the fundamental $\lambda/2$ resonance and corresponds to the observed dip in the S_{11} spectrum of Sample 37. A fit for the washer inductance yields,

$$L_{\text{washer,fit}} = 1127 \text{ pH} \quad , \tag{4.15}$$

where we used $f_{\text{fit}} = 4.646$ GHz. Fitting the washer inductance with the resonance frequencies obtained from the S_{11} spectrum of Sample 37 yields

$$L_{\text{washer,fit}} = \begin{cases} 1038 \text{ pH} & \text{for} \quad f_{\text{fit},0} = 4.837 \text{ GHz} \\ 1049 \text{ pH} & \text{for} \quad f_{\text{fit},1} = 9.623 \text{ GHz} \end{cases} \tag{4.16}$$

These results are in very good agreement with the results obtained for Sample 148 and Sample 133 when grounding the washer. Furthermore, as Sample 37

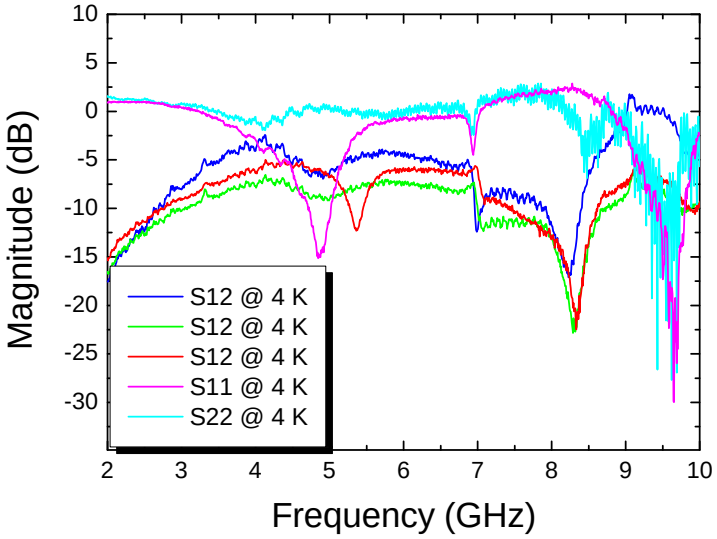

Figure 4.28: Measured S-parameters of Sample 37 (grounded washer) at different temperatures. The quality factor of the dip in the S_{11} spectrum at $f_{\text{fit}} = 4.837$ GHz is $Q_{\text{int}} \approx 10$.

and Sample 133 have the same parameters except for the coupling capacitors, we can conclude that the resonance observed for Sample 133 was indeed the first harmonic $\lambda/2$ resonance. So far, we have strong evidence, that grounding the washer effectively increases its inductance to a value of approximately 1.1 nH. However, the poor quality factors obtained for both samples are way beyond the expected values.

Disregarded Measurements

As mentioned earlier in the text, we performed 28 measurements on 14 different samples. The obtained data was often not consistent with the expected behavior of our MRs. Only for the measurements presented in this thesis, we could observe peaks in the transmission spectra *and* the corresponding dips in the reflection spectra. The following section gives a short overview over some of these measurements.

Measurements performed on samples with the three-finger interdigital coupling capacitors[12] showed a very noisy reflection spectra and in the transmission spectra neither peaks nor dips could be observed. However, this effect is not necessarily associated with the value of the coupling capacitor since we

[12] See Figure 3.8 (b)

also observed noisy reflection spectra for small values of the coupling capacitors.
After that we concentrated on measurements with small gap coupling capacitors. One of the most promising samples (Sample 160) in terms of a small reflection coefficient $\Gamma \approx 5 \cdot 10^{-3}$ at the via showed a clear dip in the S_{11} spectrum but no resonance in the transmission spectrum could be observed. The same reflection spectrum was observed for Sample 177 which has in contrast to Sample 160 $\Gamma \approx 0.3$ and a negligible smaller value of the coupling capacitor. As the best measurement results were obtained for samples with $\Gamma \approx 0.36$ we can conclude that impedance matching at the point of the via does not seem to be the crucial factor for the performance of the resonator.
We also performed measurements on Sample 37 H60 which has the same parameters as Sample 37 except that the square shaped hole in the washer has a width of 60 μm. For this measurement we grounded the washer and expected similar spectra as for Sample 37 (g.). Similar to the case of Sample 37 (g.) we did not observe peaks in the S_{12} spectrum, however, two dips in the S_{11} spectrum, one at 5.702 GHz and the other at 9.284 GHz were clearly visible. This result is in contrast to the measurement of Sample 37 (g.) where we observed equidistant dips at 4.837 GHz and 9.623 GHz. Furthermore, the reduction of the size of the hole leads to an increase of $L_{\text{washer}} \approx 930$ pH, therefore, the expected resonance frequency should be smaller than for Sample 37 (g.).
In the following chapter we will give a summary and an outlook on an alternative measurement scheme involving a cryogenic wafer probing system.

Chapter 5

Summary and Outlook

This thesis was motivated by the idea to design a high-Q superconducting Microstrip Resonator (MR) for application in Circuit-QED. The device is based upon the SQUID microstrip amplifier discussed by M. Mück and J. Clarke [36]. Theoretically, the geometry of the device should allow for a strong qubit-cavity-coupling $g \approx 200$ MHz which is twice the value calculated in reference [13].
The fundamental transmission line parameters Z_0 and $\gamma = \alpha + j\beta$ have been derived for normal conducting metals and low-loss lines. These expressions were then modified for the case of superconducting materials and the two important types of transmission lines realized in our design – the microstrip (MS) and the coplanar waveguide (CPW). A short introduction to the topic of distributed resonators formed of transmission lines was followed by the discussion of the actual design of the MR.
The MR was designed with the *Xic*© software package and the build-in inductance and capacitance extraction programs FastHenry© and FastCap© were used for estimation of the washer inductance and the coupling capacitors, respectively. In accordance with the Ketchen-Jaycox model, the resonance frequency of the MR is dominated by the inductance of the slitted washer and the number of turns of the spiral input coil. The values for the washer inductance obtained by the analytical formula (157 pH) given in reference [37] differ by a factor of 5 from the values obtained from simulations (FastHenry© (848 pH) and 3D-MLSI© (880 pH)). From our experimental results we can conclude that the actual washer inductance lies in between the analytical value and the value obtained by the simulations. Due to the effects of the slitted washer, the expressions for the attenuation in the MS section had to

Sample	**Resonance** [GHz]	$\mathbf{Q}_{\text{int}}$ **Transm.**	$\mathbf{Q}_{\text{int}}$ **Refl.**	$\mathbf{L}_{\text{washer,fit}}$
37 (n.g.)	$f_{0,\lambda/2} = 6.873$	50	180	499 pH
148 (n.g.)	$f_{0,\lambda/2} = 7.393$	30	160	366 pH
148 (g.)	$f_{0,\lambda/2} = 4.278$	2	-	1159 pH
133 (g.)	$f_{1,\lambda/2} = 9.592$	56	207	1056 pH
1 (g.)	$f_{0,\lambda/2} = 4.646$	23	-	1127 pH
37 (g.)	$f_{0,\lambda/2} = 4.837$	-	10	1038 pH
37 (g.)	$f_{1,\lambda/2} = 9.623$	-	23	1049 pH

Table 5.1: Measured resonance frequencies and quality factors for transmission and reflection. The abbreviations *n.g.* and *g.* stand for *not grounded* and *grounded*, respectively.

be modified. We modeled the MR by means of transmission line theory and the calculated values for the resonance frequencies are in very good agreement with the values obtained by the figure of merit for a $\lambda/2$-resonator. The measurement setup, the topic of S-parameters, and the calibration schemes for transmission and reflection measurements were discussed thoroughly. A measurement with a SQUID magnetometer determined the critical temperature T_c of our MRs.

Table 5.1 lists the measured resonance frequencies and quality factors for the samples discussed in this thesis. For the measurements where we did not ground the washer, the obtained resonance frequencies are at lest a factor of 1.3 higher than predicted by theory. In order to match the observed resonances to theory, we fitted for the washer inductance as this is the dominating term. However, the results are not consistent and differ by a factor of 1.3 for Sample 37 (n.g.) and Sample 148 (n.g.). Especially for the measurement of Sample 148 (n.g.) the question arises to what extent we measured the response of our resonator as the resonance frequency of this sample should be definitely lower than for Sample 37 (n.g.).

For the measurements where we grounded the washer, we observe in general a lower resonance frequency than predicted by theory. However, for these measurements all the fitted washer inductances have a value around 1.1 nH. We explain this increase in L_{washer} by the presence of the bonding wire, which represents a series inductance to the washer.

Unfortunately, the quality factors extracted from the transmission and re-

flection spectra at $T = 4$ K are very small ($Q_{\text{int}} = 2 - 207$) compared to the theoretical calculated value of $Q_{\text{int}} \approx 3 \cdot 10^4$. As we can neglect conductor losses in the superconducting state, the attenuation due to dielectric loss in the very thin SiO_2 layer is most probably much higher than assumed theoretically. Up to now, *Hypres, Inc.* does not provide any data concerning the dielectric attenuation or the loss tangent. In general, the measured S-

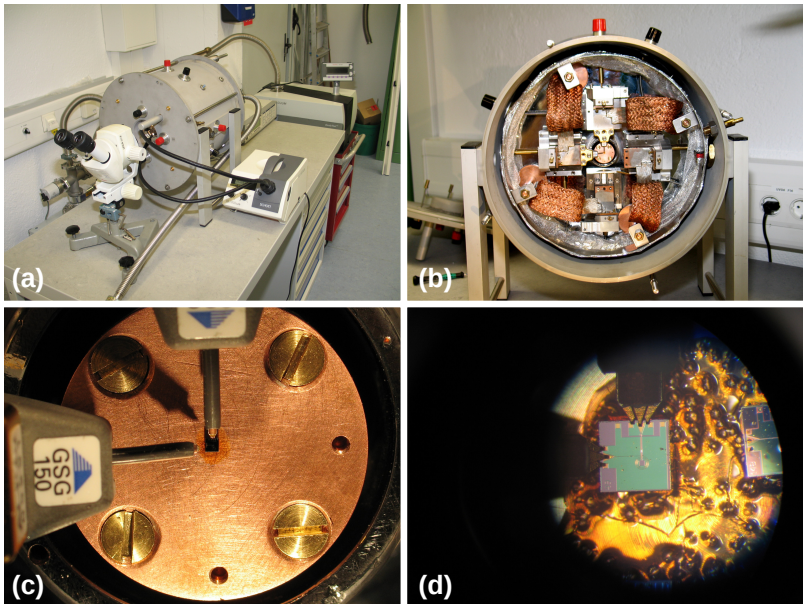

Figure 5.1: Cryogenic wafer probing system. (a) Exterior view of the probe station (without NVA). (b) Interior view of the probe station with the two sleds on which the probing tips are mounted. (c) Photograph of the copper sample holder with a MR. (d) Microscope photograph of the probing tips connected to our MR. The outer pins of the probing tips are connected to ground and the signal is applied through the pin in the middle (Ground-Signal-Ground (GSG) arrangement). The spacing between the pins is 150 μm.

parameter spectra of our resonators do not show the expected pattern of a common $\lambda/2$-resonator, except for the S_{11} spectrum of Sample 37 (g.). The MR is a quite complicated device as it consists of two different types of transmission lines connected through a via. Without the knowledge of the exact washer inductance it is very difficult to match the impedances of the two different types of transmission lines. In our measurements, however, it turned out that we obtained the best results for samples with a $Z_{\text{CPW}} = 39.3\ \Omega$. Al-

together we performed 28 measurements – most of them with the additional calibration scheme – on 14 different samples, however, only 5 measurements yielded relevant results.
With the presented calibration scheme we are only able to measure the MR *and* the bonding wires connecting it. In order to measure the MRs correctly, a deembedding procedure in combination with a **TRL** (**T**hrough-**R**eflect-**L**ine) calibration is necessary. The requirements for a TRL calibration are comprehensively summarized in reference [27]. For our case this would mean to design calibration specimens that have then to be ordered from *Hypres, Inc.*. However, if the quality factors of our MRs were in the range of $Q \sim 10^4$ we should have observed this in our experiments.
The best system to measure the properties of our resonators would be a cryogenic wafer probing system (probe station). One sample was measured with the help of D. König at the chair for solid state physics of J.P. Kotthaus (LMU München). Here, a probe station from attocube© systems[1] was available, allowing for measurements at $T = 4.2$ K without outer circuitry (e.g. bonding wires and printed circuit boards). Unfortunately the probing system was not designed for operation at GHz frequencies.
At the moment we are setting up a cryogenic probe station at the WMI which is suitable for operation at GHz frequencies. The system is shown in Figure 5.1 and described thoroughly in reference [44]. It allows for measurements at liquid helium temperatures. Another advantage of this system is the possibility to measure a large number of samples simultaneously. Definitely the most promising samples should be investigated with the probe station to get more insight into the complicated behavior of our MRs.

[1] http://www.attocube.com/

Appendix A

Quantization of the series LC-circuit

The *uncoupled* Microstrip Resonator discussed in this thesis can be modeled as a parallel LC-circuit in the vicinity of ω_r. However, according to reference [27], the series coupling capacitor has the effect of inverting the driving point impedance of the resonator. Thus, the Microstrip Resonator must be modeled as a series LC-circuit in the vicinity of ω_r.
It is convenient to map the problem of the resonant circuit on the well-known formalism for the harmonic oscillator (HO). The Hamiltonian for a series LC-circuit with capacitance C and inductance L is given by

$$\hat{\mathcal{H}}_{\mathrm{LC}} = \frac{1}{2L} L^2 I^2 + \frac{1}{2C} Q^2 \quad , \tag{A.1}$$

where I denotes the current and Q is the charge on the capacitor. This expression can be derived using a Legendre transformation on the Lagrangian of the series LC-circuit which is found in many textbooks, e.g. [45]. Comparing Equation (A.1) with the Hamiltonian of the HO

$$\hat{\mathcal{H}}_{\mathrm{HO}} = \frac{1}{2m} p^2 + \frac{m\omega^2}{2} x^2 \tag{A.2}$$

gives rise to the following substitutions:

$$\boxed{\begin{aligned} p &\Longleftrightarrow LI \\ x &\Longleftrightarrow Q \\ m &\Longleftrightarrow L \\ \omega &\Longleftrightarrow \frac{1}{\sqrt{LC}} \end{aligned}} \tag{A.3}$$

We will adopt the same formalism for quantizing the HO as shown in reference [46]. Therefore, with (A.3), the non-hermitian creation and annihilation operators for the LC-circuit can be written as

$$a^\dagger = \frac{Z_0 Q - iLI}{\sqrt{2\hbar Z_0}} \qquad \text{and} \qquad a = \frac{Z_0 Q + iLI}{\sqrt{2\hbar Z_0}} \quad , \tag{A.4}$$

with the commutator relation[1]

$$[a, a^\dagger] = 1 \quad . \tag{A.5}$$

Solving for Q and LI gives

$$Q = \sqrt{\frac{\hbar}{2Z_0}}(a^\dagger + a) \qquad \text{and} \qquad LI = i\sqrt{\frac{\hbar Z_0}{2}}(a^\dagger - a) \quad . \tag{A.6}$$

Inserting Equations (A.6) in (A.1) under consideration of Equation (A.5) yields the quantized Hamiltonian for the LC-circuit,

$$\hat{\mathcal{H}}_{\mathrm{LC}} = \hbar\omega \left(a^\dagger a + \frac{1}{2} \right) \quad , \tag{A.7}$$

which is the same as the Hamiltonian for the quantum harmonic oscillator.

[1] As mentioned in section 1.3, the charge Q and the flux $\Phi = LI$ are conjugate variables with $[\hat{Q}, \hat{\Phi}] = i\hbar = [\hat{x}, \hat{p}]$. Therefore, the commutator relation for the creation and annihilation operators of the LC-circuit must be the same as in the case of the HO, $[a, a^\dagger]_{LC} = 1 = [a, a^\dagger]_{HO}$

Appendix B

External Quality Factor Q_{ext}

In many textbooks the expression for the external quality factor of a parallel resonant circuit is given by

$$Q_{\text{ext}} = \frac{R_{\text{ext}}}{\omega_r L} \quad , \tag{B.1}$$

where R_{ext} represents the outer circuitry, ω_r is the resonance frequency, and L the inductance of the circuit. With $\omega_r = \sqrt{L/C}$ and $R_{\text{ext}} = 1/G_{\text{ext}}$ Equation (B.1) yields

$$Q_{\text{ext}} = \frac{\omega_r C}{G_{\text{ext}}} \quad . \tag{B.2}$$

Let us first assume a *symmetrically* coupled MR as shown in Figure B.1. At the resonance frequency, the external impedance Z_{ext} seen at one end of the resonator is given by

$$Z_{\text{ext}} = R_L - j\frac{1}{\omega_r C_k} \quad . \tag{B.3}$$

Then, the external admittance $Y_{\text{ext}} = 1/Z_{\text{ext}}$ can be calculated as

$$Y_{\text{ext}} = \frac{\omega_r C_k}{R_L \omega_r C_k - j} = \frac{R_L \omega_r^2 C_k^2}{1 + R_L^2 \omega_r^2 C_k^2} + j\frac{\omega_r C_k}{1 + R_L^2 \omega_r^2 C_k^2} \quad . \tag{B.4}$$

Now, the overall external conductance for *both* branches of the MR is given by

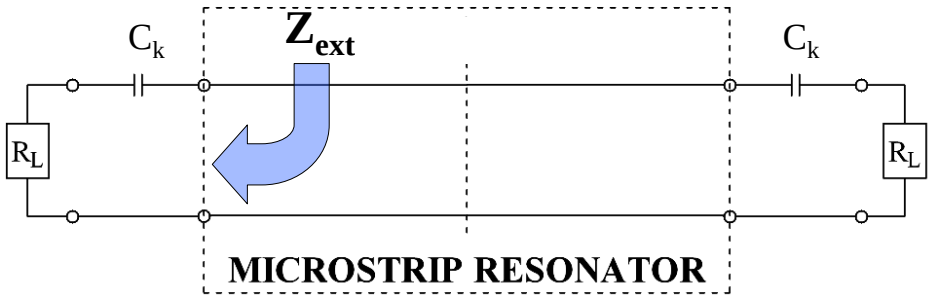

Figure B.1: Capacitive coupled MR. Out of symmetry reasons it is sufficient to calculate Z_{ext} for only one half of the MR.

$$G_{\text{ext}} = 2 \cdot \Re\{Y_{\text{ext}}\} = \frac{2R_L\omega_r^2 C_k^2}{1 + R_L^2\omega_r^2 C_k^2} \quad . \tag{B.5}$$

In the case of an *asymmetrically* coupled MR, the external conductance can be expressed as the sum of the external conductances for each branch,

$$G_{\text{ext}} = \frac{R_L\omega_r^2 C_{\text{k,MS}}^2}{1 + R_L^2\omega_r^2 C_{\text{k,MS}}^2} + \frac{R_L\omega_r^2 C_{\text{k,CPW}}^2}{1 + R_L^2\omega_r^2 C_{\text{k,CPW}}^2} \quad . \tag{B.6}$$

Here, $C_{\text{k,MS}}$ and $C_{\text{k,CPW}}$ denote the coupling capacitors for the MS- and CPW-section, respectively. Inserting Equation (B.6) into Equation (B.2) gives the external quality factor depending on known quantities of our circuit.

Appendix C

Specimen Overview

	MS	CPW	CPW	CPW	CPW
w [μm]	5	5	10	15	20
C_s [fF]	1.7	1.8	1.9	2.0	2.0
C_b [fF]	6.8	9.5	-	-	10.0
$C_{\mathrm{g},5}$ [fF]	0.6	0.5	-	-	1.4
$C_{\mathrm{g},10}$ [fF]	0.5	0.4	-	-	0.9
$C_{\mathrm{g},15}$ [fF]	0.5	0.2	-	-	0.6
$C_{\mathrm{g},20}$ [fF]	0.5	0.2	-	-	0.5
$C_{\mathrm{g},25}$ [fF]	0.5	0.1	-	-	0.3
$C_{\mathrm{g},30}$ [fF]	0.3	0.1	-	-	0.3

Table C.1: Approximate values of the coupling capacitors realized in our designs. The indices *s*, *b*, and *g* stand for *s*mall, *b*ig, and *g*ap, respectively. The number after g is the width of the gap in μm. w is the width of the corresponding transmission line section.

From 196 designed samples 98 were chosen for production. Tables C.2 - C.5 contain the parameters of all Microstrip Resonators that were ordered from *Hypres, Inc.*. n is the number of turns of the spiral input coil, l_MS and l_CPW are the lengths from the via to the coupling capacitor in the MS- and CPW-section, respectively. Thus, $l = l_\mathrm{MS} + l_\mathrm{CPW}$ is the total length of the resonator. w_CPW is the width of the center strip in the CPW section and C_k is the type of coupling capacitor. The values for the different types of coupling capacitors are found in Table C.1. $f_{0,\lambda/2}$ is the fundamental

resonance frequency calculated with Equation (3.25) where we used $L_{\text{washer}} = 848$ pH.

Sample	n	l_{MS} $[\mu m]$	$l_{\text{CWG}}[\mu m]$	$w_{\text{CWG}}[\mu m]$	C_{k}	$f_{0,\lambda/2}$ [GHz]
1	3	2140	125	5	C_{s}	5.335
2	2	1354	125	5	C_{s}	9.990
3	1	694	125	5	C_{s}	27.254
4	2	1173	35	5	C_{s}	10.768
5	3	1688	39	5	C_{s}	6.028
6	2	1682	303	5	C_{s}	8.914
7	2	890	60	5	C_{s}	12.422
8	3	2487	250	5	C_{s}	4.935
9	3	1391	109	5	C_{s}	6.656
10	1	1132	339	5	C_{s}	20.753
11	4	2529	45	5	C_{s}	3.701
12	3	2138	295	5	C_{s}	5.337
13	3	2140	125	10	C_{s}	5.335
19	2	890	60	10	C_{s}	12.422
23	4	2529	45	10	C_{s}	3.701
25	3	2140	125	15	C_{s}	5.335
31	2	890	60	15	C_{s}	12.422
35	4	2529	45	15	C_{s}	3.701
37	3	2140	125	20	C_{s}	5.335
38	2	1354	125	20	C_{s}	9.990
39	1	694	125	20	C_{s}	27.254

Table C.2: Parameters of all produced resonators. n denotes the number of turns and l_{MS} and l_{CPW} are the lengths from the via to the coupling capacitor in the MS- and CPW-section, respectively. w_{CPW} is the width of the center strip in the CPW-section, C_{k} denotes the type of coupling capacitor, and $f_{0,\lambda/2}$ is the calculated resonance frequency.

Sample	n	l_{MS} $[\mu m]$	$l_{\mathrm{CWG}}[\mu m]$	$w_{\mathrm{CWG}}[\mu m]$	C_{k}	$f_{0,\lambda/2}$ [GHz]
40	2	1173	35	20	C_{s}	10.768
41	3	1688	39	20	C_{s}	6.028
42	2	1682	303	20	C_{s}	8.914
43	2	890	60	20	C_{s}	12.422
44	3	2487	250	20	C_{s}	4.935
45	3	1391	109	20	C_{s}	6.656
46	1	1132	339	20	C_{s}	20.753
47	4	2529	45	20	C_{s}	3.701
48	3	2138	295	20	C_{s}	5.337
49	3	2140	125	5	C_{b}	5.335
50	2	1354	125	5	C_{b}	9.990
51	1	694	125	5	C_{b}	27.254
52	2	1173	35	5	C_{b}	10.768
53	3	1688	39	5	C_{b}	6.028
54	2	1682	303	5	C_{b}	8.914
55	2	890	60	5	C_{b}	12.422
56	3	2487	250	5	C_{b}	4.935
57	3	1391	109	5	C_{b}	6.656
58	1	1132	339	5	C_{b}	20.753
59	4	2529	45	5	C_{b}	3.701
60	3	2138	295	5	C_{b}	5.337
85	3	2140	125	5	C_{b}	5.335
86	2	1354	125	5	C_{b}	9.990
87	1	694	125	5	C_{b}	27.254
88	2	1173	35	5	C_{b}	10.768
89	3	1688	39	5	C_{b}	6.028
90	2	1682	303	5	C_{b}	8.914
91	2	890	60	5	C_{b}	12.422
92	3	2487	250	5	C_{b}	4.935
93	3	1391	109	5	C_{b}	6.656

Table C.3: Parameters of all produced resonators. n denotes the number of turns and l_{MS} and l_{CPW} are the lengths from the via to the coupling capacitor in the MS- and CPW-section, respectively. w_{CPW} is the width of the center strip in the CPW-section, C_{k} denotes the type of coupling capacitor, and $f_{0,\lambda/2}$ is the calculated resonance frequency.

Sample	n	l_{MS} $[\mu m]$	$l_{\mathrm{CWG}}[\mu m]$	$w_{\mathrm{CWG}}[\mu m]$	C_{k}	$f_{0,\lambda/2}$ [GHz]
94	1	1132	339	5	C_{b}	20.753
95	4	2529	45	5	C_{b}	3.701
96	3	2138	295	5	C_{b}	5.337
97	3	2140	125	5	$C_{\mathrm{g,10}}$	5.335
98	2	1354	125	5	$C_{\mathrm{g,10}}$	9.990
99	1	694	125	5	$C_{\mathrm{g,10}}$	27.254
100	2	1173	35	5	$C_{\mathrm{g,10}}$	10.768
101	3	1688	39	5	$C_{\mathrm{g,10}}$	6.028
102	2	1682	303	5	$C_{\mathrm{g,10}}$	8.914
103	2	890	60	5	$C_{\mathrm{g,10}}$	12.422
104	3	2487	250	5	$C_{\mathrm{g,10}}$	4.935
105	3	1391	109	5	$C_{\mathrm{g,10}}$	6.656
106	1	1132	339	5	$C_{\mathrm{g,10}}$	20.753
107	4	2529	45	5	$C_{\mathrm{g,10}}$	3.701
108	3	2138	295	5	$C_{\mathrm{g,10}}$	5.337
133	3	2140	125	20	$C_{\mathrm{g,10}}$	5.335
134	2	1354	125	20	$C_{\mathrm{g,10}}$	9.990
135	1	694	125	20	$C_{\mathrm{g,10}}$	27.254
136	2	1173	35	20	$C_{\mathrm{g,10}}$	10.768
137	3	1688	39	20	$C_{\mathrm{g,10}}$	6.028
138	2	1682	303	20	$C_{\mathrm{g,10}}$	8.914
139	2	890	60	20	$C_{\mathrm{g,10}}$	12.422
140	3	2487	250	20	$C_{\mathrm{g,10}}$	4.935
141	3	1391	109	20	$C_{\mathrm{g,10}}$	6.656
142	1	1132	339	20	$C_{\mathrm{g,10}}$	20.753
143	4	2529	45	20	$C_{\mathrm{g,10}}$	3.701
144	3	2138	295	20	$C_{\mathrm{g,10}}$	5.337
145*	3	2447	460	5	C_{s}	4.977
148*	3	2447	460	20	C_{s}	4.977
149*	2	1319	460	5	C_{s}	10.129

Table C.4: Parameters of all produced resonators. n denotes the number of turns and l_{MS} and l_{CPW} are the lengths from the via to the coupling capacitor in the MS- and CPW-section, respectively. w_{CPW} is the width of the center strip in the CPW-section, C_{k} denotes the type of coupling capacitor, and $f_{0,\lambda/2}$ is the calculated resonance frequency. For samples denoted by a *, the second coupling capacitor is situated on the inner edge of the input coil as shown in Figure 4.10.

Sample	n	l_{MS} $[\mu m]$	$l_{\mathrm{CWG}}[\mu m]$	$w_{\mathrm{CWG}}[\mu m]$	C_{k}	$f_{0,\lambda/2}$ [GHz]
152*	2	1319	460	20	C_{s}	10.129
153	2	1173	35	5	$C_{\mathrm{g,5}}$	10.768
157	2	1173	35	5	$C_{\mathrm{g,15}}$	10.768
158	2	1173	35	5	$C_{\mathrm{g,20}}$	10.768
159	2	1173	35	5	$C_{\mathrm{g,25}}$	10.768
160	2	1173	35	5	$C_{\mathrm{g,30}}$	10.768
177	2	1173	35	20	$C_{\mathrm{g,5}}$	10.768
181	2	1173	35	20	$C_{\mathrm{g,15}}$	10.768
182	2	1173	35	20	$C_{\mathrm{g,20}}$	10.768
183	2	1173	35	20	$C_{\mathrm{g,25}}$	10.768
184	2	1173	35	20	$C_{\mathrm{g,30}}$	10.768
185	3	2140	125	5	C_{s}	5.335
186	2	1354	125	5	C_{s}	9.990
37 100	3	2140	125	20	C_{s}	5.335
37 60	3	2140	125	20	C_{s}	5.335
37 H60	3	2140	125	20	C_{s}	5.335
37 H80	3	2140	125	20	C_{s}	5.335

Table C.5: Parameters of all produced resonators. n denotes the number of turns and l_{MS} and l_{CPW} are the lengths from the via to the coupling capacitor in the MS- and CPW-section, respectively. w_{CPW} is the width of the center strip in the CPW-section, C_{k} denotes the type of coupling capacitor, and $f_{0,\lambda/2}$ is the calculated resonance frequency. For samples denoted by a *, the second coupling capacitor is situated on the inner edge of the input coil as shown in Figure 4.10. For Sample 37 100 and Sample 37 60, the slit in the groundplane has a width of 100 μm and 60 μm, respectively. For Sample 37 H60 and Sample 37 H80, the square shaped hole in the washer has a width of 60 μm and 80 μm, respectively.

Bibliography

[1] R.P. Feynman. Simulating Physics with Computers. *Int. J. Theor. Phys.*, V 21:467, 1982.

[2] D. Deutsch. Quantum theory, the Church-Turing Principle and the universal quantum computer. *Proc. R. Soc. London A*, 400:97, 1985.

[3] P. Shor. Algorithms for quantum computation: Discrete logarithms and factoring. *in Proc. 35th Ann. Symp. on the Foundations of Computer Science (ed. S. Goldwasser), IEEE Computer Society Press, Los Alamitos, California*, 1:124–134, 1994.

[4] R. Gross and A. Marx. *Applied Superconductivity: Josephson Effect and Superconducting Electronics.* http://www.wmi.badw.de/E23/lehre/skript/index.html, (Walther-Meissner-Institut, Garching b. München), 2006.

[5] A. J. Leggett and A. Garg. Quantum mechanics versus macroscopic realism: Is the flux there when nobody looks? *Phys. Rev. Lett.*, 54:857, 1985.

[6] D. B. Schwartz, B. Sen, C. N. Archie, and J. E. Lukens. Quantitative study of the effect of the environment on macroscopic quantum tunneling. *Phys. Rev. Lett.*, 55:1547, 1985.

[7] J.R. Friedman, V. Patel, W. Chen, S.K. Tolpygo, and J.E. Lukens. Quantum superposition of distinct macroscopic states. *Nature*, 406:43–46, 2000.

[8] J.E. Mooij, T.P. Orlando, L. Levitov, Lin Tian, Caspar H. van der Wal, and Seth Lloyd. Josephson persistent-current qubit. *Science*, 285:1036, 1999.

[9] R. Doll and M. Näbauer. Experimental proof of magnetic flux quantization in a superconducting ring. *Phys. Rev. Lett.*, 7:51–52, 1961.

[10] B.S. Deaver and W.M. Fairbank. Experimental evidence for quantized flux in superconducting cylinders. *Phys. Rev. Lett.*, 7:43–46, 1961.

[11] M.J. Storcz. *Decoherence, control, and cncoding of coupled solid-state quantum bits.* PhD thesis, Ludwig-Maximilians-Universität München, 2005.

[12] M. Mariantoni, M.J. Storcz, F.K. Wilhelm, W.D. Oliver, A. Emmert, A. Marx, R. Gross, H. Christ, and E. Solano. Generation of Microwave Single Photons and Homodyne Tomography on a Chip. *submitted to Phys. Rev. Lett., cond-mat/0509737*, 2005.

[13] A. Blais, R.-S. Huang, A. Wallraff, S.M. Girvin, and R. J. Schoelkopf. Cavity quantum electrodynamics for superconducting electrical circuits: an architecture for quantum computation. *Phys. Rev. A*, 69:062320, 2004.

[14] S. van Enk, J. Cirac, and P. Zoller. Photonic channels for quantum communication. *Science*, 279:205, 1998.

[15] A. Wallraff, D.I. Schuster, A. Blais, L. Frunzio, R.-S. Huang, J. Majer, S. Kumar, S.M. Girvin, and R.J. Schoelkopf. Strong coupling of a single photon to a superconducting qubit using circuit quantum electrodynamics. *Nature*, 431:162–167, 2004.

[16] R.K. Hoffmann. *Handbook of Microwave Integrated Circuits.* Artech House, (Norwood, MA), 1987.

[17] T. Edwards. *Foundations for Microstrip Circuit Design.* John Wiley & Sons, (West Sussex, England), 1992.

[18] H. A. Wheeler. Transmission-line properties of a strip on a dielectric sheet on a plane. *IEEE Trans. Microw. Theory Tech.*, 25:631, 1977.

[19] M. Kirschning and R. H. Jansen. Accurate model for effective dielectric constant of microstrip with validity up to millimeter-wave frequencies. *Electron. Lett.*, 18:272, 1982.

[20] M. Kobayashi. A dispersion formula satisfying recent requirements in microstrip CAD. *IEEE Trans. Microw. Theory Tech.*, 36:1246, 1988.

[21] R. N. Simons. *Coplanar Waveguide Circuits, Components, and Systems.* John Wiley & Sons, (New York), 2001.

[22] G. Hasnain, A. Dienes, and J. R. Whinnery. Dispersion of picosecond pulses in coplanar transmission lines. *IEEE Trans. Microw. Theory Tech.*, 34:738, 1986.

[23] R. Meservey and P. M. Tedrow. Measurements of the kinetic inductance of superconducting linear structures. *J. Appl. Phys.*, 40:2028, 1969.

[24] W.H. Chang. The inductance of a superconducting strip transmission line. *J. Appl. Phys.*, 50:8129, 1979.

[25] J.C. Swihart. Field solution for a thin-film superconducting strip transmission line. *J. Appl. Phys.*, 32:461, 1961.

[26] Hypres Inc. Niobium integrated circuit fabrication design rules. http://www.hypres.com/pages/download/designrules/rules.pdf, 2005.

[27] D. M. Pozar. *Microwave Engineering, Third Edition.* John Wiley & Sons, Inc., (New York), 2005.

[28] T. v. Duzer and C. W. Turner. *Principles of superconducive devices and circuits.* Edward Arnold, (London), 1981.

[29] D.C Mattis and J. Bardeen. Theory of anomalous skin effect in normal and superconducting metals. *Phys. Rev.*, 111:412, 1959.

[30] C. Wilker, Z.-Y. Shen, and V. X. Nguyen ans M. S. Brenner. A sapphire resonator for microwave characterization of superconducting thin films. *IEEE Trans. Appl. Supercond.*, 3:1457, 1993.

[31] O.R. Baiocchi, K.S.Kong, H. Ling, and T. Itoh. Effects of superconducting losses in pulse propagation on microstrip lines. *IEEE Microw. Guided Wave Lett.*, 1:1051, 1991.

[32] R.L. Kautz. Picosecond pulses on superconducting striplnes. *J. Appl. Phys.*, 49:308, 1978.

[33] W. Rauch, E. Gornik, G. Solkner, A. A. Valenzuela, F. Fox, and H. Behner. Microwave properties of $YBa_2Cu_30_{7-x}$ thin films studied with coplanar transmission line resonators. *J. Appl. Phys.*, 73:1866–1872, 1993.

[34] G.E. Ponchak and L.P.B. Kathei. Open- and short-circuit terminated series stubs in finite-width coplanar waveguide on silicon. *IEEE Trans. Microw. Theory Tech.*, 45:970, 1997.

[35] R. E. Collin. *Foundations for Microwave Engineering, Second Edition.* Wiley-IEEE Press, (New Jersey), 2000.

[36] M. Mück and J. Clarke. The superconducting quantum intereference device microstrip amplifier: Computer models. *J. Appl. Phys.*, 88:6910, 2000.

[37] M.B. Ketchen and J.M. Jaycox. Planar coupling scheme for ultra low noise dc squids. *IEEE Trans. Magn.*, 17:400, 1981.

[38] S. Ramo, J.R. Whinnery, and T. v. Duzer. *Fields and Waves in Communication Electroncis.* John Wiley & Sons, Inc., 1994.

[39] Stöcker. *Taschenbuch der Physik.* Verlag Harii Deutsch, (Thun und Frankfurt am Main), 2000.

[40] P.M. Watson and K.C. Gupta. Design and optimization of cpw circuits using em-ann models for cpw components. *IEEE Trans. Microw. Theory Tech.*, 45:2515, 1997.

[41] Agilent Technologies Inc. Network analyzer basics. http://www.agilent.com.

[42] A. Emmert. Circuit-quantum electrodynamics (CQED) with superconducting flux qubits. Diploma Thesis, 2006.

[43] L. Frunzio, A. Wallraff, D. Schuster, J. Majer, and R. Schoelkopf. Fabrication and characterization of superconducting circuit qed devices for quantum computation. *IEEE Trans. Appl. Supercond.*, 15:860, 2005.

[44] G.J. Höfer, F. Jäger, and H.A. Kratz. Broadband four-channel cryogenic wafer probing system for automated coplanar on-chip measurements. *Rev. Sci. Instrum.*, 64:788, 1993.

[45] J.D. Jackson. *Classical electrodynamics*. John Wiley & Sons, Inc., (New York, N.Y.), 1999, 3rd ed.

[46] F. Schwabl. *Quantenmechanik*. Springer Verlag, (Berlin, Germany), 1998, 5th ed.

Danksagung

Der ansonst herrschenden Reihenfolge in Danksagungen zum Trotz, möchte ich mich zu allererst bei *meinen Eltern* bedanken, die mir nicht nur mein Studium ermöglicht haben, sondern auch immer (und damit meine ich: *immer*) hinter mir und meinen (teils nicht einleuchtenden) Entscheidungen standen.

Bei *Prof. Dr. Rudolf Gross* möchte ich mich bedanken, mir diese Diplomarbeit am Walther-Meissner-Institut ermöglicht zu haben. Er hatte immer ein offenes Ohr für die Probleme eines jungen Diplomanden.

Dr. Achim Marx danke ich für die hervorragende Betreuung während des letzten Jahres. Ohne seine Hilfe und seinen profunden Erfahrungsschatz wäre diese Diplomarbeit nicht zusatnde gekommen. Ich hoffe auch in Zukunft auf eine fruchtbare Zusammenarbeit mit ihm in seiner Qubit-Gruppe.

Meinem langjährigen Freund und jetzt in Paris heimischen Doktoranden *Andreas Emmert* möchte ich sagen: Merci Andi, ohne dich wäre das Studium so zaach geworden. Viel Glück in Paris.

Bei den Doktoranden *Tobias Heimbeck, Karl Madek* und *Georg Wild* bedanke ich mich für die hervorragenden Einweisungen in sündhaft teure Gerätschaften, Hilfestellungen jedweder Art und den Spaß im Labor.

Stefan Gepraegs, Matthias Opel, Robert Müller, Helmut Thies, Dr. Christian Probst, Thomas Brenninger, Joachim Geismann und *Frau Gabrielle Goerblich* möchte ich für die tatkräftige Unterstützung während des letzten Jahres danken.

Dem jetzt Schwerverdiener *Dieter Andres* und dem Sachverständigen in Fragen Tischfußball, *Renke Stolle*, danke ich für das angenehme Büroklima.

Last but not least danke ich allen *meinen Freunden* die mich schon so lange begleiten. Ein ganz besonderer Dank geht an meine Freundin *Denise*, die immer für mich da war und ist.